MICRO AND NANO STRUCTURED METAL COPPER TETRASILICATES

by

DARRAH K. JOHNSON-MCDANIEL

(Under the Direction of Tina T. Salguero)

ABSTRACT

The metal copper tetrasilicate series ($ACuSi_4O_{10}$), noted for its brilliant blue color, comprises $CaCuSi_4O_{10}$, $SrCuSi_4O_{10}$, and $BaCuSi_4O_{10}$. The pigments based on $CaCuSi_4O_{10}$ and $BaCuSi_4O_{10}$ have the distinction of being two of the oldest synthetic materials, dating back to 3100 and 500 B.C. respectively. Of more interest to modern audiences is the strong luminescence of the $ACuSi_4O_{10}$ series in the near-infrared. We have developed three methods for structuring the $ACuSi_4O_{10}$ series on the micro and nano scales. Chapter II details how we can synthesis micro-structured $ACuSi_4O_{10}$ using solid state synthesis with nanoscale precursors. Chapters III and IV outline how we can use hydrothermal techniques to control the size and morphology of the $ACuSi_4O_{10}$ series. And finally, Chapter V discusses how we can exfoliate the $ACuSi_4O_{10}$ series into nanosheets using hot water and agitation, as well as provides several examples of the solution processability of the nanosheets.

INDEX WORDS: nanosheets, two-dimensional materials, hydrothermal synthesis, solid state synthesis, metal copper tetrasilicates, near IR emitting materials

MICRO AND NANO STRUCTURED METAL COPPER TETRASILICATES

by

DARRAH K. JOHNSON-MCDANIEL

B.S., University of Georgia, 2010

A Dissertation Submitted to the Graduate Faculty of The University of Georgia in Partial Fulfillment of the Requirements for the Degree

DOCTOR OF PHILSOPHY

ATHENS, GEORGIA

2016

MICRO AND NANO STRUCTURED METAL COPPER TETRASILICATES

by

DARRAH K. JOHNSON-MCDANIEL

Major Professor:	Tina T. Salguero
Committee:	Jason Locklin
	Paul Schroeder

Electronic Version Approved:

Suzanne Barbour

Dean of the Graduate School

The University of Georgia

May 2016

DEDICATION

To my family: thank you for all your support over the years

ACKNOWLEDGEMENTS

I would like to acknowledge all of my fellow Salguero group members who helped me throughout my graduate years. I would be remiss if I did not thank Dr. Chris Barrett who taught me a lot about nanomaterials and microscopy during my early time in the lab. Isaiah Norris and Richard Weimar were excellent undergraduates that aided in several of the projects discussed in this thesis. Dr. Timothy Pope helped me immensely with formatting and presentations. Roshini Ramachandran was an excellent collaborator and proofreader. Dr. Matt Davidson, Matt Bloodgood, Monika Milkovska, Greg Neher, Nick Nguyen, Mayra Pedraza, Harshani Rathnaweera, Asma Sharafi, and Dan Sexton were all wonderful colleagues over the years.

I would also like to thank my committee members, Professor Paul Schroeder and Professor Jason Locklin, for their assistance and mentorship. And finally, I would like to express my deep gratitude to my research advisor, Professor Tina Salguero, for her mentorship, guidance, and support throughout my graduate career.

TABLE OF CONTENTS

Page

ACKNOWLEDGEMENTS ..... **v**

CHAPTERS

1 INDRODUCTION AND LITERATURE REVIEW **1**

The Metal Copper Tetrasilicate Series 1

Structural details 8

Nanostructured Materials 10

Research Approaches 11

References 13

2 SIZE CONTROL OF THE METAL COPPER TETRASILICATE SERIES BY MEANS OF SOLID STATE SYNTHESIS WITH NANOSCALE PRECURSORS **17**

Abstract 18

Introduction 19

Experimental 20

Results and Discussion 22

Conclusion 56

References 58

3 HYDROTHERMAL FORMATION OF CALCIUM COPPER TETRASILICATE **60**

Abstract 61

Introduction 62

Experimental 63

Results and Discussion 65

Conclusion 71

References 72

4 **SIZE AND MORPHOLOGICAL CONTROL OF STRONTIUM AND BARIUM COPPER TETRASILICATES VIA HYDROTHERMAL SYNTHESIS 75**

Abstract 76

Introduction 77

Experimental 78

Results and Discussion 81

Conclusion 97

References 99

5 EXFOLIATION OF THE METAL COPPER TETRASILICATE SERIES 101

Abstract 102

Introduction 103

Experimental 105

Results and Discussion 107

Conclusion 122

References 124

6 CONCLUSIONS 127

Conclusions 127

References.....130

CHAPTER I

INTRODUCTION AND LITERATURE REVIEW

The Metal Copper Tetrasilicate Series

As Phillip Ball stated in his wonderful treatise on color 'a good blue was hard to find'.[1] This was especially true for early civilizations because, unlike the easily found red and yellow ochres and other iron oxides widely used as colorants in ancient times, blue is not a natural earth color.[2] Clear, vibrant blues were highly prized and sought after by ancient peoples from the Mediterranean to East Asia for both aesthetic and cultural reasons. For example, blue was of particular importance to the ancient Egyptians, because they regarded it as the color of the gods.[3] While it's true that minerals such as azurite and lapis lazuli exist in beautiful shades of blue, these pigments were too rare and too difficult to mine for use on a large scale; and, in the case of azurite, too unstable.[2] For all these reasons, the ancient people were determined to create a relatively inexpensive, stable synthetic equivalent to lapis lazuli; and thus was born the first artificial pigment, calcium copper tetrasilicate, $CaCuSi_4O_{10}$, more commonly known as Egyptian blue. However, it should be noted that these ancient calcium copper tetrasilicates are rarely found as pure compounds. Rather, they are usually found in a pigment mixture, most frequently with wollastonite.[4] The standard synthesis for this striking blue pigment is thought to have employed quartz pebbles, malachite and lime, with a flux comprised of papyrus ash and trona, and firing temperatures between 800-900 °C.[5] While the exact date of initial formation is unknown, archeologists have found traces of it in a glaze on a bowl dated to 3200-3000 BC[6]; and

it might have been synthesized at approximately the same time, or even earlier, in Mesopotamia.[7] Egyptian blue was commonly used throughout Egypt and the rest of the Ancient Near East to coat objects such as beads, scarabs, statuettes, and inlays, from the time of its inception in the Bronze Age all the way down to the fall of the Roman empire.[7]

Despite its extensive usage in the ancient world, it isn't until Roman times that a documented mention of a recipe for making Egyptian blue appears. In his seminal work *de architectura libri decem* ('Ten Books on Architecture'), the 1st century BC Roman architect and engineer Marcus Vitruvius Pollio wrote that a blue pigment, caeruleum, was being manufactured in a factory in Pozzuoli by a certain trader and producer of pigments named Vestorius. Here, caeruleum was prepared from copper filings, sand, and soda which was a procedure that Vestorius had previously observed at Alexandria.[8] Unfortunately for the posterity of Egyptian blue, the recipe made no explicit mention of requiring a calcium source. This omission is probably because the location of the factory was fortuitously near a mine for calcareous sand, which contains lime.[7] The famous first century AD Roman scholar and naturalist Gaius Plinius Secundus, more commonly known as Pliny the Elder, also mentioned several different versions of caeruleum in his Natural Histories. He even commented briefly on the cost of such blue pigments, indicating that such pigments were commonly produced and traded.[9] However, Pliny too made no mention of the importance of using calcium carbonate and without the knowledge of the key component, the synthesis produces a green pigment, and therefore use of Egyptian blue underwent a dramatic decline after the fall of the Roman Empire; and, by the early Middle Ages, knowledge of its formation had disappeared.

Egyptian blue emerged from obscurity when it was chemically analyzed by Sir Humphry Davy in the early 19th century. After observing the excavation of a small pot colored with

Egyptian blue from the ruins of Pompeii, Davy analyzed the material and made the connection to Vitruvius's caeruleum due to its acid stability.[10] It is perhaps only fitting that it was a British chemist who made this important discovery since Roman Britain represents the farthest western extent of Egyptian blue's spread in antiquity, having been found in wall paintings at various Romano-British sites in middle and southern England such as Chichester's Fishbourne Palace, the Roman town of Verulamium north of London, a Roman villa south of Northampton and a Romano-British temple near Oxford.[11] Returning to Davy and his work, it would be another 74 years before there was any significant follow-up to his pioneering research on Egyptian blue. This occurred in the late 1800s when French geologist Ferdinand Fouqué was the first to establish the composition of Egyptian blue as $CaCuSi_4O_{10}$ by experimenting on archaeological samples of Egyptian blue that did not contain any soda or potash. He was also the first to successfully replicate the synthesis and to measure some of the material's physical properties. Additionally, Fouqué determined that the specific gravity of $CaCuSi_4O_{10}$ was 3.04; found that it belonged to the tetragonal system; and noted that the optical properties of the crystals were uniaxial negative and displayed pleochroism.[12] A short time later, the British chemist W. J. Russell successfully reproduced $CaCuSi_4O_{10}$ using copper carbonate, calcium carbonate, and quartz sand. Moreover, he experimented with the ratios required for obtaining the proper shade of blue. He claimed that the color was derived from the amount of copper ore used: 2-5% gave a light blue; increasing it to 25-30% gave a purple blue.[13] The late 19th century archaeologist and geologist Flaxman Spurrell also reported a synthesis of Egyptian blue that produced a purplish cast by using larger portions of lime and copper[14], but if this purple form was a discrete phase, or merely an outlier still remains to be seen.

However, despite these significant advances, it wasn't until the early 1900s that there was a systematic study of the formation of Egyptian blue when a trio of University of Edinburgh chemists, Laurie, McLintock, and Miles followed up on Russell's work, even analyzing samples that had been prepared earlier by Russell. In the process, they determined several important factors for the synthesis of Egyptian blue. Firstly, they confirmed the role of $CaCO_3$ in the formation of $CaCuSi_4O_{10}$. They also determined that the synthesis only proceeds in a narrow temperature range: below 830 °C Egyptian blue did not form and above 900 °C the reaction produced green frit, a glassy non-crystalline substance of copper doped calcium silicate used by the Egyptians as a green pigment. The ideal temperature of formation turned out to be 850 °C. Finally, they detailed the role the salt flux plays: the flux did not insert itself into the structure, but rather was present to allow the other components to be reactive, however using too much flux produces a glass.[15] Since that time, there have been several extensive investigations into the structure and formation of $CaCuSi_4O_{10}$. The crystal structure was solved by noted Berkeley mineralogist and crystallographer Adolf Pabst in the 1950s from single crystals of the $ACuSi_4O_{10}$ series synthesized using a flux based method.[16] Chase found that Pabst's measurement of the d-spacings was in good agreement with archaeological samples.[17] In the 1990s, Chakoumakos did further a refinement using neutron diffraction on a synthetic solid state sample,[18] Mirti and colleagues also refined the crystal structure from an archeological sample[7], and Bensch and Schur did a similar refinement on material that had been found on an ancient oven brick,[19]. Additional investigation into the formation of $CaCuSi_4O_{10}$ in the early 1970s by Chase[17], and then later in the 1980s by Ulrich[20], Wiedemann[3] and Tite[21], determined that heating a mixture of quartz, copper oxide and calcium carbonate, in an alkali flux, over a temperature range of 900-1000 °C produced deep blue polycrystalline $CaCuSi_4O_{10}$. More

recently, Pradell used high temperature X-ray diffraction to further determine that $CaCuSi_4O_{10}$ crystals form by nucleation in the flux phase, even at very low flux percentage, and the growth temperature range for crystallization was 1000-700 °C. Additionally, research by Pradell into the microcrystalline structure of archeological samples indicates that they were formed using flux-based methods.[22] This information, along with studies by Petrie on the materials used[5a], Jaksch's comprehensive study of ancient samples[4], and Mazzocchin's work on the possible different synthetic methods[23] sheds even more light on how the ancient people would have synthesized Egyptian blue.

Interestingly, $CaCuSi_4O_{10}$ was not the only blue pigment to dazzle the ancient world. $BaCuSi_4O_{10}$ or Han blue, has a similar history to $CaCuSi_4O_{10}$, although it was produced later and there remain no written records of its ancient synthesis.[24] From archaeometric studies on the remnants of pottery containing Han blue, the pigment's usage has been dated back to as early as 500 B.C., and it lasted until the end of the Han period in 220 A.D., akin to how the synthesis of Egyptian blue ceased with the fall of the Roman Empire.[24-25] In a similar fashion to Egyptian blue, Han blue was used to color murals, sculptures, and pottery; but unlike it's Egyptian counterpart was also found as octagonal pigment sticks, which are thought to have been used as trade currency.[26] Traces of $BaCuSi_4O_{10}$ first showed up in glassy faience[25] and it was usually present as a mixed phase with another barium copper silicate, $BaCuSi_2O_6$, or Han purple[24]. In total, there are four distinct barium copper silicates that exist: $BaCuSi_4O_{10}$, $BaCuSi_2O_6$, $BaCuSi_2O_7$, and $BaCu_2Si_2O_7$.[27] This is in marked contrast to calcium copper silicate which has not been found in other structural forms. From archeological evidence, lead is present in almost all of the Han blue and Han purple samples.[25, 28] This would seem to suggest that Han blue was primarily synthesized using flux based methods. However, there are some other possible

explanations. Studies on archeological samples indicate that barite, $BaSO_4$, was the most commonly used Ba-compound.[24] Barite is commonly found in China, whereas witherite, $BaCO_3$, is a scarce mineral.[29] Nevertheless, some samples do show evidence of witherite, $BaCO_3$, perhaps due to it being mined in conjunction with barite; and, thus, the lead could have been present to catalyze the decomposition of the barium sulfite.[30] However, the decisive heterogeneity of the lead compounds in the pigment mixture suggests that its primary usage was as a flux and that catalytic activity was simply an added bonus.[25] After the collapse of the Han dynasty, Han blue disappeared until the late 1800s when renowned French chemist Henri-Louis Le Chatelier 're-invented' $BaCuSi_4O_{10}$, even filing a patent for the invention of green, blue, and violet barium copper silicate pigments.[31] By the mid-twentieth century, Han blue's crystal structure had been solved by Pabst,[16] and was then later refined by Polish crystallographers Janczak and Kubiak in the 1990s.[32] Shortly thereafter, Chakoumakos and colleagues made a further refinement of Han blue's structure using neutron diffraction on a synthetic solid state sample.[18] More recently, $BaCuSi_4O_{10}$ has been synthesized using hydrothermal methods[33] and as a mixed oxide pigment, $Ba_{0.5}La_{0.5}Na_{0.5}Cu_{0.5}Si_4O_{10}$, for use as a glaze[34].

The striking chemical similarity between $CaCuSi_4O_{10}$ and $BaCuSi_4O_{10}$ raises the intriguing possibility as to if there was a technology transfer between the two cultures. Indeed, the presence of the Silk Road that ran between Persian Empires and pre-Imperial China cultures and served as a source of not only goods and wares, but also information, would suggest the strong possibility that such a transfer took place. However, there is as yet no archaeological evidence that Egyptian blue was ever in China. And even if there had been such a transfer, the ancient Chinese people would have still had to adapt the synthesis to accommodate a different starting material and to account for the formation of the different structural phases that the

barium copper silicate system yields. This synthesis was quite a technological achievement.[26] Indeed, the overall quality of the material created by these ancient peoples is surprisingly high, and there is not as much variation in composition as might have been expected from a relatively complicated synthesis in a time where there was no easy way to share information.[7, 13, 30] The successful development of such chemically sophisticated pigments really showcases the ingenuity and technological savvy of these ancient chemists.

$SrCuSi_4O_{10}$ has not been as well studied as its more famous counterparts. It is also, perhaps not coincidentally, the only member of the series that was not synthesized as a discrete pigment in ancient times. True, traces of it have been found in some samples of Egyptian blue, but this is most likely due to the presence of strontianite, $SrCO_3$, in the mined or quarried calcium carbonate used for the synthesis, causing the resulting pigment to contain a mixture of both $CaCuSi_4O_{10}$ and $SrCuSi_4O_{10}$ and there is no evidence to suggest this was done intentionally.[24] The literature suggests that $SrCuSi_4O_{10}$ behaves relatively similarly to the other members of the $ACuSi_4O_{10}$. Pabst synthesized single crystals using a 10% borax flux[16], but most of the other work on $SrCuSi_4O_{10}$ has been in the solid state[18, 35], although recently it has been synthesized hydrothermally[33]. $SrCuSi_4O_{10}$ has also been used in a mixed oxide pigment[36] and been a target for lanthanide incorporation by means of solid state synthesis in order to increase its reflectance[37].

It should be noted that all three members of the $ACuSi_4O_{10}$ series exist as naturally occurring minerals, albeit rare ones. As this fact was not discovered until the 20th century, the mineral forms can have had little influence on the initial pigment synthesises.[38] Cuprorivaite, which was first discovered in 1938 by Minguzzi[25c] in the Vesuvian lava and was subsequently confirmed as the mineralogical form of $CaCuSi_4O_{10}$ by Pabst[39], has been found in such widely disparate places

as Africa and the United States.[38c, 40] Wesselsite and Effenburgurite, the mineralogical forms of $SrCuSi_4O_{10}$ and $BaCuSi_4O_{10}$ respectively, are even rarer minerals and have only been found in the Kalahari Manganese Field in South Africa.[38a, 38b]

Twenty-first century access to modern colorant chemistry techniques, equipment and materials has provided us with a seemingly infinite variety of blues. Yet, even with all these choices at our disposal, our eye is still drawn to the 'good blue' found by our ancient forebears. Down through the centuries, those 'good blues' have been sought after, found, lost, re-discovered, studied and analyzed and now are being given new life as part of cutting edge 21st century technology.

Structural Details

The metal copper tetrasilicate series belongs to a larger class of materials known as the Gillespite group, $ABSi_4O_{10}$.[16] This series takes its name from the mineral Gillespite, $BaFeSi_4O_{10}$, and comprises the three metal copper tetrasilicates, $CaCuSi_4O_{10}$, $SrCuSi_4O_{10}$, and $BaCuSi_4O_{10}$, as well as their iron[41] and chromium[42] analogues. All of these isostructural materials crystallize in the P4/*ncc* space group. The metal, either copper, iron or chromium, is in square planer coordination bound to a network of tetrahedral silica (Figure 1.1a), with a cation of either calcium, strontium or barium, that sits in eight-fold coordination between the puckered metal silicate layers (Figure 1.1b). As the cation size increases from calcium to strontium to barium, so too do the overall cell dimensions of the crystal.

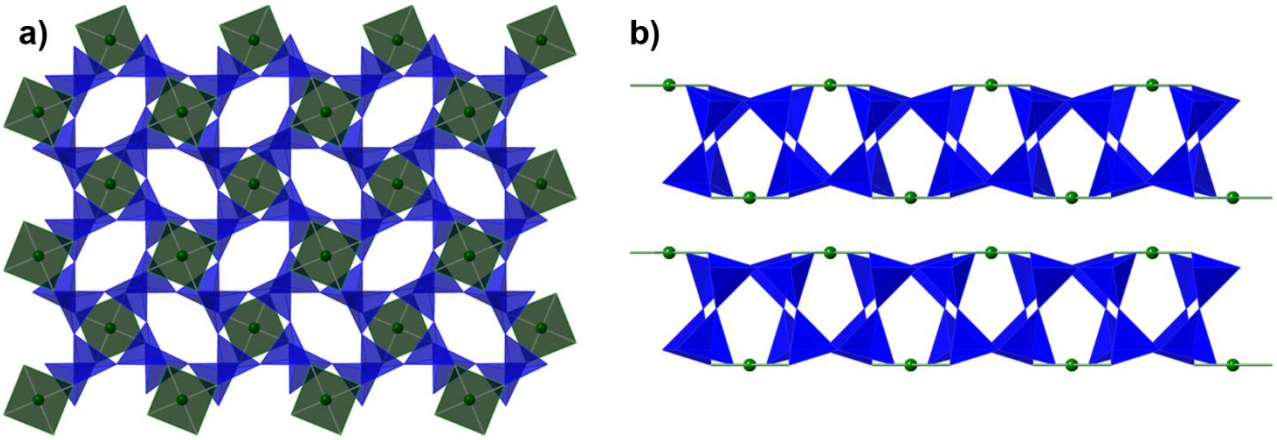

Figure 1.1. Crystal structure of $CaCuSi_4O_{10}$ shown from a) the {001} plane of the crystal and b) the {100} plane.

Pabst found that the overall properties of the different metal copper tetrasilicates are very similar in that they are all very stable to acid leaching and they have perfect cleavage along the {001} axis. However, changing the cation does lead to slight differences in the optical properties, notably, that the refractive indices for $CaCuSi_4O_{10}$ are greater than the other two.[16]

The source of the brilliant blue color that made these pigments so desirable in the ancient world is also responsible for the most interesting property of the $ACuSi_4O_{10}$ series: strong luminescence in the near-infrared.[43] As one might suspect, the reason for this photoluminescence involves the structure of the metal copper tetrasilicates. The Italian chemist G. Pozza and his collaborators determined that in $ACuSi_4O_{10}$ structure, the square planer copper is the only photoactive ion and is in D_{4h} coordination due to the Jahn-Teller effect and lattice constraints.[44] From ligand field theory, changing the symmetry from O_h to D_{4h}, splits the degenerate ground state, E_g, into A_{1g} and B_{1g} and the excited state, T_g, into B_{2g} and E_g (Figure 1.2).

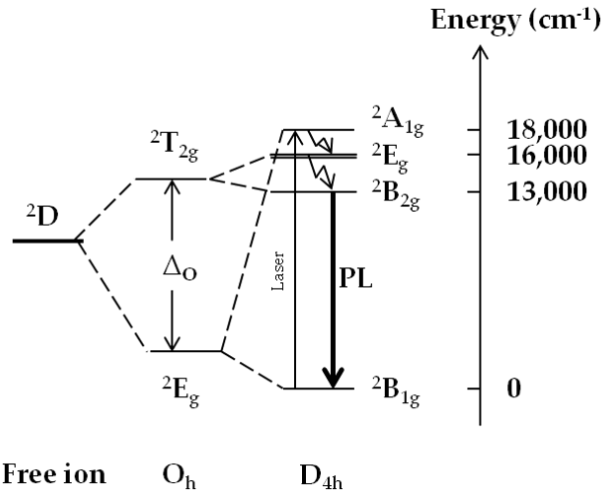

Figure 1.2. Crystal field splitting diagram for Cu^{2+}.

When the material is excited in the visible region, three transitions occur: B_{1g} to A_{1g}, E_g, and B_{2g}. The last transition is the one responsible for the emission. The emission for $CaCuSi_4O_{10}$ is a relatively sharp, symmetric band centered at around 950 nm.[45] The emission for $SrCuSi_4O_{10}$ and $BaCuSi_4O_{10}$ is redshifted to around 980 nm and 1000 nm, respectively.[45-46] The strong luminescence is extraordinarily useful for non-invasive analysis, especially when analyzing ancient paintings or artifacts where sample removal is limited or impossible.[44] Additionally, the strong luminescence has generated interest for modern applications as a sensor or a biological imaging agent.[47]

Nanostructured Materials

Nanomaterials can be classified as zero, one, or two dimensional.[48] In addition to the vast array of other exciting possibilities provided by these extraordinary materials, creating substances on the nanoscale, and especially on the two dimensional scale, opens up a world of new prospects for solution processing.[49] There are two general methods for creating two dimensional materials: top-down or bottom up approaches. Top-down approaches usually consist

of delaminating or exfoliating a bulk material into nanosheets (Figure 1.3).[49b, 50] Bottom up approaches include, but are not limited to, self-assembly[51] and templating.[52] Both of these methods will be discussed further later in this dissertation.

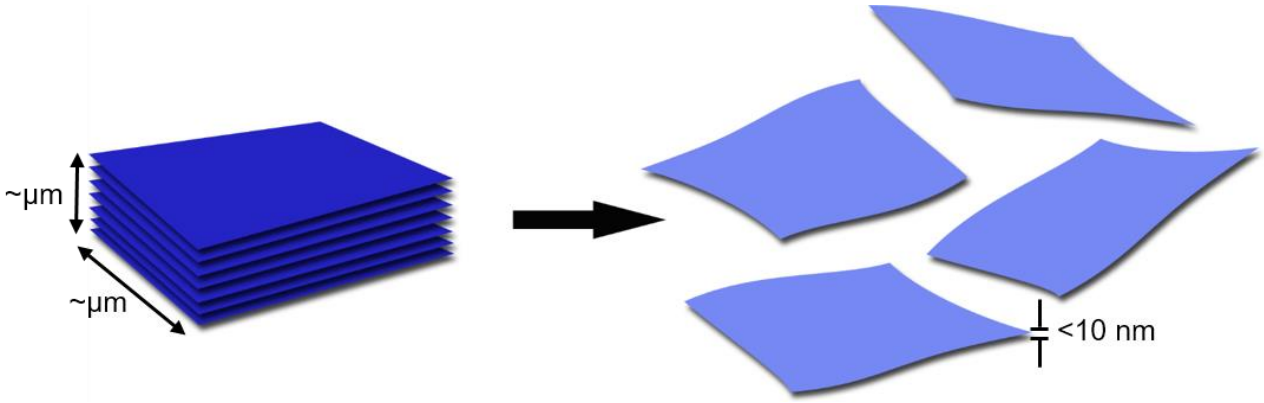

Figure 1.3. General schematic for exfoliating a layered material into mono-to-few layer nanosheets.

Our work is focused on synthetically controlling and tuning the morphology of this series on the micro and nano scales to explore the chemistry of the series and harness the near-infrared emission for applications using solution-based processing methods, as well as for use as a potential biological imaging agent.

Research Approaches

The work presented in this dissertation describes three novel methods for controlling the morphology of the metal copper tetrasilicate series on both the micro and nano scales. Chapter II describes how using solid state synthesis with nanoscale precursors creates micron-scale $ACuSi_4O_{10}$ crystals that are more uniform in size and morphology than those created through bulk solid state synthesis. Chapters III and IV discusses the hydrothermal synthesis of the $ACuSi_4O_{10}$ series. Specifically, Chapter III details the 'just right' Goldilocks nature of the hydrothermal synthesis of $CaCuSi_4O_{10}$ and Chapter IV shows how we can use hydrothermal synthesis to tune the crystal size and morphology of $SrCuSi_4O_{10}$ and $BaCuSi_4O_{10}$ by varying

precursors, time, and temperature. In Chapter V, we show that all members of the $ACuSi_4O_{10}$ series can be easily exfoliated into nanosheets using hot water and agitation and that the size of the resulting nanosheets is dependent on the size of the crystals used in the exfoliation. We further show that the NIR emission of the bulk material is retained in the nanosheet product and, thus, that the resulting colloidal dispersions can be used either as an ink for spray coating or ink jet printing or as a biological imaging agent. Overall, our work clearly shows that these remarkable blue pigments from the ancient world have a very real place in modern nanoscience as well.

References

1. Ball, P., *Bright Earth: Art and the Invention of Color*. **2001**, Farrar, Straus and Giroux.
2. Berke, H., *Angew. Chem. Int. Ed.* **2002,** *41*, 2483-2487.
3. Wiedemann, H. G.; Bayer, G., *Anal. Chem.* **1982,** *54*, 619A-628A.
4. Jaksch, H.; Seipel, W.; Weiner, K. L.; El Goresy, A., *Naturwissenschaften* **1983,** *70*, 525-535.
5. (a) Petrie, W. M. F., *Tell El Amarna*. **1894,** London; (b) Bayer, G.; Wiedemann, H. G., *Chem. Labor Betr.* **1976,** *27*, 432-7.
6. Newman, R., *A Companion to Ancient Egyptian Art*. **2014**, Wiley.
7. Mirti, P.; Appolonia, L.; Casoli, A.; Ferrari, R. P.; Laurenti, E.; Amisano Canesi, A.; Chiari, G., *Spectrochim. Acta, Part A* **1995,** *51A*, 437-46.
8. Pollio, M. V., *De architectura libri decem*. Vol. VII.
9. Secundus, G. P., *Naturalis Historia*. Vol. XXXIII.
10. Davy, H., *Philos. T. Roy. Soc.* **1815,** *105*, 97-124.
11. (a) Jope, M., The social implications of Celtic art: 600 BC to AD 600. In *The Celtic World* Green, M. J., Ed. Routledge: London **1996**; (b) Clegg, S. Blue shade hues: a study of blue pigments used by Romano-British wall-painters. University of Sussex, **2014**.
12. Fouque, F., *Bull. Soc. Chim. Fr.* **1889,** *XII*.
13. Russell, W. J., *P. Roy. Soc. Lond. A. Mat.* **1893,** XIV, 67-71.
14. Spurrell, F. C. J., *The Archaeol. J.* **1895,** *52*, 222-239.
15. Laurie, A. P.; McLintock, W. F. P.; Miles, F. D., *P. Roy. Soc. Lond. A. Mat.* **1914,** *89*, 418-429.
16. Pabst, A., *Acta Crystallogr.* **1959,** *12*, 733-9.

17. Chase, W. T., *Egyptian Blue as a Pigment and Ceramic Material*. **1971**, MIT Press: Cambridge, MA.

18. Chakoumakos, B. C.; Fernandez-Baca, J. A.; Boatner, L. A., *J. Solid State Chem.* **1993,** *103*, 105-113.

19. Bensch, W.; Schur, M., *Z. Kristallogr.* **1995**, *210*, p 530.

20. Ullrich, D., *PACT* **1987,** *17*, 323–332

21. Tite, M. S.; Bimson, M.; Cowell, M. R., *Adv. Chem. Ser.* **1984,** *205*, 215-42.

22. Pradell, T.; Salvado, N.; Hatton, G. D.; Tite, M. S., *J. Am. Ceram. Soc.* **2006,** *89*, 1426-1431.

23. Mazzocchin, G. A.; Rudello, D.; Bragato, C.; Agnoli, F., *J. Cult. Herit.* **2004,** *5*, 129-133.

24. Berke, H.; Wiedemann, H. G., *East Asia Sci. Technol. Med.*, **2000**, *17*, 94-120.

25. Ma, Q.; Portmann, A.; Ferdinand, W.; Berke, H., *Stud. Conserv.* **2006,** *51*, 81-98.

26. Bouherou, S.; Berke, H., and Wiedemann, H.G., *Chimia* **2001,** *55*, 942–951.

27. (a) Finger, L. W.; Hazen, R. M.; Hemley, R. J., *Am. Mineral.* **1989,** *74*, 952-955; (b) Tsukada, I.; Sasago, Y.; Uchinokura, K.; Zheludev, A.; Maslov, S.; Shirane, G.; Kakurai, K.; Ressouche, E., *Phys. Rev. B* **1999,** *60*, 6601-6607.

28. FitzHugh, E. W.; Zycherman, L. A., *Stud. Conserv.* **1983,** *28*, 15-23.

29. Qin, Y.; Wang, Y. H.; Chen, X.; Li, H. M.; Li, X. L., *Archaeometry* **2015**, early view.

30. Berke, H., *Chem. Soc. Rev.* **2007,** *36*, 15-30.

31. FitzHugh, E. W.; Zycherman, L. A., *Stud. Conserv.* **1992,** *37*, 145-54.

32. Janczak, J.; Kubiak, R., *Acta Crystallogr. Sect. C: Cryst. Struct. Commun.* **1992,** *48*, 1299-1301.

33. Chen, Y.; Shang, M. Y.; Wu, X. F.; Feng, S. H., *Crystengcomm* **2014,** *16*, 5418-5423.

34. Kar, J. K.; Stevens, R.; Bowen, C. R., *J. Alloys Compd.* **2008,** *461*, 77-84.

35. Chen, W.; Shi, Y.; Chen, Z.; Sang, X.; Zheng, S.; Liu, X.; Qiu, J., *J. Phys. Chem. C* **2015**, *119*, 20571-20577.

36. Knight, K. S.; Henderson, C. M. B.; Clark, S. M., *Eur. J. Mineral.* **2010,** *22*, 411-423.

37. Jose, S.; Reddy, M. L., *Dyes Pigment.* **2013,** *98*, 540-546.

38. (a) Giester, G.; Rieck, B., *Mineral. Mag.* **1994,** *58*, 663-670; (b) Giester, G.; Rieck, B., *Mineral. Mag.* **1996,** *60*, 795-798; (c) Minguzzi, C., *Period. Mineral. Mag.* **1938,** *9*, 333-345.

39. A., M. F. P., *Am. Mineral.* **1962,** *47*, 409-411.

40. Eastaugh, N. W., V.; Chaplin, T.; Siddall, R., *The Pigment Compendium: A Dictionary of Historical Pigments*. Butterworth-Heinemann: Oxford, U.K., 2005.

41. (a) Pabst, A., *Am. Mineral.* **1958,** *43*, 970-980; (b) Pabst, A., *Am. Mineral.* **1943,** *28*, 372-390.

42. Miletich, R.; Allan, D. R.; Angel, R. J., *Am. Mineral.* **1997,** *82*, 697-707.

43. Ajò, D.; Chiari, G.; De Zuane, F.; Favaro, M.; Bertolin, M., *Art '96 proceedings.* **1996,** *5th International Conference on Non-destructive Testing, Microanalytical Methods and Environmental Evaluation for Study and Conservation of Works of Art, Budapest, September 24–28,* 33-47.

44. Pozza, G.; Ajò, D.; Chiari, G.; De Zuane, F.; Favaro, M., *J. Cult. Herit.* **2000,** *1*, 393-398.

45. Verri, G., *Anal. Bioanal. Chem.* **2009,** *394*, 1011-1021.

46. Borisov, S. M.; Würth, C.; Resch-Genger, U.; Klimant, I., *Anal. Chem.* **2013,** *85*, 9371-9377.

47. Accorsi, G.; Verri, G.; Bolognesi, M.; Armaroli, N.; Clementi, C.; Miliani, C.; Romani, A., *Chem. Commun.* **2009,** *23*, 3392-3394.

48. Vollath, D., *Nanomaterials: An Introduction to Synthesis, Properties and Applications*. 2nd ed., **2013**, Wiley.

49. (a) Schwartz, R. W., Manoj, N., Chemical Solution Deposition—Basic Principles In *Solution Processing of Inorganic Materials*, Mitzi, D., Ed. Wiely: 2009; (b) Shibata, T.; Takano, H.; Ebina, Y.; Kim, D. S.; Ozawa, T. C.; Akatsuka, K.; Ohnishi, T.; Takada, K.; Kogure, T.; Sasaki, T., *J. Mater. Chem. C* **2014,** *2*, 441-449.

50. Novoselov, K. S.; Geim, A. K.; Morozov, S. V.; Jiang, D.; Zhang, Y.; Dubonos, S. V.; Grigorieva, I. V.; Firsov, A. A., *Science* **2004,** *306*, 666-669.

51. Wang, Z. C.; Li, Z. Y.; Medforth, C. J.; Shelnutt, J. A., *J. Am. Chem. Soc.* **2007,** *129*, 2440-2441.

52. Pope, T. R.; Lassig, M. N.; Neher, G.; Weimar, R. D., III; Salguero, T. T., *J. Mater. Chem. C* **2014,** *2*, 3223-3230.

CHAPTER 2

SIZE CONTROL OF THE METAL COPPER TETRASILICATE SERIES BY MEANS OF SOLID STATE SYNTHESIS WITH NANOSCALE PRECURSORS

Darrah Johnson-McDaniel and Tina T. Salguero. To be submitted to *Crystal Engineering Communication.*

Abstract

The $ACuSi_4O_{10}$ series has been traditionally synthesized using either melt-flux or solid state methods. These methods typically produce relatively large, dark blue crystals or light blue polycrystalline aggregates of random size and shape, require high temperatures or harsh fluxes, and lack control over the final size and morphology. Using nanoscale precursors and common solid state synthetic techniques, we have lowered the initial reaction temperatures for the $ACuSi_4O_{10}$ series by over 200 °C and are able to create brighter blues when compared to solid state products synthesized with bulk precursors. With the nanoscale reactants, we can form $CaCuSi_4O_{10}$ and $SrCuSi_4O_{10}$ into crystals that have sub-micron grain size and $BaCuSi_4O_{10}$ into sub-micron sized single crystals in the ideal crystal shape. By tailoring the initial particle size, we have provided a first step to controlling the final size and morphology of the $ACuSi_4O_{10}$ series though simple solid state synthesis.

Introduction

Nanomaterials are much more reactive than their bulk counterparts due to the increased amount of exposed surface area and number of interfaces which lower the reaction point of the materials.[1] The most common route to reducing the size of reactants is through mechanical ball milling, which decreases the overall particle size and grain size.[2] However, there is a difference between milling bulk materials and using nanomaterials as precursors. While milling bulk materials easily reduces the grain size of the particles to the nanoscale, only rarely does it reduce the overall particle size down to the nanoscale. Therefore, mechanically milled reactants cannot be expected to be behave in a similar manner to nanoscale precursors. Using nanoscale precursors to tailor the product size and morphology has been relatively unexplored. Nanoparticles of perovskites have been synthesized by solid state reaction with nanoscale precursors[3] or by annealing amorphous nanoparticle precursors[4]. In both cases the nanoscale morphology is maintained throughout the process. Additionally, the nano-morphology of the final product in alloys and other metal oxides has been maintained by using nanoscale precursers.[5]

The $ACuSi_4O_{10}$ series, host to brilliant blue pigments, was traditionally synthesized using flux-based or solid state methods.[6] The flux-based method typically produces large, dark blue crystals that fragment on removal from the crucible and requires the use of harsh fluxes and high temperatures. The solid state method produces light blue polycrystalline aggregates of random size and shape and still requires high temperatures. Furthermore, neither of these methods provides a great deal of control over the final size or morphology of the products. Forming the $ACuSi_4O_{10}$ series on the micron or nanoscale, enables us to take full advantage of its emission in the near-infrared for such potential applications as security inks or biological imaging. Here we

show that using nanoscale precursors with simple solid state synthesis is an important first step to controlling the final size and morphology the $ACuSi_4O_{10}$ series.

Experimental

Solid State Synthesis: ACO_3 nanoparticles were synthesized using the procedure developed by M. Davidson and coworkers at The University of Georgia Department of Chemistry.

$CaCuSi_4O_{10}$: 0.067 g (0.665 mmol) of $CaCO_3$ (Sigma Aldrich, BioXtra, > 99.0% purity) or $CaCO_3$ nanoparticles or 0.037 g (0.660 mmol) CaO nanoparticles (Sigma Aldrich, 98% purity, <160 nm particle size), 0.160 g (2.65 mmol) of SiO_2 (Sigma Aldrich, 99% purity) or SiO_2 nanoparticles (US Nano 99.5+% purity, 15-20 nm particle size), and 0.053 g (0.665 mmol) CuO (Sigma Aldrich, 99.99% trace metals basis) or CuO nanoparticles (US Nano, 99.95% purity, 25-55 nm particle size) were ground until homogeneous in an agate mortar and pestle. The color of the resulting powder was a dull gray. The powder was then either used as is, or was uniaxially pressed into a 1 x 13 mm pellet using 5 tons of pressure. The resulting powder or pellet was then transferred into a platinum crucible and heated in a box furnace for 16 h. The bulk reaction was heated to a temperature of 1050 ˚C; the nanoscale reactions were heated at varying temperatures. The ramp rate for all reactions was 5 °C per min.

$SrCuSi_4O_{10}$: 0.087 g (0.590 mmol) of $SrCO_3$ (Sigma Aldrich, ≥ 99.9% trace metals basis purity) or $SrCO_3$ nanoparticles, 0.142 g (2.36 mmol) of SiO_2 (Sigma Aldrich, 99% purity) or SiO_2 nanoparticles (US Nano 99.5+% purity, 15-20 nm particle size), and 0.047 g (0.590 mmol) CuO (Sigma Aldrich, 99.99% trace metals basis) or CuO nanoparticles (US Nano, 99.95% purity, 25-55 nm particle size) were ground until homogeneous in an agate mortar and pestle. The color of the resulting powder was a dull gray. The powder was then used as is, or uniaxially pressed into

a 1 x 13 mm pellet using 5 tons of pressure. The resulting powder or pellet was then transferred into a platinum crucible and heated in a box furnace for 16 h. The bulk reaction was heated to a temperature of 1000 °C; the nanoscale reactions were heated at varying temperatures. The ramp rate for all reactions was 5 °C per min.

$BaCuSi_4O_{10}$: 0.104 g (0.528 mmol) of $BaCO_3$ (SREM Chemicals, 99.9% purity) or $BaCO_3$ nanoparticles, 0.127 g (2.11 mmol) of SiO_2 (Sigma Aldrich, 99% purity) or SiO_2 nanoparticles (US Nano 99.5+% purity, 15-20 nm particle size), and 0.042 g (0.528 mmol) CuO (Sigma Aldrich, 99.99% trace metals basis) or CuO nanoparticles (US Nano, 99.95% purity, 25-55 nm particle size) were ground until homogeneous in an agate mortar and pestle. The color of the resulting powder was a dull gray. The powder was then either used as is, or was uniaxially pressed into a 1 x 13 mm pellet using 5 tons of pressure. The resulting powder or pellet was then transferred into a platinum crucible and heated in a box furnace for 16 h. The bulk reaction was heated to a temperature of 950 °C; the nanoscale reactions were heated at varying temperatures. The ramp rate for all reactions was 5 °C per min.

Characterization: The identity of the synthesized pigments was confirmed using a Bruker D8-Advance powder X-ray diffractometer (Co-Kα radiation source) operated at 40 mA and 40 kV. The PXRD patterns were recorded over the 2θ range of 10−70° with a scanning rate of 0.1 sec $step^{-1}$. The morphology of the crystals was examined using a FEI Inspect F field emission gun scanning electron microscope (SEM) operated at 20 keV. The samples were prepared for SEM by sprinkling the powders on carbon sticky tape and then coating with gold. Thermogravimetric analysis (TGA) was carried out using a Mettler Toledo Thermogravimetric Analyzer. The samples were all run in air from 25-1000 °C at a rate of 5 °C/min, excluding the bulk reactants for the preparation of $BaCuSi_4O_{10}$, which was run at 10 °C/min.

Results and Discussion

The $ACuSi_4O_{10}$ series can be readily synthesized using solid state methods, with results shown below.[6c] For comparison purposes, Figure 2.1 shows optical and scanning electron microscopy (SEM) images of all three solid state products: $CaCuSi_4O_{10}$, $SrCuSi_4O_{10}$, and $BaCuSi_4O_{10}$. All three products are a similar pale blue in color and are comprised of relatively small crystals with random size and morphology. The temperature required for complete reaction decreases as we proceed down the alkaline earth series, from 1050 °C for $CaCuSi_4O_{10}$, to 1000 °C for $SrCuSi_4O_{10}$, and finally to 950 °C for $BaCuSi_4O_{10}$.

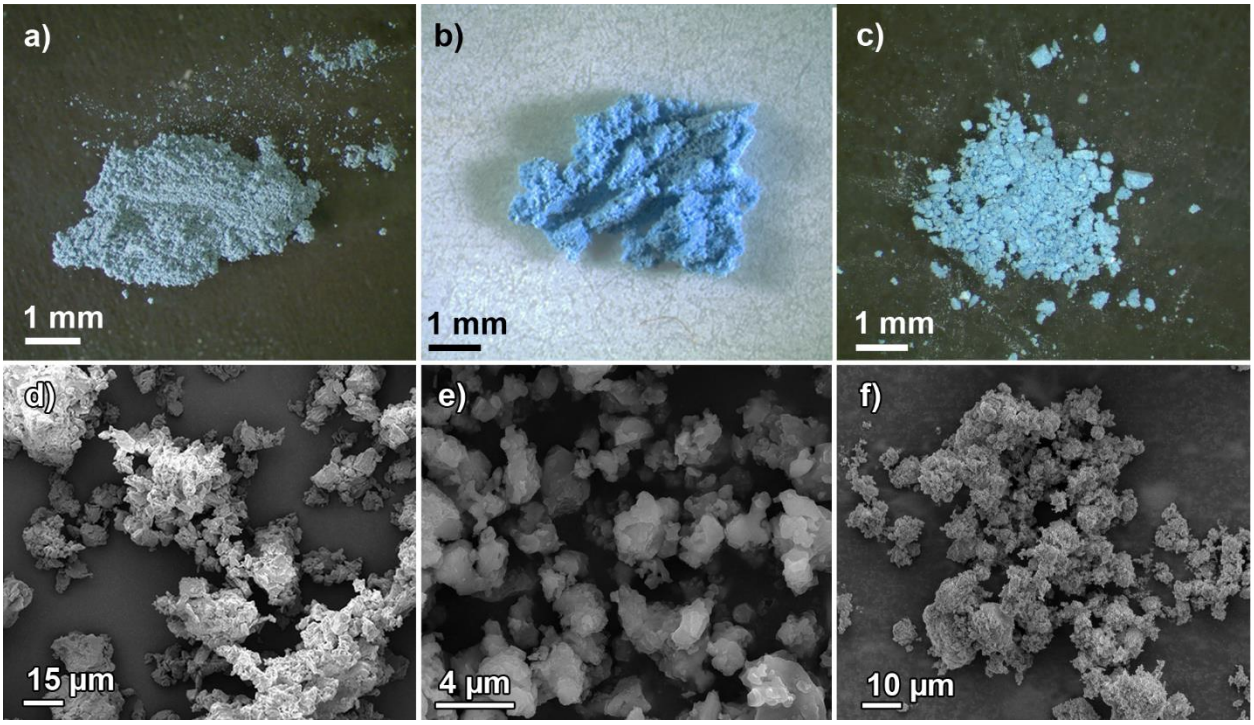

Figure 2.1. $ACuSi_4O_{10}$ series synthesized using standard solid state methods. Optical images of a) $CaCuSi_4O_{10}$, b) $SrCuSi_4O_{10}$, and c) $BaCuSi_4O_{10}$ show the pale blue color of the products. The corresponding SEM images in d-f show the relatively small crystal size.

We confirmed the composition of the products using powder X-ray diffraction (PXRD) (Figure 2.2). All three of the products matched their corresponding reference patterns well with the exception of $CaCuSi_4O_{10}$, which exhibited two small peaks corresponding to unreacted SiO_2.

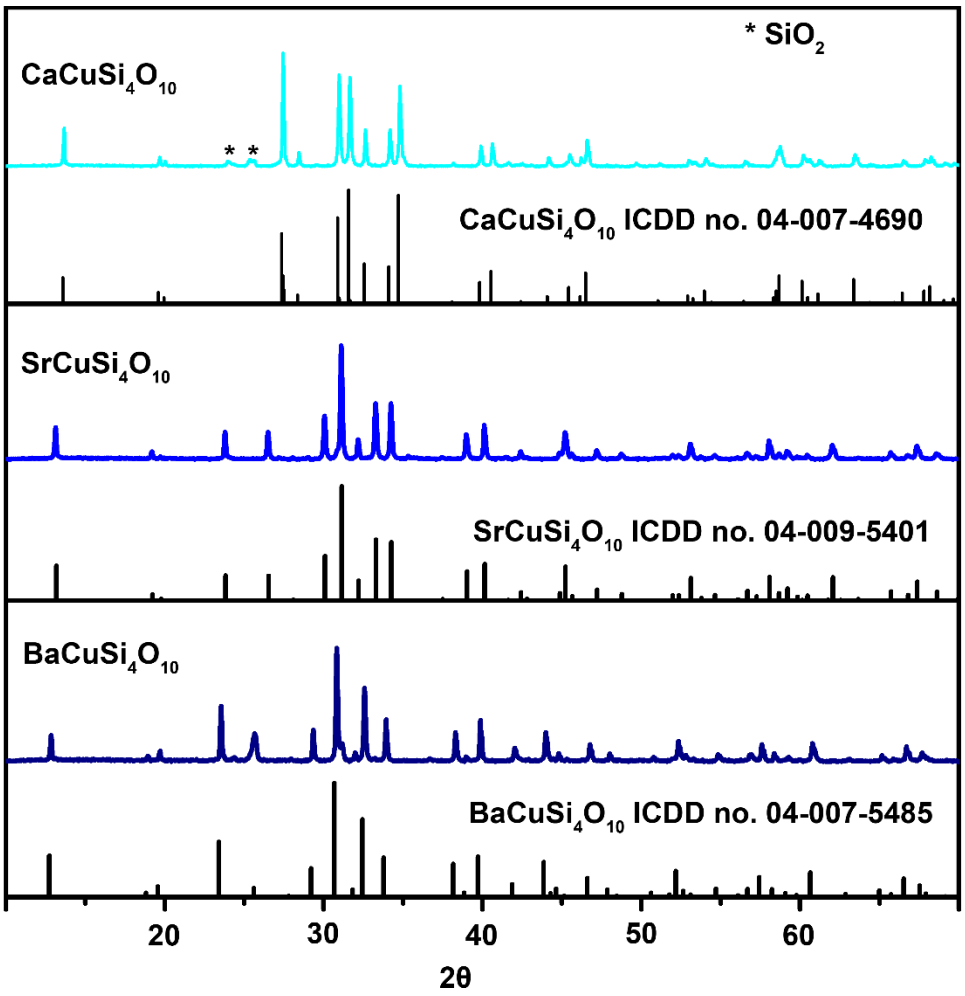

Figure 2.2. PXRD patterns of $ACuSi_4O_{10}$ series synthesized by the solid state method with matching reference patterns, * indicates SiO_2.

Synthesizing the $ACuSi_4O_{10}$ series via the solid state method is a relatively simple process. However, the solid state synthesis method with bulk precursors requires high temperatures and still does not produce the vivid blue colors that are characteristic of the materials. Nor does it make sub-micron or nanoscale crystals with consistent size and morphology. Our research aims to change this. We sought a way to produce sub-micron or nanoscale results, while not losing methodological simplicity.

To that end, we have used starting materials that are all on the nanoscale in order to lower the reaction temperature and potentially create another route to micron or nano-sized $ACuSi_4O_{10}$

by the reactants acting as a template for the final product. Starting with $CaCuSi_4O_{10}$ and using nanoparticle analogues of the bulk reactants, we performed a series of experiments to determine the optimum conditions for the reactions. We started with a temperature study from 800-1000 ˚C (Figure 2.3) in order to determine the temperature required for formation of $CaCuSi_4O_{10}$ using nanoscale precursors.

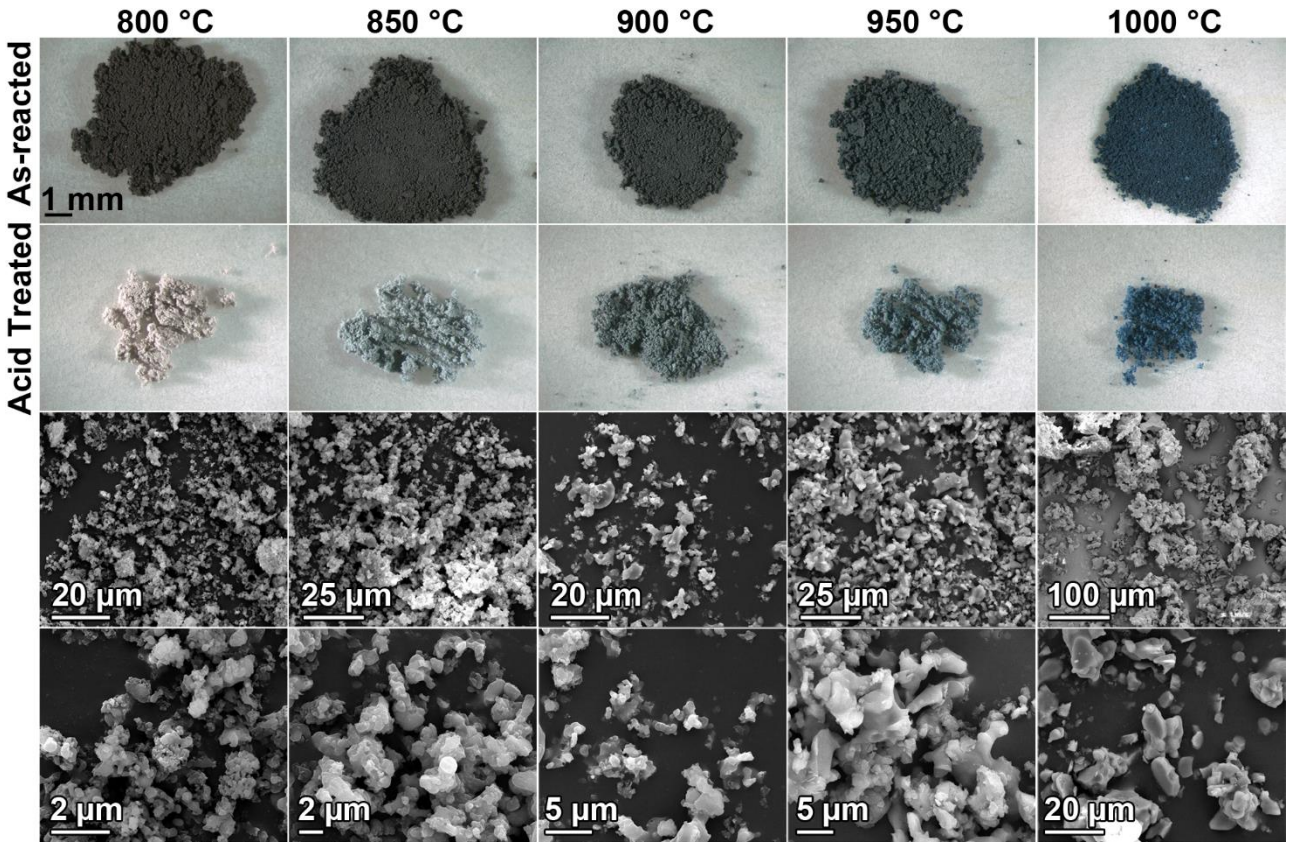

Figure 2.3. Top two rows show optical images of the as-reacted and acid treated products of $CaCuSi_4O_{10}$ solid state reactions using nano precursors reacted from 800-1000 °C. Bottom two rows show SEM images of the products after acid treatment.

At 800 ˚C, the resulting powder was black in color, changing to a light gray after acid treatment. By PXRD, the as-reacted powder was comprised of SiO_2, CuO, and $CaSiO_3$, not the desired $CaCuSi_4O_{10}$ (Figure 2.4). After acid treatment, the product was just SiO_2 (Figure 2.5). SEM showed crystals of random shape, which were all under approximately 2 µm in size. The

initial product was still a black color at 850 °C (Figure 2.3), but after acid treatment a slight, but noticeable, bluish tinge appeared indicating the formation of $CaCuSi_4O_{10}$. This was confirmed by PXRD, which revealed the presence of $CaCuSi_4O_{10}$ in addition to SiO_2 and CuO (Figures 2.4 and 2.5). From 900-1000 °C, the amount of $CaCuSi_4O_{10}$ present varied directly with temperature, increasing as the temperature increased (Figures 2.5). Additionally, the products were a more obvious blue and, by SEM, had a larger average crystal size, increasing from ~ 2 μm to ~10 μm (Figure 2.4). The increase in crystal size accounts for the increased blue color of the products.[7] The gray-black color present at lower temperatures can potentially be explained as a consequence of the high surface area of the nanoparticles, whereby the CuO 'coats' the other reactants and stops the reaction from going to completion which led to the continued persistence of the gray color. Even at 950 °C, there was still a dullness to the blue color prior to acid treatment. Acid treatment does partially remove the unreacted CuO, (Figure 2.5), which suggests the validity of the theory.

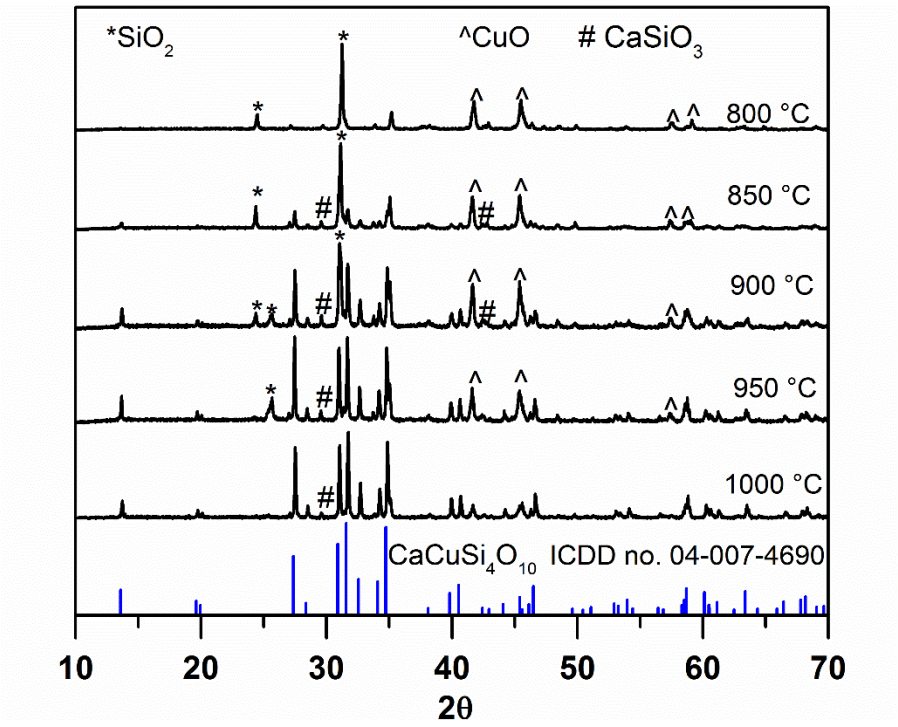

Figure 2.4. PXRD of $CaCuSi_4O_{10}$ solid state reactions using nano precursors reacted from 800-1000 °C with $CaCuSi_4O_{10}$ reference pattern.

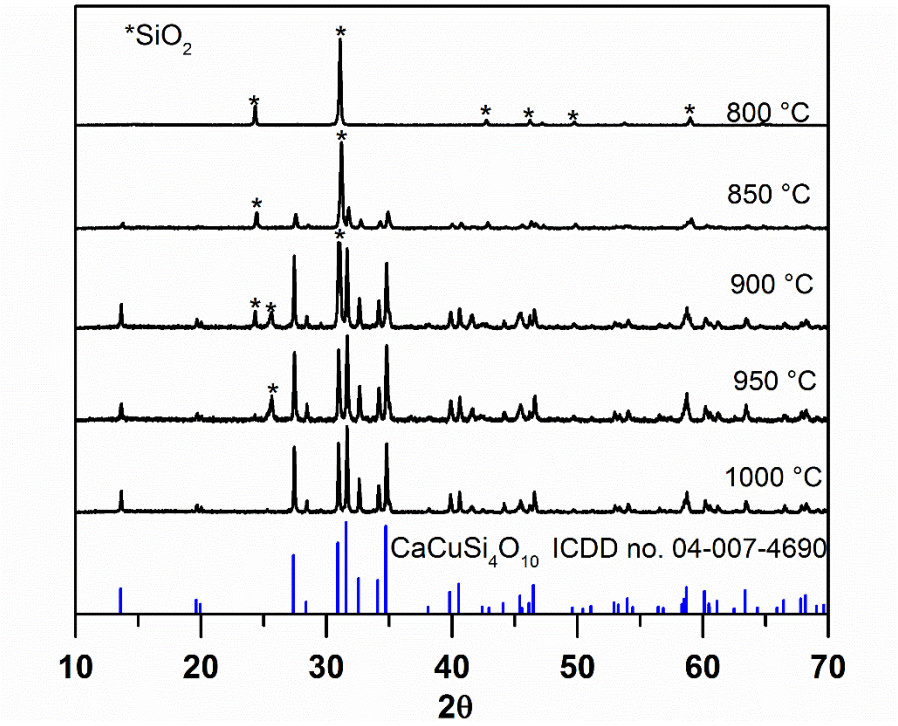

Figure 2.5. PXRD of $CaCuSi_4O_{10}$ solid state reactions using nano precursors reacted from 800-1000 °C after acid treatment with $CaCuSi_4O_{10}$ reference pattern.

In order to further understand the formation of $CaCuSi_4O_{10}$ using nano precursors, we performed thermogravimetric analysis (TGA) on the nanoscale $CaCO_3$-CuO-SiO_2 mixture as well as the SiO_2 and CuO nanoparticles and, for comparison, bulk $CaCO_3$-CuO-SiO_2 mixture (Figure 2.6).

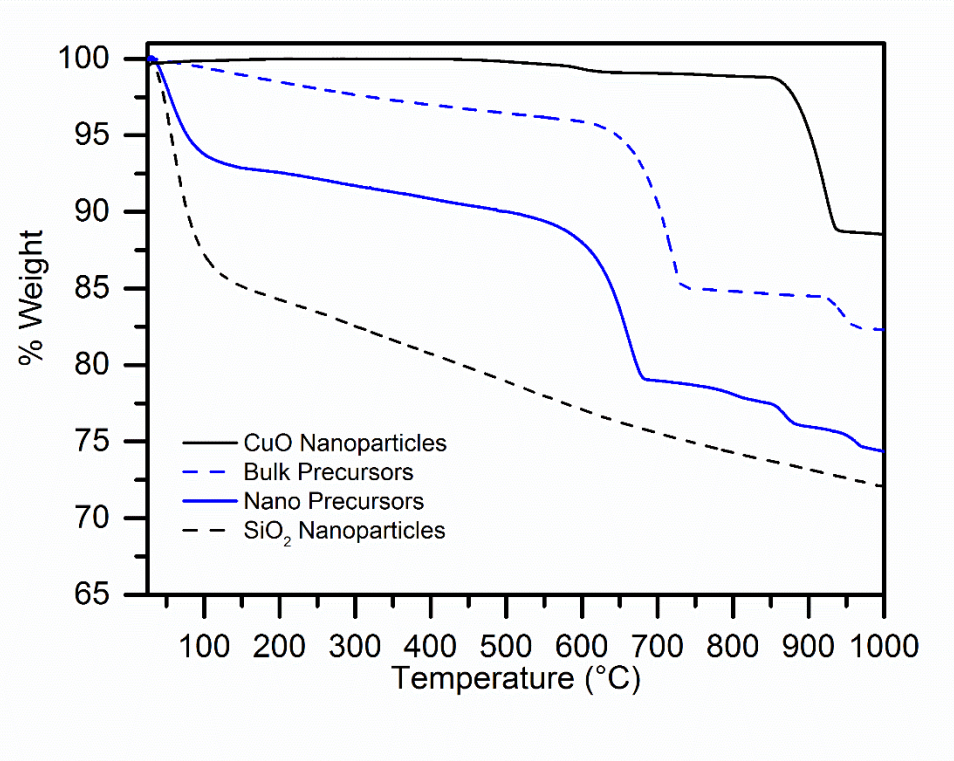

Figure 2.6. TGA curves of bulk and nanoscale $CaCuSi_4O_{10}$ reaction precursors and SiO_2 and CuO nanoparticles heated in air from 25-1000 ˚C at 5 ˚C/min.

Examining the nanoscale reaction in air from 25-1000 °C at the same heating rate of 5 °C/min, reveals several points of interest: (1) We see that below 150 °C there was a relatively large weight loss of ~7.3 %. The most likely cause of this loss is the absorption of residual water by the nanoscale SiO_2. (2) The largest weight loss, of ~10.8 %, occurred between 500-650 °C, corresponding to the decomposition of $CaCO_3$ into CaO and CO_2. (3) Between 850-1000 °C, there were two small drops in the thermograph. $CaCuSi_4O_{10}$ is known to decompose into SiO_2 and a mixture of CuO and Cu_2O at temperatures above 1000 °C and that decomposition is represented by two small drops in the thermograph.[8] Here, using the nanoscale reactants shifted the decomposition of the carbonate and the copper oxide to lower temperatures when compared to the bulk mixture, thus further confirming the increased reactivity of the nanoscale precursors.

In order to further test if using nanoscale precursors enhanced the reactivity, we used these precursors in conjunction with pelleting. Pelleting is known to decrease the interpartical void space in addition to increasing surface free energy, thus further increasing the reaction rate.[9]

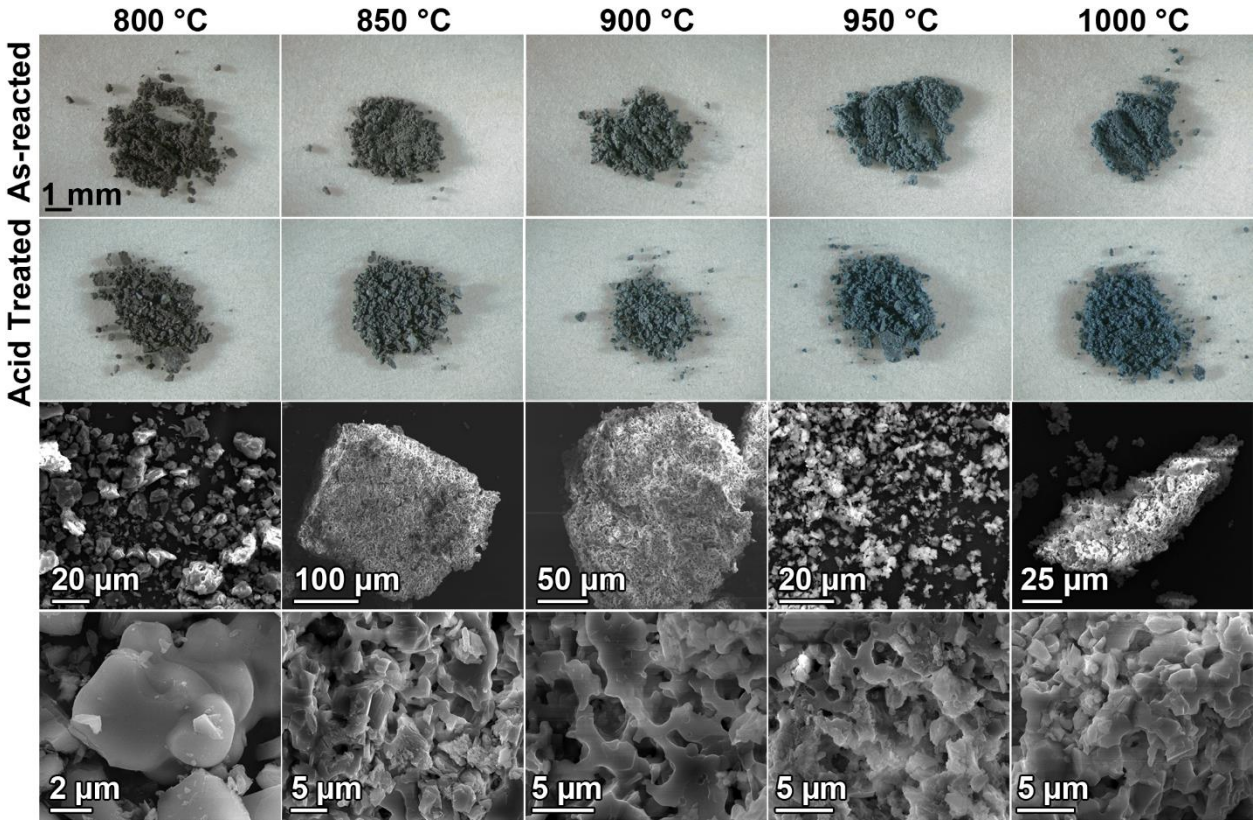

Figure 2.7. Top two rows show optical images of the as-reacted and acid treated products of $CaCuSi_4O_{10}$ solid state reactions using pelletized nano precursors reacted from 800-1000 °C. Bottom two rows show SEM images of the products after acid treatment.

After pressing the nanopowders into pellets, we again carried out a temperature study from 800-1000 ˚C (Figure 2.7) At 800 ˚C, again the resulting powder was a black color, which changed to gray after acid treatment. This time, however, we did see a small amount of $CaCuSi_4O_{10}$ by powder diffraction (Figures 2.8 and 2.9), though the product was still mostly comprised of SiO_2 and CuO. SEM showed much larger crystals than the reaction with loose powder. At 850 ˚C, again the initial product was still black, but after acid treatment it was a blue gray (Figure 2.7), the PXRD pattern was similar to the reaction at 800 ˚C. SEM showed that the

$CaCuSi_4O_{10}$ crystals were starting to sinter together into larger crystals, forming a porous network (Figure. 2.7) and there is a larger percentage of $CaCuSi_4O_{10}$ present in the PXRD pattern (Figure 2.8). By 900 ˚C, the product seemed to be mostly $CaCuSi_4O_{10}$, with a small amount of unreacted CuO (Figure 2.8). At 950-1000 C, the product was all $CaCuSi_4O_{10}$. To further pinpoint the temperature of formation, we extended the temperature study: at 750 ˚C, the reaction is mostly comprised of $CaSiO_3$, SiO_2, and CuO (Figure 2.8), with a very small amount of $CaCuSi_4O_{10}$ (Figures 2.8 and 2.9), and by 700 ˚C, there is no formation of $CaCuSi_4O_{10}$. The morphology of the products from 900-1000 ˚C is similar to that of the 850 ˚C reaction, a porous network of sintered crystals. Again, we saw that the color of the product is a more obvious blue with higher reaction temperatures, and we saw that the average crystal size increased as well, accounting for the intensification in color. Pressing the nanopowders into pellets did indeed increase the reaction rate and lower the temperature for formation of $CaCuSi_4O_{10}$ down to 750 ˚C (Figure 2.8). Additionally, pelletizing the reactants increased the crystallinity of the products, prevented the formation of the $CaSiO_3$ impurity that was present in the loose powders from 800-1000 ˚C, and formed more porous products than those synthesized from loose powders.

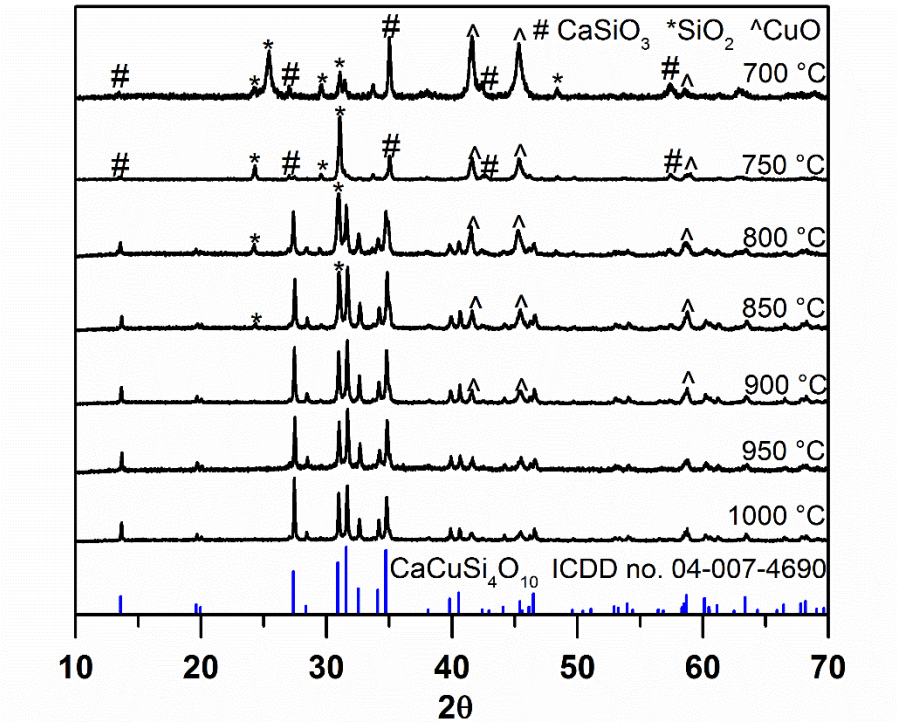

Figure 2.8. PXRD of $CaCuSi_4O_{10}$ solid state reactions using pelletized nano precursors reacted from 700-1000 °C with $CaCuSi_4O_{10}$ reference pattern.

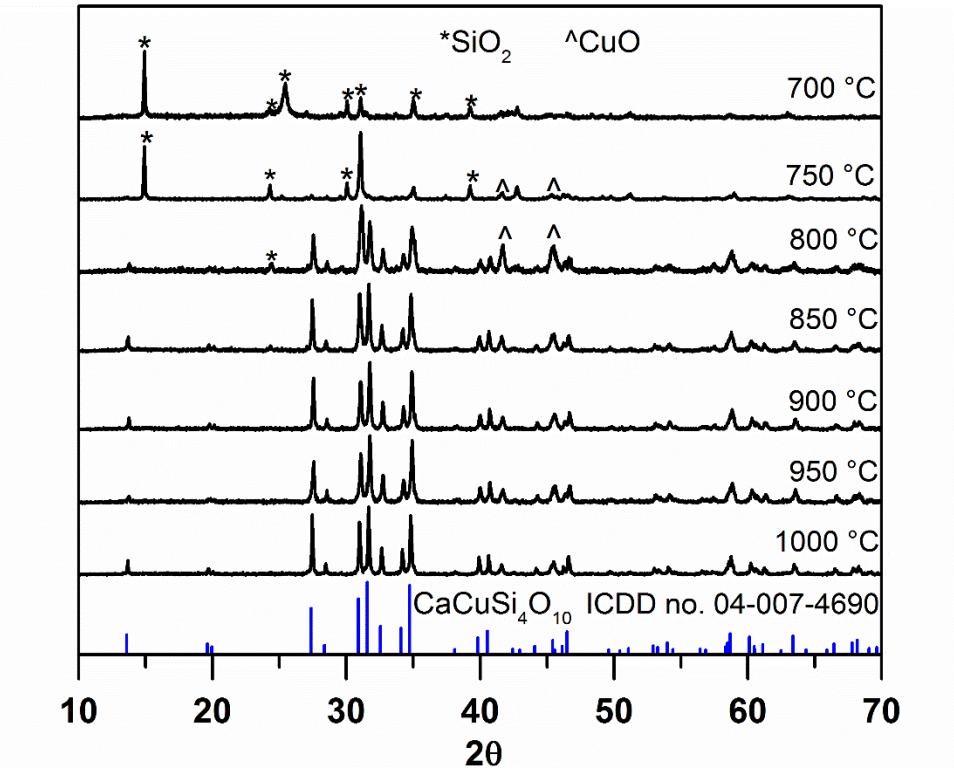

Figure 2.9. PXRD of $CaCuSi_4O_{10}$ solid state reactions using pelletized nano precursors reacted from 700-1000 °C after acid treatment with $CaCuSi_4O_{10}$ reference pattern.

Another potential roadblock in the templating effect of the nanosized precursors is that $CaCO_3$ might no longer be on the nanoscale if it converts to CaO before reacting with the other reagents. In order to mitigate that, we used commercial nanoparticles of CaO in the place of the synthesized $CaCO_3$ nanoparticles.

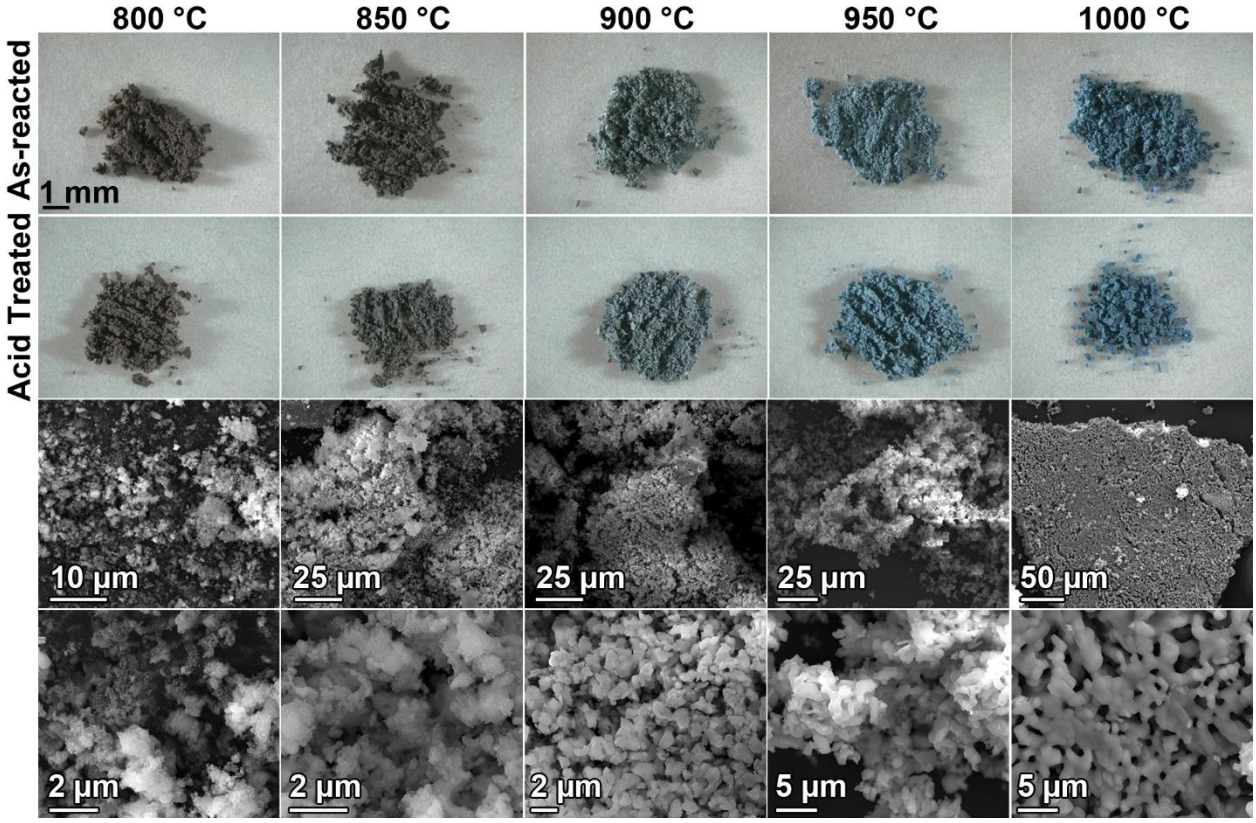

Figure 2.10. Top two rows show optical images of the as-reacted and acid treated products of $CaCuSi_4O_{10}$ solid state reactions using nano precursors with CaO nanoparticles reacted from 800-1000 °C. Bottom two rows show SEM images of the products after acid treatment.

We carried out the same temperature study as before from 800-1000 °C, only this time substituting CaO nanoparticles for the $CaCO_3$ nanoparticles (Figure 2.10). At 800 ˚C, the resulting powder was still black in color, though it changed to gray after acid treatment. PXRD analysis showed the product to be predominantly SiO_2 and CuO (Figure 2.11). At 850 ˚C, similarly to what we had previously observed for the loose powder reactions with $CaCO_3$, the initial product was still black, but after acid treatment it had turned a gray color (Figure 2.10) and there was very little, if any $CaCuSi_4O_{10}$ present (Figure 2.11). By 900˚C, the product was mostly $CaCuSi_4O_{10}$; however, in addition to the unreacted CuO, there was a different form of SiO_2 present as an impurity through 1000 ˚C that persisted even after acid treatment (Figures 2.11 and 2.12). The morphology by SEM was uniform micron size crystals that sintered together at

temperatures above 900 °C forming a porous network (Figure 2.10). Again, we saw that the color of the product was a more noticeable blue with higher reaction temperatures, and we saw that the average crystal size was larger than in the lower temperature reactions, accounting for the increase in blueness. Using CaO nanoparticles in the place of $CaCO_3$ nanoparticles did not increase the reactivity enough to synthesize $CaCuSi_4O_{10}$ at lower temperatures, however it did form smaller, more uniform crystals in a porous network at higher temperatures providing a more obvious blue color.

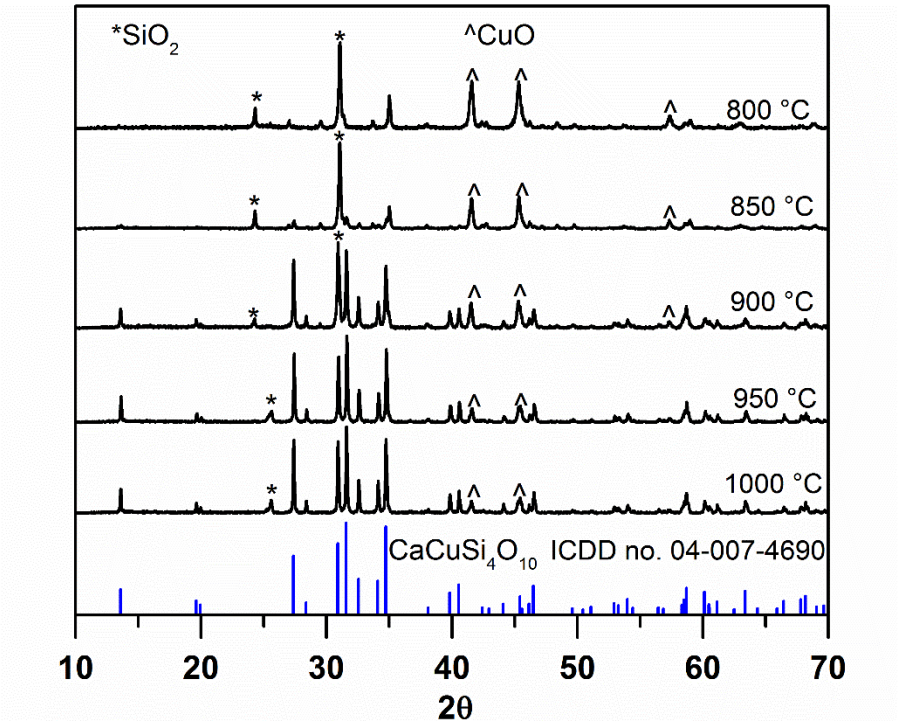

Figure 2.11. PXRD patterns of $CaCuSi_4O_{10}$ solid state reactions using nano precursors with CaO nanoparticles reacted from 800-1000 °C with $CaCuSi_4O_{10}$ reference pattern.

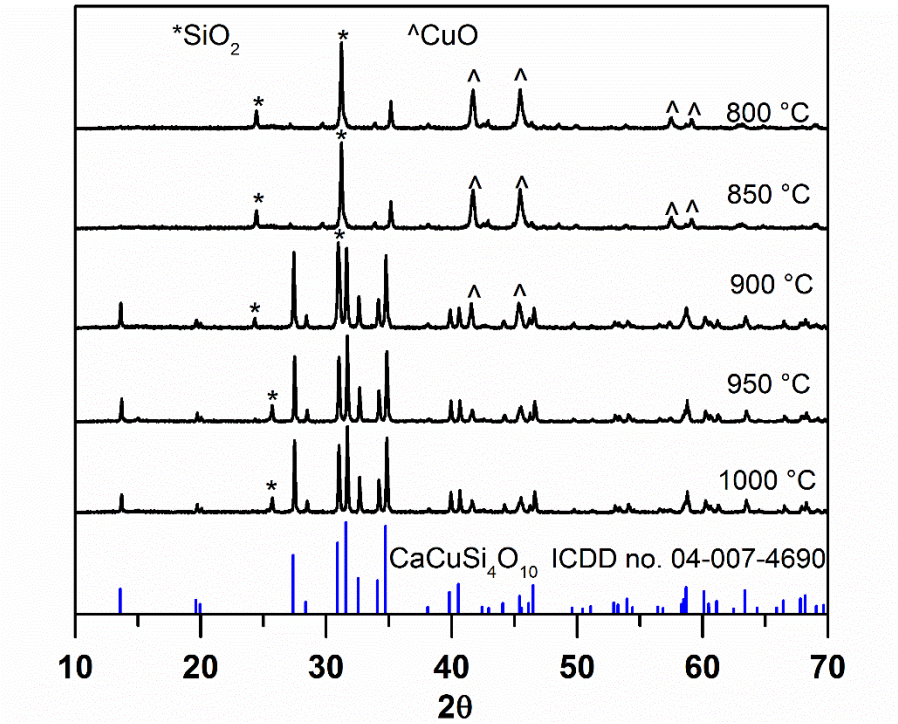

Figure 2.12. PXRD patterns of $CaCuSi_4O_{10}$ solid state reactions using nano precursors with CaO nanopaticles reacted from 800-1000 °C after acid treatment with $CaCuSi_4O_{10}$ reference pattern.

In order to improve the relatively sluggish reactivity of $CaCuSi_4O_{10}$ synthesized using CaO nanoparticles, we pressed all the powders into pellets and then repeated the temperature study (Figure 2.13).

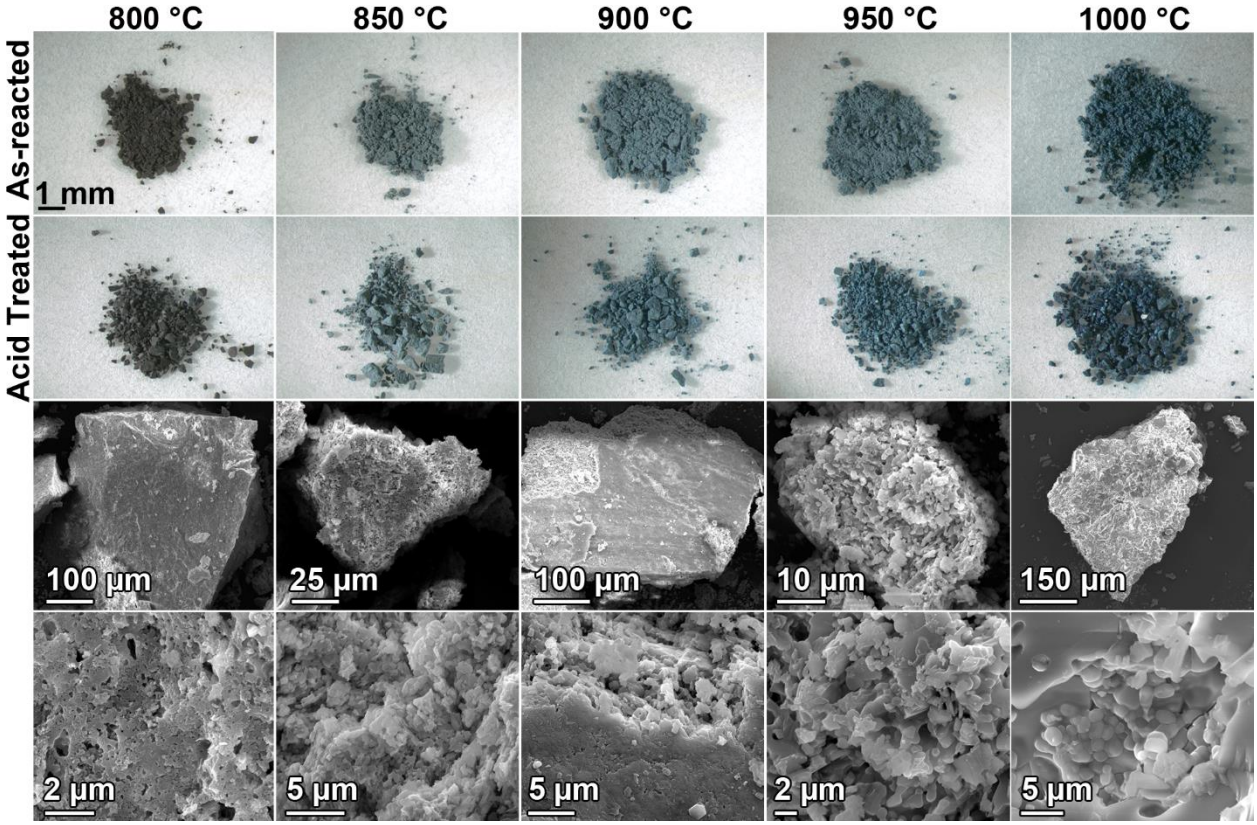

Figure 2.13. Top two rows show optical images of the as-reacted and acid treated products of $CaCuSi_4O_{10}$ solid state reactions using pelletized nano precursors reacted from 800-1000 °C. Bottom two rows show SEM images of the products after acid treatment.

At 800 ˚C, the resulting powder was still black in color, which changed to gray after acid treatment. By PXRD, the product was comprised of mostly SiO_2 and CuO with a very small amount of $CaCuSi_4O_{10}$ and $CaSiO_3$ (Figure 2.14); after acid treatment, the $CaCuSi_4O_{10}$ peaks are more apparent (Figure 2.15). At 850 ˚C, the initial product was a blue-gray and had a greater amount of $CaCuSi_4O_{10}$, after acid treatment it was a slightly lighter blue-gray (Figure 2.13). SEM showed that the morphology of product was comprised of small sub-micron crystals that were sintered together to form the larger crystals. By 900˚C, the product was completely $CaCuSi_4O_{10}$, and by SEM the crystals were slightly larger (Figures 2.13 and 2.14). From 900-950 ˚C, a crust appeared to have formed on the surface of the crystals, perhaps due to the surface of the pellet sintering together more rapidly than the inside of the pellet. By 1000 ˚C, the crystals

were on the micron scale and were starting to form smooth single crystals. Again, we observed that the color of the product was a more obvious blue with higher reaction temperatures, and we saw that the average crystal size was larger as well, accounting for the increased color intensity. Intriguingly, these samples were much less porous than those synthesized with the loose powders.

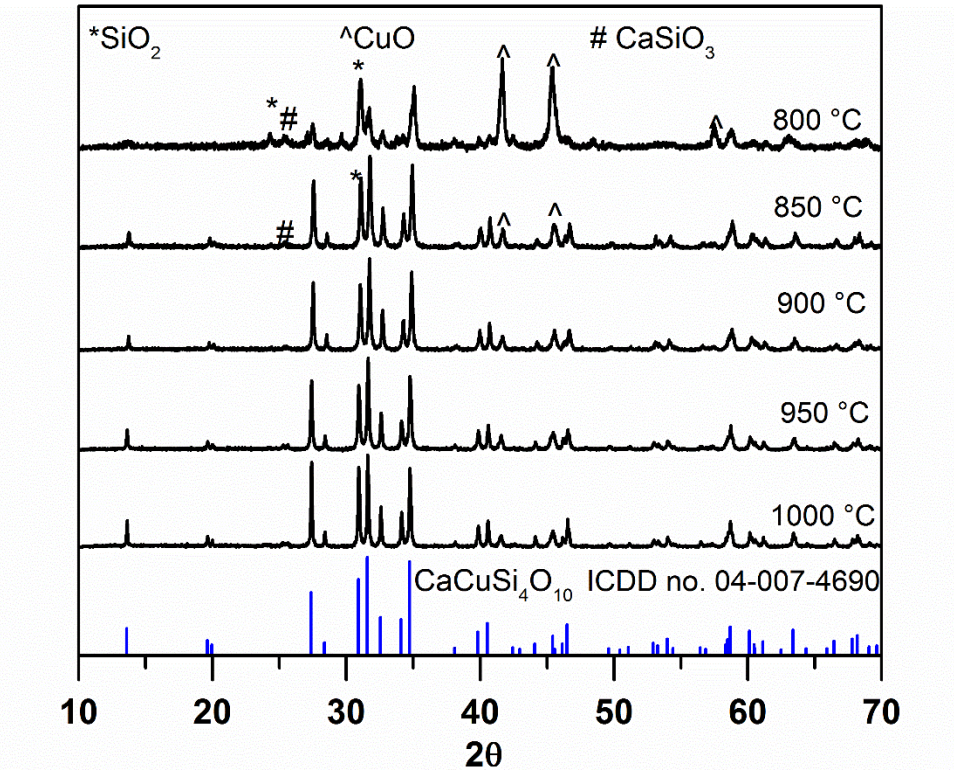

Figure 2.14. PXRD of $CaCuSi_4O_{10}$ solid state reactions using pelletized nano precursors with CaO nanoparticles reacted from 800-1000 °C.

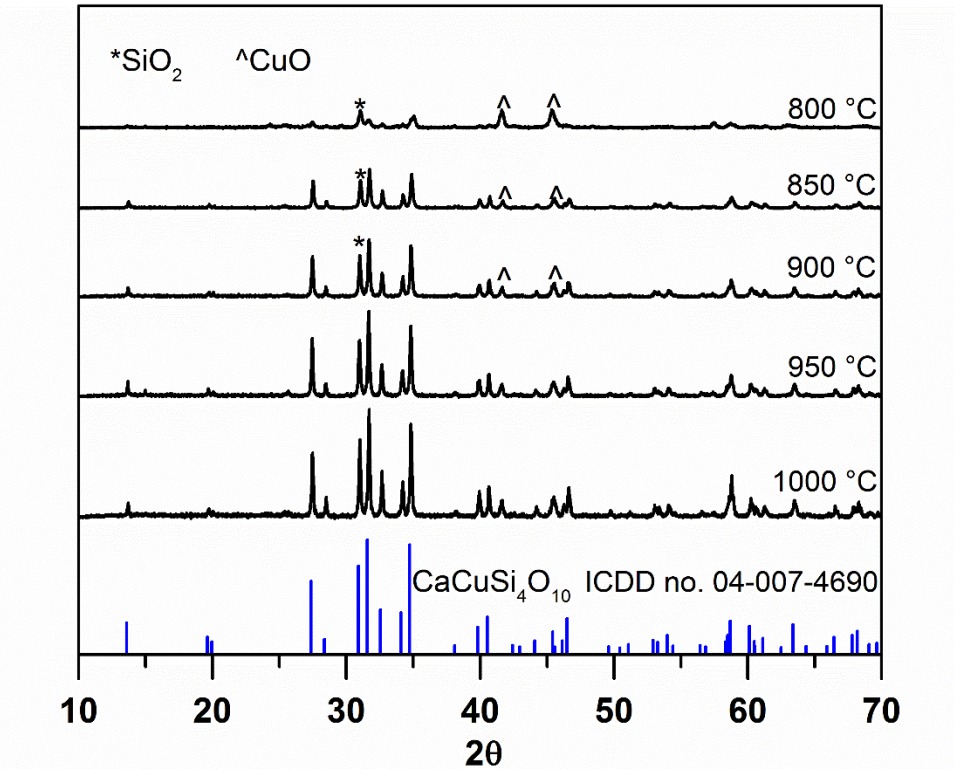

Figure 2.15. PXRD of $CaCuSi_4O_{10}$ solid state reactions using pelletized nano precursors with CaO nanoparticles reacted from 800-1000 °C after acid treatment.

Overall, we were successful at using nanoscale precursors to synthesize $CaCuSi_4O_{10}$ and we managed to lower the reaction temperature from 1050 °C to 850 °C. Pressing the precursors into pellets increased reactivity further and shifted the reaction to still lower temperatures. While the nanoparticles of CaO exhibited a decreased reactivity when compared to a fresh oxide, using all nanoscale reactants did produce more vivid blues at higher temperatures and crystals with more uniform grain size. And while this method does not provide a route to single crystals or produce free standing sub-micron crystals with a consistent size and morphology, it did produce porous networks of crystals with uniform grain size which could be useful for catalytic studies.

$SrCuSi_4O_{10}$ reacts at a lower temperature than $CaCuSi_4O_{10}$ with bulk precursors, so we would expect that this would continue to hold true with nanoscale precursors as well.

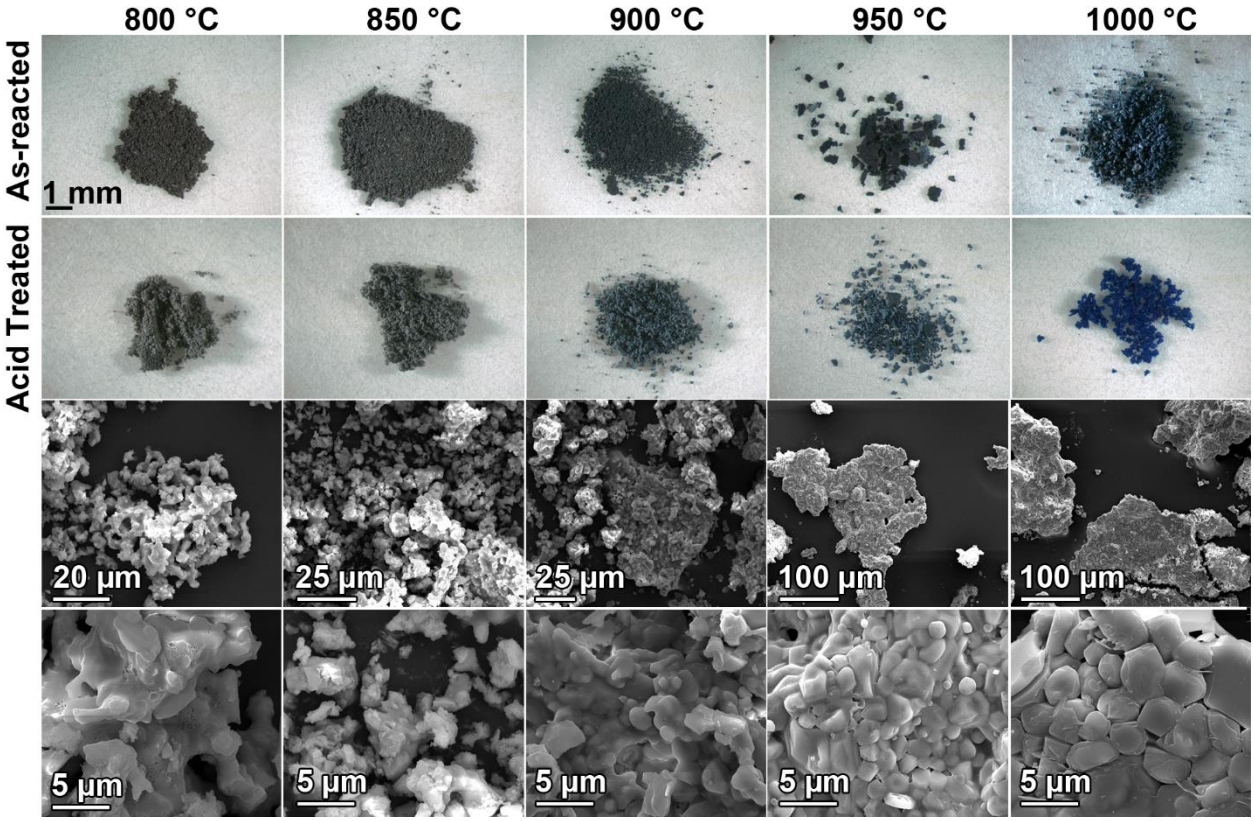

Figure 2.16. Top two rows show optical images of the as-reacted and acid treated products of $SrCuSi_4O_{10}$ solid state reactions using nano precursors reacted from 800-1000 °C. Bottom two rows show SEM images of the products after acid treatment.

For consistency and comparability, we also carried out a temperature study from 800-1000 ˚C (Figure 2.16). From 800-900 ˚C, initially there appeared to be little change from the $CaCuSi_4O_{10}$ reactions: the resulting powders were a black color, which changed to gray after acid treatment. This time, however, by PXRD (Figure 2.17), all the products were $SrCuSi_4O_{10}$, with a small $SrSiO_3$ impurity that was removed by acid treatment (Figure 2.18). SEM showed that the products were comprised of crystals of varying sizes. Starting at 900 °C, the blue color of the products became increasingly vivid, and as expected, SEM showed that the products were comprised of larger crystals than the ones formed in the lower temperature reactions (Figure 2.16). However, they were not smooth single crystals, but instead were smaller crystals that were sintered together. The smaller crystals had a rectangular shape and were ~ 1 µm in size at 950

°C, and were slightly larger at 1000 °C. We expected that $SrCuSi_4O_{10}$ would react at lower temperatures than $CaCuSi_4O_{10,}$ however the morphology of the resulting crystals was unexpected. To further pinpoint the temperature of formation, we extended the temperature study: $SrCuSi_4O_{10}$ forms at temperatures as low as 700 °C; at 650 °C, there is no formation of $SrCuSi_4O_{10}$, instead there is a mixture of $SrSi_2O_4$, and CuO.

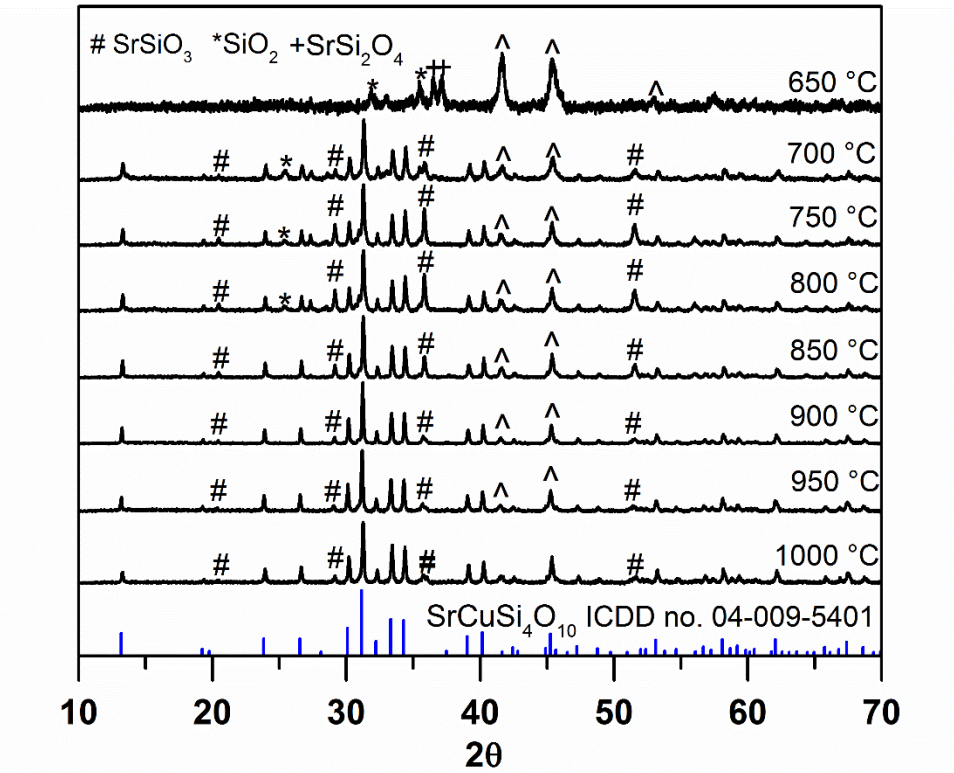

Figure 2.17. PXRD patterns of $SrCuSi_4O_{10}$ solid state reactions using nano precursors reacted from 650-1000 °C with $SrCuSi_4O_{10}$ reference pattern.

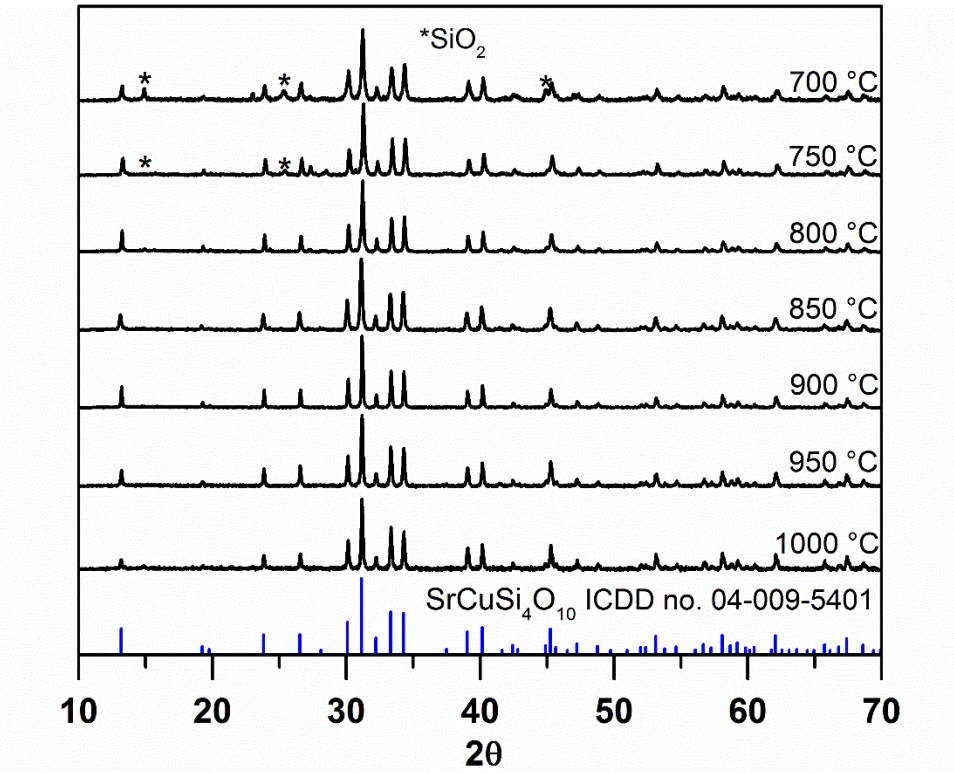

Figure 2.18. PXRD patterns of $SrCuSi_4O_{10}$ solid state reactions using nano precursors reacted from 700-1000 °C after acid treatment with $SrCuSi_4O_{10}$ reference pattern.

We again performed thermogravimetric analysis (TGA), this time on the nanoscale and bulk $SrCO_3$-CuO-SiO_2 mixture, to shed more light on the formation of our product using nano precursors (Figure 2.19).

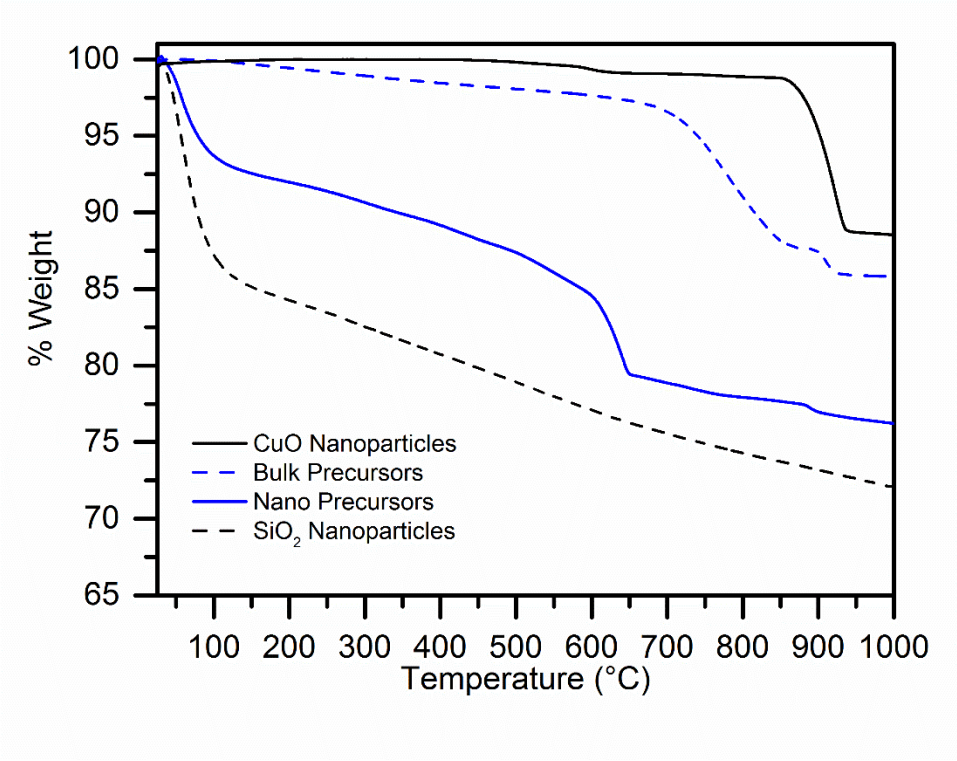

Figure 2.19. TGA curves of bulk and nanoscale $SrCuSi_4O_{10}$ reaction precursors and SiO_2 and CuO nanoparticles heated in air from 25-1000 ˚C at 5 ˚C/min.

Examining the reaction in air from 25-1000 °C at the same heating rate of 5 °C/min, we saw the following: (1) that below 150 °C there was a relatively large weight loss of ~7 %, most likely caused by the loss of residual water to absorption by the nanoscale SiO_2, similar to what was previously observed in the $CaCuSi_4O_{10}$ reactions; (2) that the greatest amount of decomposition occurred between 400-650 °C, a loss of ~15 % corresponding to the decomposition of $SrCO_3$ into SrO and CO_2, although it should be noted that this decomposition was more gradual in $SrCO_3$ than in $CaCO_3$); and (3) we confirmed that thermal stability of $SrCuSi_4O_{10}$ was greater than that of $CaCuSi_4O_{10}$ because it did not decompose before 1000 °C.[8]

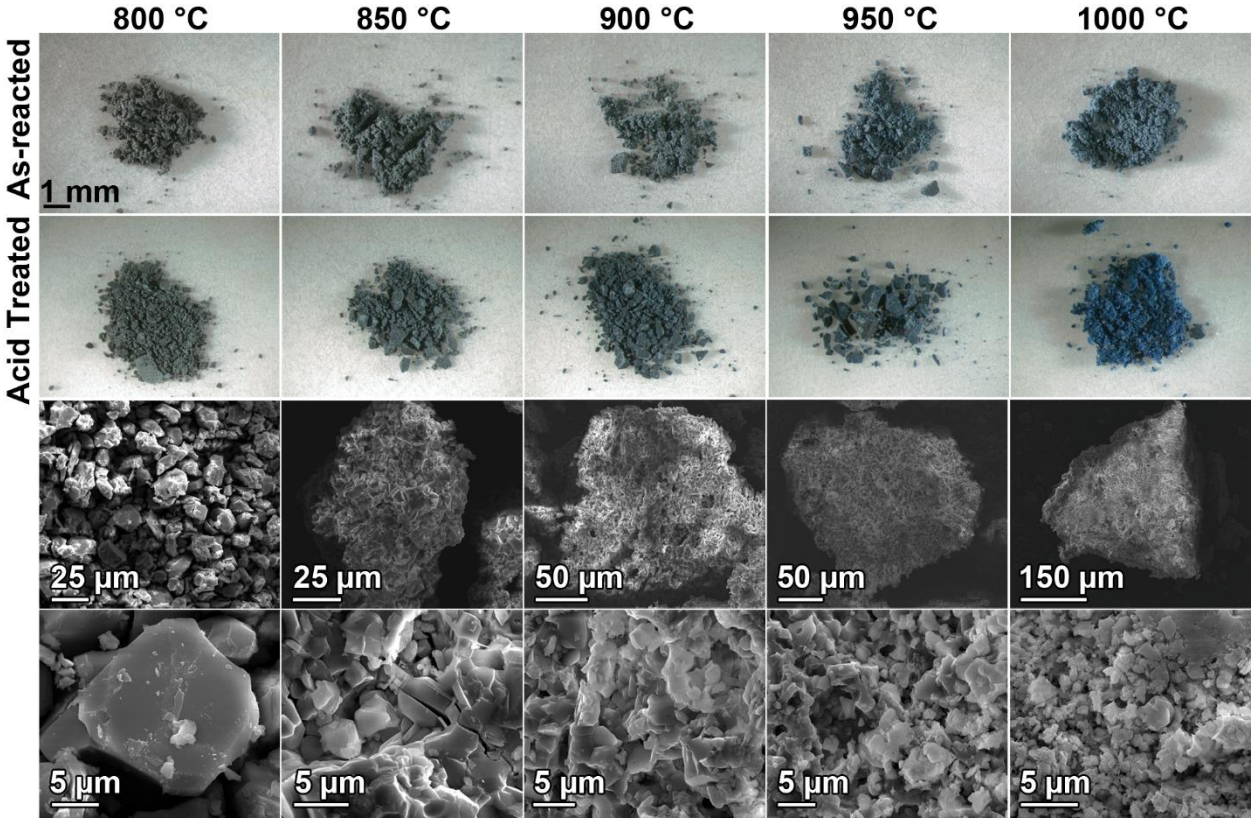

Figure 2.20. Top two rows show optical images of the as-reacted and acid treated products of $SrCuSi_4O_{10}$ solid state reactions using pelletized nano precursors reacted from 800-1000 °C. Bottom two rows show SEM images of the products after acid treatment.

After pressing the nanopowders into pellets, we again carried out a temperature study from 800-1000 ˚C (Figure 2.20). The majority of the products were a blue-gray color, only changing to a darker blue at 1000 ˚C after acid treatment. By PXRD, all the products were $SrCuSi_4O_{10}$ with a slight $SrSiO_3$ impurity that was removed after acid treatment (Figures 2.21 and 2.22). Examining the morphology by SEM, we saw that at 800 ˚C there were crystals that were approximately 10-25 µm in size, that were then fused into larger crystals at higher temperatures. Again, we extended the temperature study and we obtained very similar results: $SrCuSi_4O_{10}$ formed at temperatures as low as 700 ˚C; at 650 ˚C, there was no formation of $SrCuSi_4O_{10}$, instead there was a mixture of $SrSi_2O_4$, $SrSiO_3$, and CuO. Unlike what we observed in $CaCuSi_4O_{10}$ reactions, it did not appear that pelletizing the nanopowders provided any major

advantage for the synthesis of $SrCuSi_4O_{10}$ over the temperature range of 800-1000 °C in terms of reaction temperature and morphology. This is probably due to (1) the increased reactivity of the $SrCO_3$ when compared to $CaCO_3$; and (2) to the fact that, because the Sr:Cu:Si:O system does not form other strontium copper silicates polymorphs, such as $SrCuSi_2O_6$ or $SrCuSi_2O_7$, there were no competing kinetically favored products. Therefore, $SrCuSi_4O_{10}$ was free to form at lower temperatures.

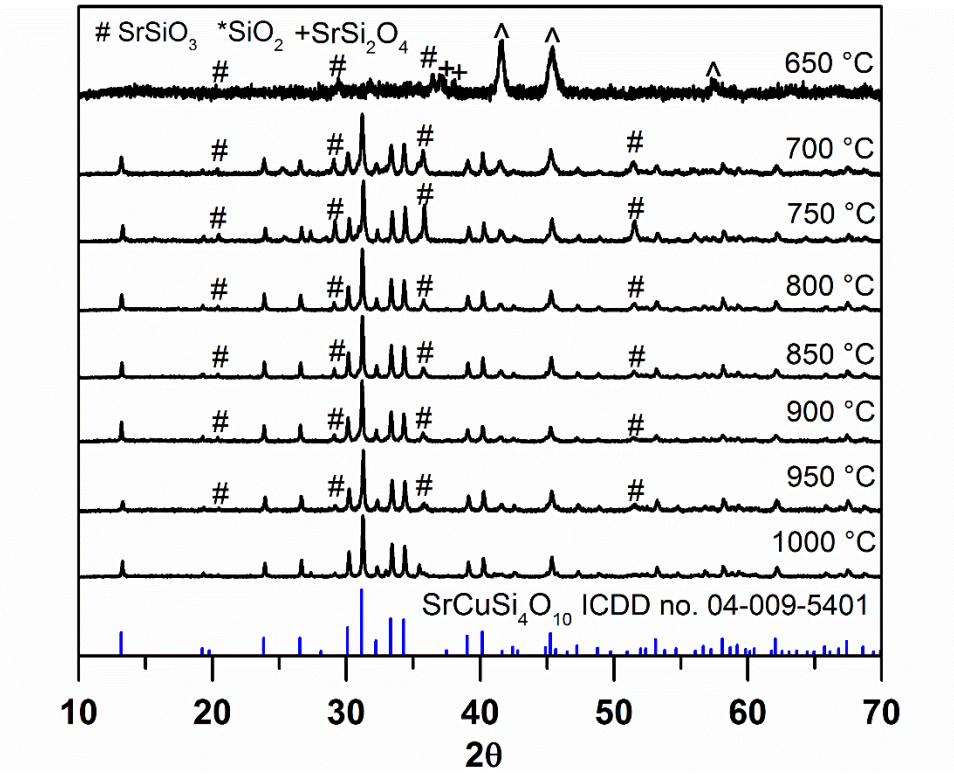

Figure 2.21. PXRD patterns of $SrCuSi_4O_{10}$ solid state reactions using nano precursors pressed into pellets and reacted from 700-1000 °C with $SrCuSi_4O_{10}$ reference pattern.

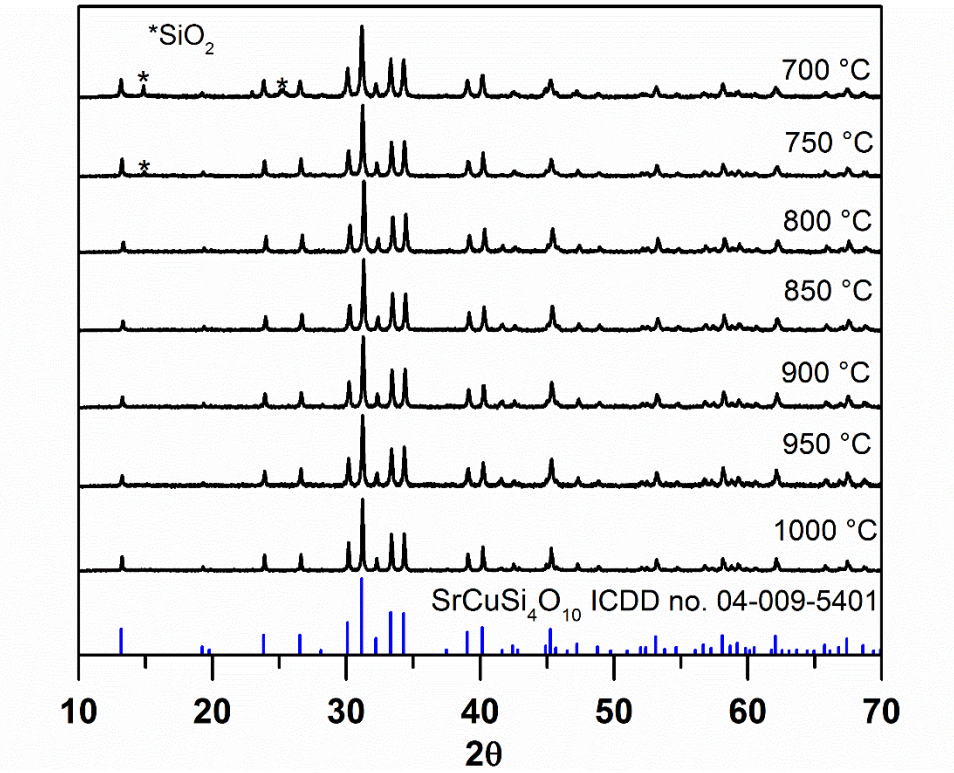

Figure 2.22. PXRD patterns of $SrCuSi_4O_{10}$ solid state reactions using nano precursors pressed into pellets and reacted from 800-1000 °C after acid treatment with $SrCuSi_4O_{10}$ reference pattern.

Of all the members of the $ACuSi_4O_{10}$ series, $BaCuSi_4O_{10}$ should react the most readily. For consistency, we again carried out a temperature study from 800-1000 °C. However, all the resulting products appeared to be various shades of purple (Figure 2.23 top row), rather than the expected blue.

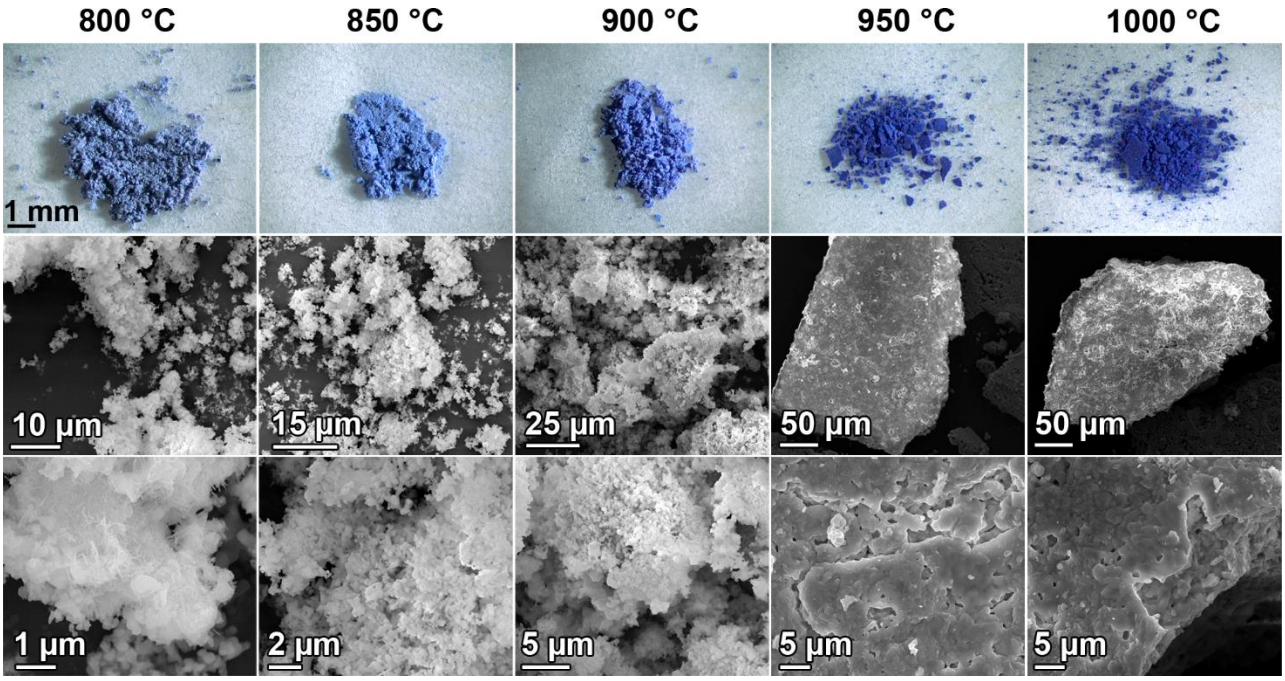

Figure 2.23. Optical and SEM images of $BaCuSi_4O_{10}$ solid state reactions using nano precursors reacted from 800-1000 °C.

After further examination of the products at higher magnifications, it became clear that the products were actually a mixture of both blue and purple (Figure 2.24).

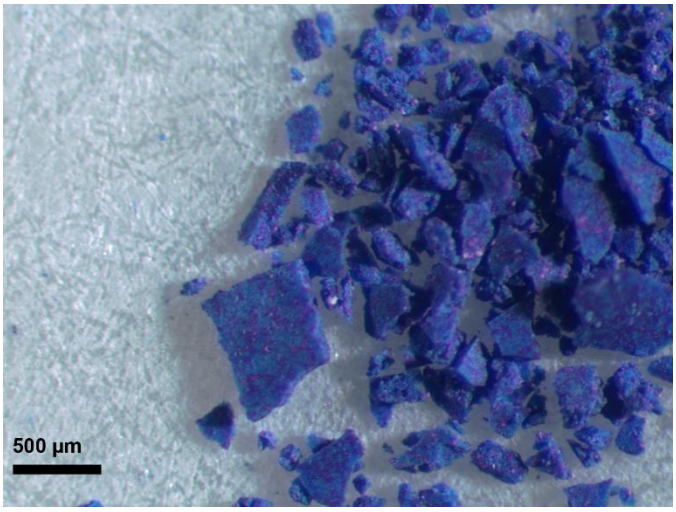

Figure 2.24. Optical image at higher magnification of the product formed from the $BaCuSi_4O_{10}$ reaction at 1000 °C.

The presence of these purple shades indicated that $BaCuSi_2O_6$ was forming as a mixed product with $BaCuSi_4O_{10}$. Previous work has indicated that $BaCuSi_2O_6$ forms as the primary product at lower temperatures, even when using a 1:4:1 ratio of barium to silicon to copper.[10] Here, perhaps due to the increased reactivity of the nanoscale reactants, the formation of $BaCuSi_2O_6$ was even more favored. At lower temperatures, another Ba:Cu:Si:O product, $BaCuSi_2O_7$, formed as well. Again, this result is consistent with previous work.[10] As the reaction temperature decreased, a higher percentage of $BaCuSi_2O_6$ was formed until 750 °C where, per diffraction analysis, the product was almost completely $BaCuSi_2O_6$ (Figure 2.25).

Examining the products with optical microscopy, $BaCuSi_2O_6$ was formed in discrete pockets (Figure 2.24). However, by SEM, there was no obvious difference between $BaCuSi_2O_6$ and $BaCuSi_4O_{10}$ (Figure 2.23). At higher temperatures, 900-1000 °C, the particles appeared fused together into larger pieces. Unlike what we had observed for the lighter members of the $ACuSi_4O_{10}$ series, there was no gray color present in the $BaCuSi_4O_{10}$ reactions. Because $BaCO_3$ is more reactive than the other alkali carbonates, perhaps all the CuO was being reacted due to the $BaCuSi_2O_6$ having a lower energy of formation which would account for the above color difference.

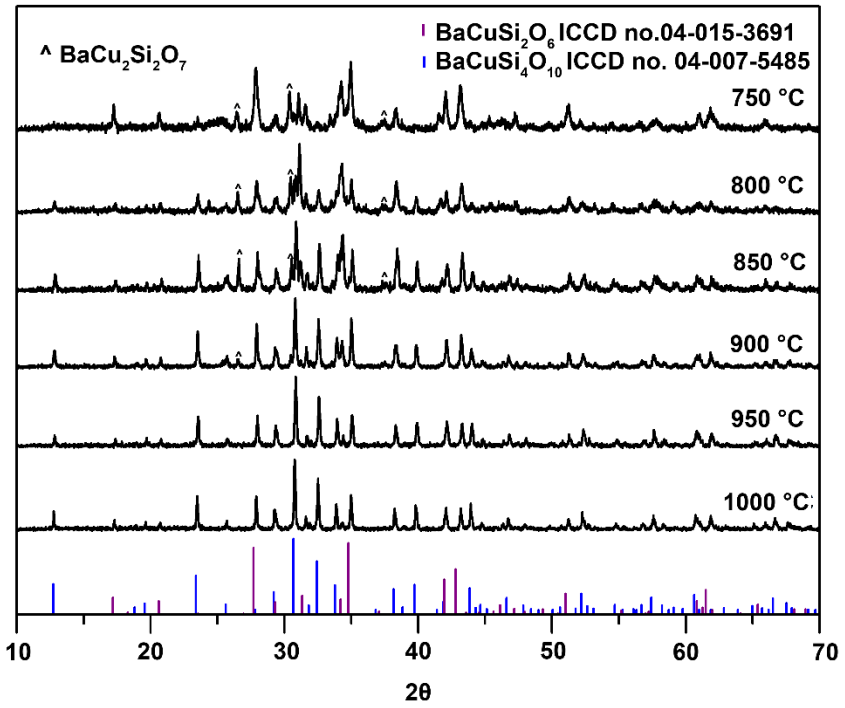

Figure 2.25. PXRD patterns of $BaCuSi_4O_{10}$ solid state reactions using nano precursors reacted from 750-1000 °C before acid treatment with $BaCuSi_2O_6$ and $BaCuSi_4O_{10}$ reference patterns.

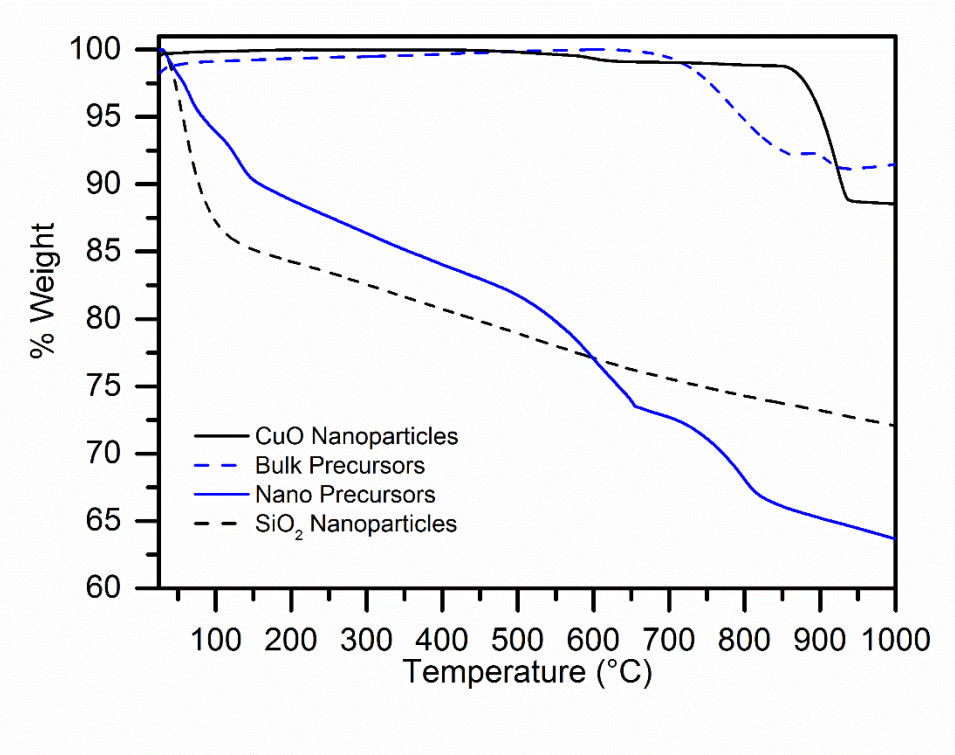

Figure 2.26. TGA curves of bulk and nanoscale $BaCuSi_4O_{10}$ reaction precursors and SiO_2 and CuO nanoparticles heated in air from 25-1000 °C at 5 °C/min.

Thermogravimetric analysis (TGA) of the formation of $BaCuSi_4O_{10}$ using the nanoscale precursors (Figure 2.26) provided more information about how the reaction was proceeding. Analyzing the reaction in air from 25-1000 °C at the same heating rate of 5 °C/min, we saw that below 150 °C there was a relatively large weight loss of ~10 %. Again, this loss was most likely caused by the due to the absorption of residual water by SiO_2. The major decomposition occurred between 400-650 °C, a weight loss of ~12 % that corresponded to the decomposition of $BaCO_3$ into BaO and CO_2, this loss was similar to what was previously observed for $CaCO_3$ and $SrCO_3$. The most unexpected feature was a loss of 6.8% from 650-835 °C, which is greater than what was observed for the bulk precursors. Again, we saw evidence of $BaCuSi_4O_{10}$'s greater thermal stability because it still hadn't decomposed by 1000 °C.[8]

Unlike $BaCuSi_4O_{10}$, $BaCuSi_2O_6$ rapidly decomposes in acid.[10-11] Therefore, it was easily removed with a solution of 1 M HNO_3 while leaving the $BaCuSi_4O_{10}$ product intact. After the acid treatment, all the products were blue (Figure 2.27 top row). The places where $BaCuSi_2O_6$ has been present was now clearly visible as holes in the 950-1000 °C samples (Figure 2.27 bottom two rows). The morphology of the other samples appeared unchanged.

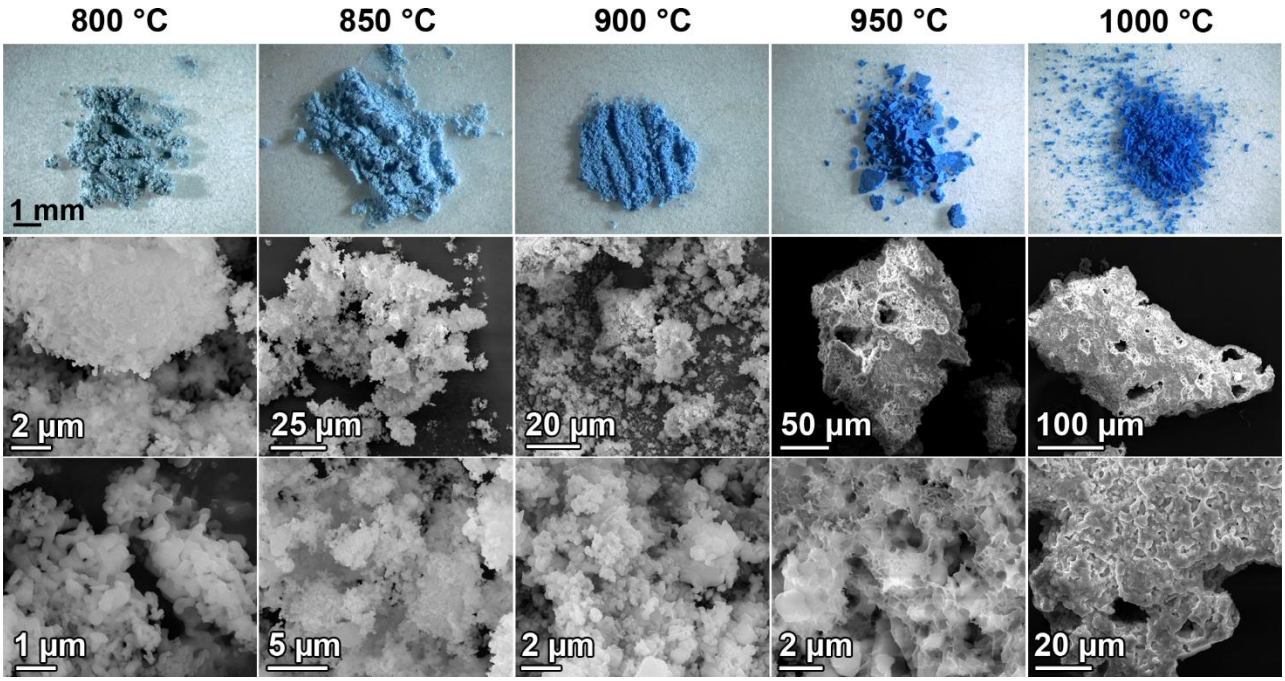

Figure 2.27. Optical and SEM images of $BaCuSi_4O_{10}$ solid state reactions using nano precursors reacted from 800-1000 °C after acid treatment.

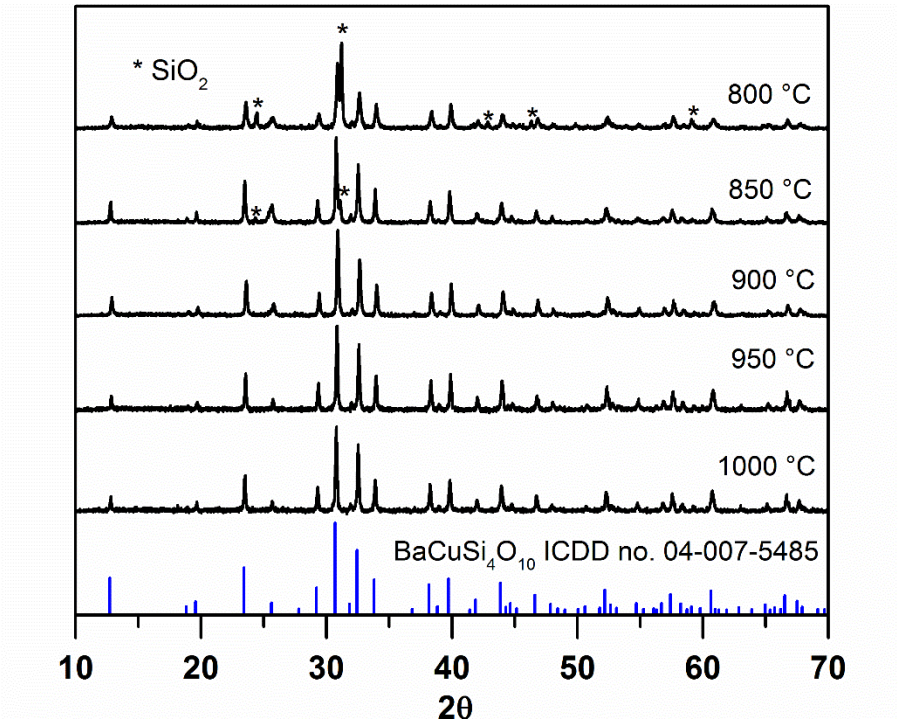

Figure 2.28. PXRD patterns of $BaCuSi_4O_{10}$ solid state reactions using nano precursors reacted from 800-1000 °C after acid treatment with $BaCuSi_4O_{10}$ reference pattern.

PXRD analysis showed that $BaCuSi_4O_{10}$ was the sole barium copper silicate present in our product, though there was a slight silica impurity starting at 850 °C (Figure 2.28). This impurity was probably simply the remains of the earlier barium copper silicates following acid treatment. On the whole, the reaction temperatures required for formation of $BaCuSi_4O_{10}$ were much lower than for the bulk material. However, the formation of the mixed product was not a particularly advantageous result, and even though $BaCuSi_2O_6$ can be readily removed with acid, the remaining products were still slightly contaminated with SiO_2. Given the above, we were particularly interested in seeing if our use of pelletized nanopowders could improve on these results.

After pressing the nanopowders into pellets, we again carried out a temperature study from 800-1000 °C (Figure 2.29). However, unlike the previous reactions with loose powders, this time all the reaction products were blue because pressing the reactants into pellets prevented the formation of $BaCuSi_2O_6$ over the temperature range initially investigated. Pelletizing the nanopowders increased reactivity sufficiently to not only lower the initial temperature of formation significantly**,** but also prevent the formation of $BaCuSi_2O_6$ over the temperature range of 800-1000 °C.

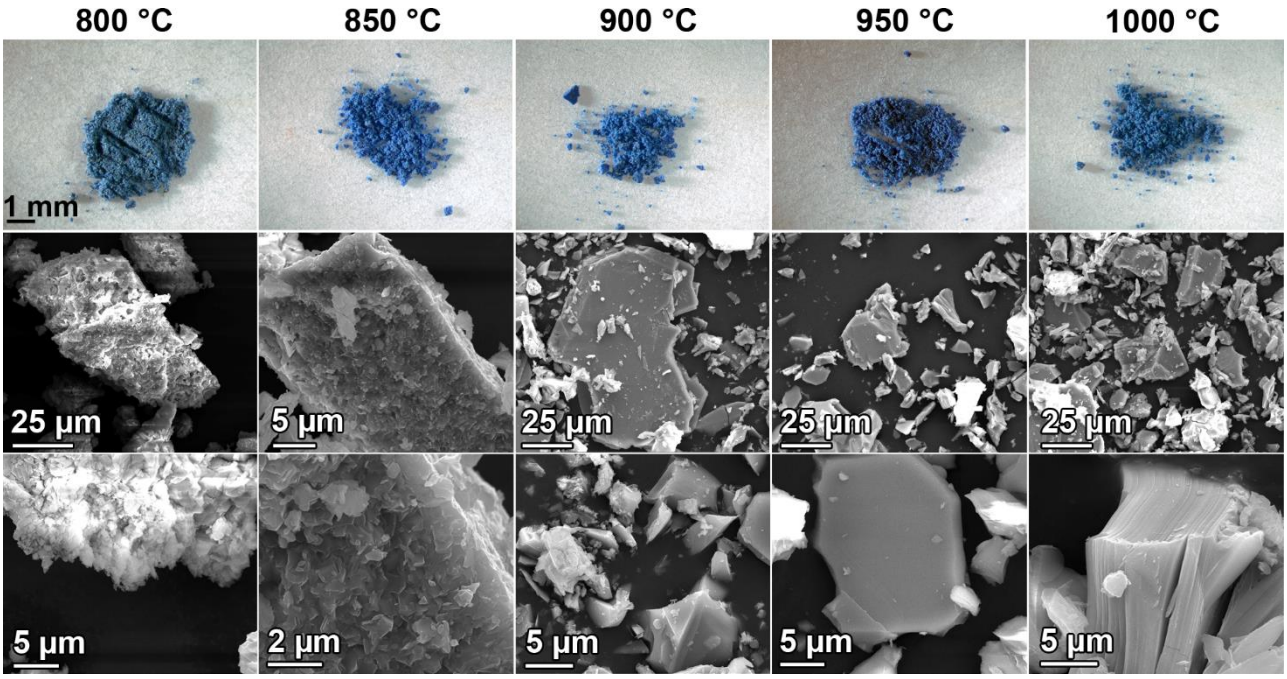

Figure 2.29. Optical and SEM images of $BaCuSi_4O_{10}$ solid state reactions using pelletized nano precursors reacted from 800-1000 °C.

From 800-850 ˚C, the products comprised microcrystals sintered together. At temperatures above 900 ˚C, the crystals formed were smooth single crystals.

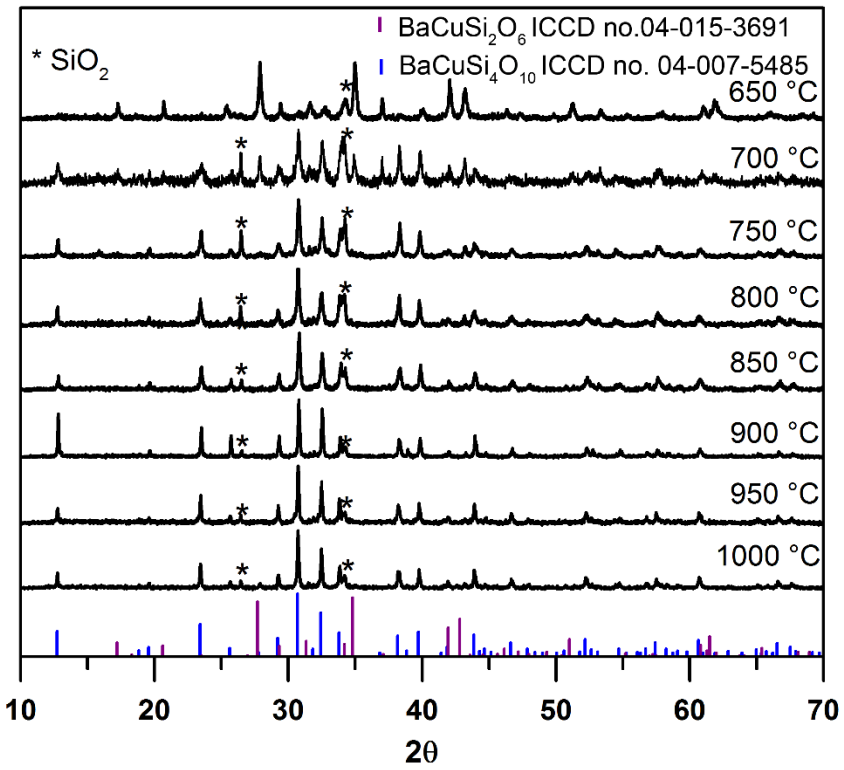

Figure 2.30. PXRD patterns of $BaCuSi_4O_{10}$ solid state reactions using nano precursors pressed into pellets and reacted from 650-1000 °C.

Analyzing the products by PXRD confirmed that the crystals were $BaCuSi_4O_{10}$ with a SiO_2 impurity and that there was no formation of $BaCuSi_2O_6$ from 800-1000 °C (Figure 2.30). We continued the temperature study at even lower temperatures to further pinpoint the initial formation temperature for $BaCuSi_4O_{10}$ using pelletized nanoscale precursors (Figure 2.30). From the data, the initial formation temperature for $BaCuSi_4O_{10}$ was around 700 °C. However, $BaCuSi_2O_6$ started forming as a mixed phase with $BaCuSi_4O_{10}$ below 750 C° and only $BaCuSi_2O_6$ was present below 700 °C.

After acid treatment the morphology of the products remained mostly unchanged (Figure 2.31). The crystals formed at 800-850 °C were still micron size sintered into chunks, and those formed at 900-1000 °C were still smooth and much larger. There was a slight difference after

acid treatment, in that it was now much more obvious that the $BaCuSi_4O_{10}$ formed at 850 °C was in the form of sub-micron size single crystals (Figure 2.32).

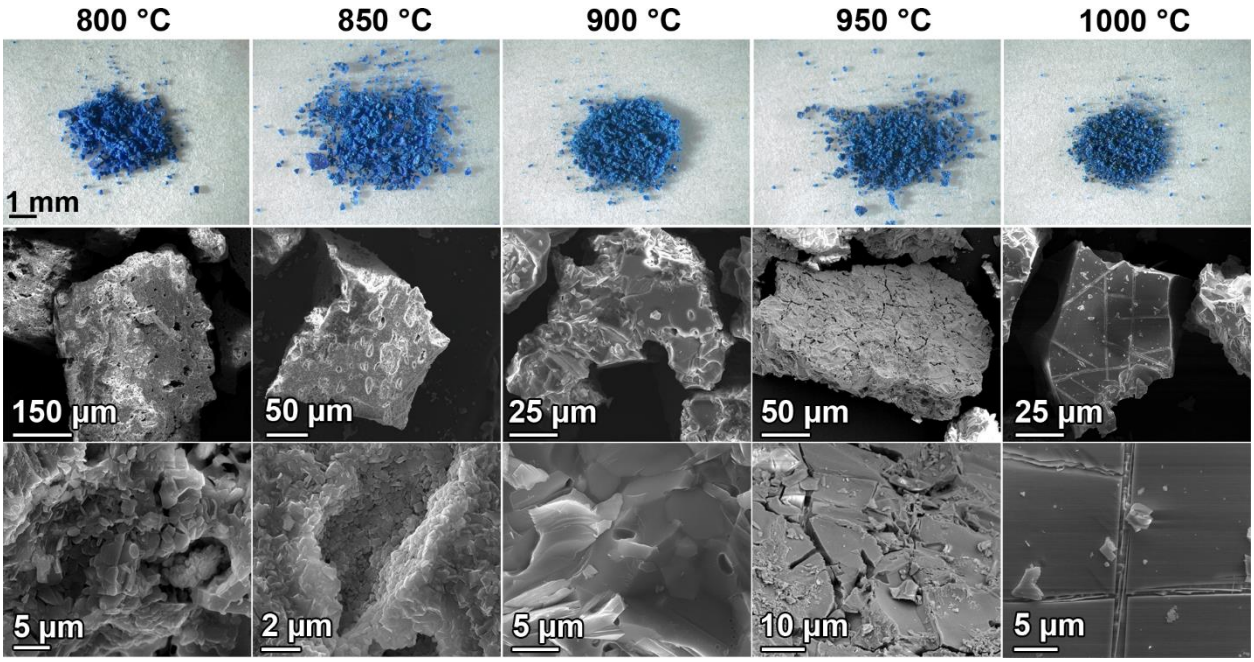

Figure 2.31. Optical and SEM images of $BaCuSi_4O_{10}$ solid state reactions using pelletized nano precursors reacted from 800-1000 °C after acid treatment.

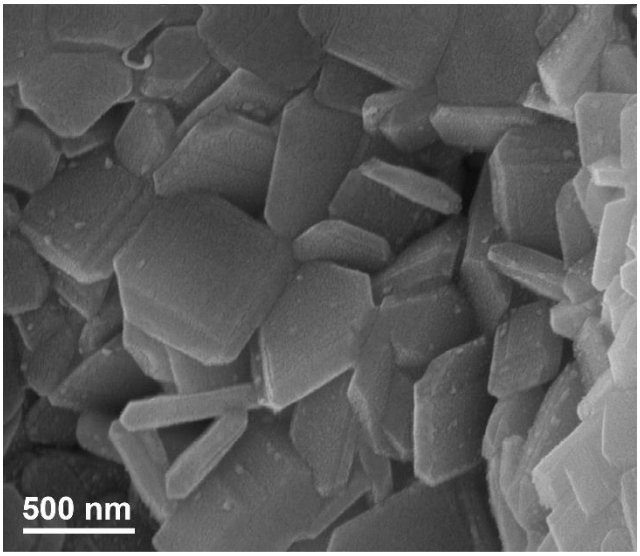

Figure 2.32. SEM image showing the microcrystalline morphology of $BaCuSi_4O_{10}$ synthesized at 850 °C after acid treatment.

The reaction at 850 °C produced sub-micron sized crystals with a morphology consistent with the ideal shape for the $ACuSi_4O_{10}$ series according to the rules of Donnay and Harker[12] and

are consistent with Pabst's results[6a], only without the presence of a fluxing agent. The crystals were around 700 nm and ~130 nm in thickness (Figure 2.32.), which are considerably smaller than the 0.1x 0.03 mm crystals produced using Pabst's method.

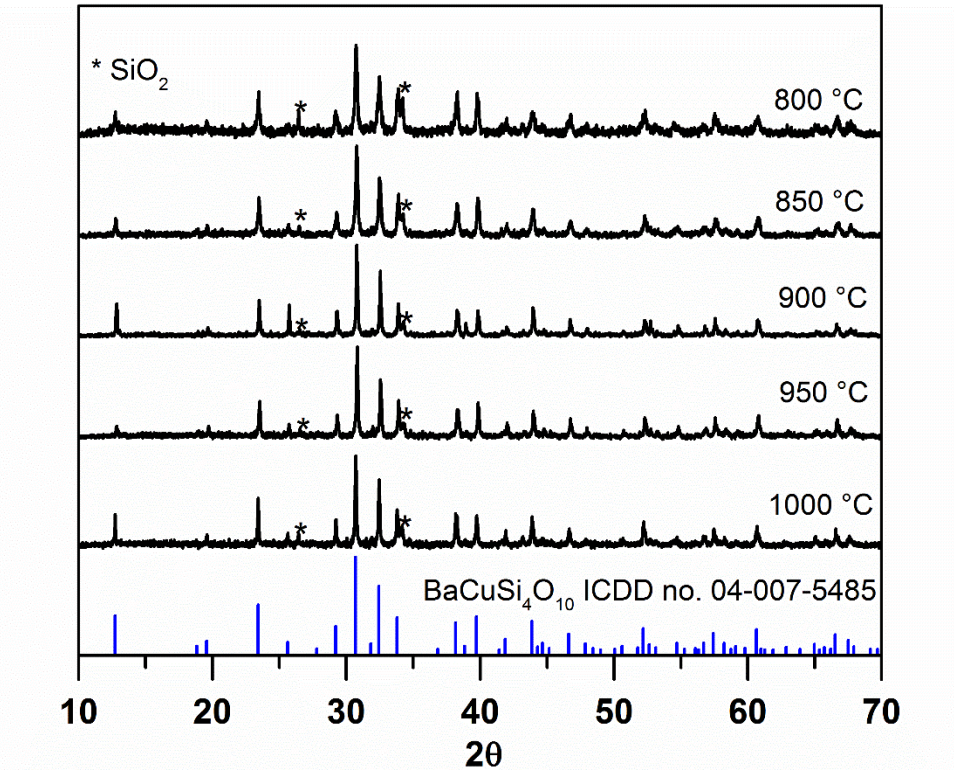

Figure 2.33. PXRD patterns of $BaCuSi_4O_{10}$ solid state reactions using nano precursors pressed into pellets and reacted from 800-1000 °C after acid treatment.

Overall, the use of nanoscale reactants for the synthesis of $BaCuSi_4O_{10}$ proved quite successful. While the loose powders produced a mixture of $BaCuSi_2O_6$ and $BaCuSi_4O_{10}$, the unwanted $BaCuSi_2O_6$ was easily removed with a simple acid treatment. Furthermore, by pelletizing the nanopowders, we were able to form single crystals of $BaCuSi_4O_{10}$ of varying sizes.

Conclusion

Using nanoscale precursors lowered the solid state reaction temperature for the $ACuSi_4O_{10}$ series by ~200 ˚C. We found that pressing the powdered nanoscale reactants into pellets was the most effective method for enhancing the reactivity of the $ACuSi_4O_{10}$ series. $SrCuSi_4O_{10}$ was the most reactive of all the series, which was in contrast to previous results which indicate that $BaCuSi_4O_{10}$ should react the most readily. However, due to the presence of more kinetically favored products in the $BaO:CuO:SiO_2$ system, and the lack thereof in the $SrO:CuO:SiO_2$ system, the results were not that surprising. The morphology of the products was typically sub-micron crystals sintered into larger crystals. However, in the case of $CaCuSi_4O_{10}$, changing our precursors to nanoparticles of CaO enabled us to form crystals with more uniform size and shape, indicating that the initial reactant morphology did have an influence on the final product shape.

For $SrCuSi_4O_{10}$, the best results came from the loose powders at a temperature range from 900-1000 ˚C and were crystals with uniform size and shape sintered together. The novel porous networks of $CaCuSi_4O_{10}$ and $SrCuSi_4O_{10}$ crystals that may have potential for use in catalytic reactions.

$BaCuSi_4O_{10}$, when reacted in loose powders formed as a mixture of $BaCuSi_2O_6$ and $BaCuSi_4O_{10}$, but by pressing the nanopowders into pellets, we were able to increase the reactivity sufficiently to prevent the formation of $BaCuSi_2O_6$ as well as to form single crystals of $BaCuSi_4O_{10}$ of varying sizes. The best results were the uniform sub-micron single crystals formed at 850 ˚C. In sum, our results here represent a positive achievement: by using nanoscale

precursors in solid state synthesis we have provided another route to size and morphology control over the $ACuSi_4O_{10}$ series.

References

1. Bastus, N. G.; Casals, E.; Vazquez-Campos, S.; Puntes, V., *Nanotoxicology* **2008,** *2*, 99-112.
2. (a) *Nanomaterials: Synthesis, Properties and Applications*. Second ed.; Taylor & Francis Group: 1996; (b) Aleksandr Ivanovich Gusev, A. A., *Nanocrystalline Materials* Cambridge Int Science Publishing: 2004; (c) Chen, Y.; Li, C. P.; Chen, H.; Chen, Y., *Sci. Technol. Adv. Mater.* **2006,** *7*, 839-846; (d) Bodaghi, M.; Mirhabibi, A.; Tahriri, M., *Powder Metall. Met. Ceram.* **2009,** *48*, 634-640.
3. Buscaglia, M. T.; Bassoli, M.; Buscaglia, V.; Vormberg, R., *J. Am. Ceram. Soc.* **2008,** *91*, 2862-2869.
4. Jiao, S.; Kilby, K. T.; Zhang, L.; Fray, D. J., *Nanotechnology* **2009,** *20*, 085606.
5. (a) Akyildiz, H., *Ceram. Int.* **2015,** *41*, 14108-14115; (b) Wu, K.; Hu, G.; Du, K.; Peng, Z.; Cao, Y., *Mater. Lett.* **2015,** *152*, 217-219.
6. (a) Pabst, A., *Acta Crystallogr.* **1959,** *12*, 733-9; (b) Tite, M. S.; Bimson, M.; Cowell, M. R., *Adv. Chem. Ser.* **1984,** *205*, 215-42; (c) Chakoumakos, B. C.; Fernandez-Baca, J. A.; Boatner, L. A., *J. Solid State Chem.* **1993,** *103*, 105-113; (d) Berke, H.; Wiedemann, H. G., *East Asia Sci. Technol. Med.*, **2000**, *17*, 94-120.; (e) Mazzocchin, G. A.; Rudello, D.; Bragato, C.; Agnoli, F., *J. Cult. Herit.* **2004,** *5*, 129-133; (f) Pradell, T.; Salvado, N.; Hatton, G. D.; Tite, M. S., *J. Am. Ceram. Soc.* **2006,** *89*, 1426-1431.
7. (a) Eastaugh, N. W., V.; Chaplin, T.; Siddall, R., *The Pigment Compendium: A Dictionary of Historical Pigments*. **2005**, Butterworth-Heinemann: Oxford, U.K. (b) Riederer, J., Egyptian Blue. In *Artists' Pigments: A Handbook of Their History and Characteristics*, FitzHugh, E. W., Ed. **1997**.

8. Wiedemann, H. G; Bayer, G., *Chem. Tech.* **1977,** *7*, 381-389.

9. West, A. R., *Solid State Chemistry and Its Applications*. **1987**, John Wiley & Sons.

10. Wiedemann, H. G.; Bayer, G., *Formation and stability of Chinese barium copper-silicate pigments*. **1996**, Getty Conservation Inst: Los Angeles, 379-387.

11. FitzHugh, E. W.; Zycherman, L. A., *Stud. Conserv.* **1992,** *37*, 145-54.

12. Harker, J. D. H. D. a. D., *Am. Mineral.* **1937,** *22*, 446-467.

CHAPTER 3

HYDROTHERMAL FORMATION OF CALCIUM COPPER TETRASILICATE

Darrah Johnson-McDaniel, Sara Comer, Joseph Kolis, and Tina T. Salguero. *Chemistry: A European Journal*. **2015**, *49*, 17560–17564. Reproduced with permission from Wiley-VCH.

Abstract

We describe the first hydrothermal synthesis of $CaCuSi_4O_{10}$ as micron-scale clusters of thin platelets, distinct from morphologies generated under salt-flux or solid-state conditions. The hydrothermal reaction conditions are surprisingly specific: too cold, and instead of $CaCuSi_4O_{10}$, a porous calcium copper silicate forms; too hot, and calcium silicate ($CaSiO_3$) forms. The precursors also strongly impact the course of the reaction, with the most common side product being sodium copper silicate ($Na_2CuSi_4O_{10}$). Optimized conditions for hydrothermal $CaCuSi_4O_{10}$ formation from calcium chloride, copper(II) nitrate, sodium silicate, and ammonium hydroxide are 350 °C at 3000 psi for 72 h; at longer reaction times, competitive delamination and exfoliation causes crystal fragmentation. These results illustrate that $CaCuSi_4O_{10}$ is an even more unique material than previously appreciated.

Introduction

Calcium copper tetrasilicate ($CaCuSi_4O_{10}$) holds a special place in the history of chemistry as the first synthetic inorganic material produced on large scale.[1,2] During the past five millennia, it has been used extensively as a blue pigment (Egyptian blue), and recent research has focused on its remarkable near infrared luminescence properties.[3] In addition to archaeological imaging,[4] these investigations have included using Yb^{3+} doping to increase near infrared emission,[5] evaluating $CaCuSi_4O_{10}$ as the active material in optical sensors,[6] measuring the effects of temperature on photoluminescence,[7] detailing the electronic structure of the blue chromophore,[8] and utilizing the upconversion capability of $CaCuSi_4O_{10}$ under laser excitation to produce bright broadband light.[9] Traditionally $CaCuSi_4O_{10}$ has been prepared by salt-flux routes;[10] the necessary reaction temperature (ca. 875 °C) was accessible even in antiquity using wood-fired ovens.[11] Solid state synthesis also can be used to produce $CaCuSi_4O_{10}$ but requires higher temperatures (>1000 °C).[12] Neither method provides control over product morphology or size, however, which is an important consideration for modern applications like imaging and sensing technologies.

We are interested in synthesizing $CaCuSi_4O_{10}$ using a hydrothermal process because this method typically has the advantages of producing homogeneous and well-crystallized materials under relatively mild temperatures and pressures.[13] Notably, $CaCuSi_4O_{10}$ occurs as a rare mineral, cuprorivaite, at locations in Italy (Mount Vesuvius), Germany (the Sattelberg volcanic cone, Eifel region), South Africa (Messina copper mines), and the United States (Klamath County, Oregon).[14] The geology of these sites suggests that cuprorivaite forms in a hydrothermal environment. Indeed, the heavier congeners of $CaCuSi_4O_{10}$, namely $SrCuSi_4O_{10}$ and $BaCuSi_4O_{10}$, can be synthesized from the alkali earth chlorides, copper(II) oxide, and sodium silicate in basic,

aqueous conditions at a modest temperature (250 °C).[15] The hydrothermal synthesis of $CaCuSi_4O_{10}$ has remained elusive, however. As stated by Warner in his monograph on important inorganic materials, "Success in this area would break the historic dependency on the use of a salt flux, and may provide an insight to the conditions under which cuprorivaite forms in nature."[2]

Experimental

General: $CaCl_2 \cdot 2H_2O$ (ACS reagent, ≥ 99% purity), sodium silicate solution [$Na_2O(SiO_2)_x(H_2O)_x$] (reagent grade purity, 26.5% SiO_2), NH_4OH (ACS reagent, 28–30% NH_3 basis), and 5M NaOH (ACS Reagent, ≥ 97.0%) were purchased from Sigma-Aldrich. $Cu(NO_3)_2 \cdot 2.5H_2O$ (certified ACS grade) was purchased from Fischer Scientific. $Ca(NO_3)_2 \cdot 4H_2O$ (certified ACS crystalline grade) was purchased from J. T. Baker.

Hydrothermal synthesis of $CaCuSi_4O_{10}$: $CaCl_2 \cdot 2H_2O$ (0.196 g, 1.33 mmol) and $Cu(NO_3)_2 \cdot 2.5H_2O$ (0.619 g, 2.66 mmol) or $CuCl_2 \cdot 2H_2O$ (0.227 g, 1.33 mmol) were dissolved in deionized water (30 mL). While monitoring the pH and stirring, sodium silicate solution [$Na_2O(SiO_2)_x(H_2O)_x$] (1.27 mL; 5.31 mmol of SiO_2) was added drop-wise to the solution. The final pH of the solution was then adjusted to 12 using 14.6M NH_4OH (28–30% NH_3 basis). Then a sample of the resulting gelatinous mixture (0.8 mL) was placed into a silver ampule, welded shut, placed in a high temperature autoclave (filled with deionized water to counter-pressure the ampules), and heated to 350 °C for 12–96 h. Once the reaction time was complete, the vessel was cooled to room temperature, the solid product was washed with water and collected by vacuum filtration. The isolated yield of blue crystals was 0.007 g (54%). Additional experiments to

examine varying reaction conditions were carried out in the same manner with $Ca(NO_3)_2 \cdot 4H_2O$ (0.314 g, 1.33 mmol), $CuCl_2 \cdot 2H_2O$ (0.227 g, 1.33 mmol), and 5M NaOH at 350 or 450 °C.

Hydrothermal synthesis of calcium copper silicate hydrate micro-dumbbells: $Ca(NO_3)_2 \cdot 4H_2O$ (0.314 g, 1.33 mmol) and $Cu(NO_3)_2 \cdot 2.5H_2O$ (0.619 g, 2.66 mmol) were dissolved in deionized water (30 mL). While monitoring the pH and stirring, sodium silicate solution $[Na_2O(SiO_2)_x(H_2O)_x]$ (1.27 mL; 5.31 mmol of SiO_2) was added drop-wise to the solution. The final pH of the solution was then adjusted to 12 using 14.6M NH_4OH (28–30% NH_3 basis). The resulting gelatinous mixture was placed into a 45 mL capacity Teflon-lined autoclave (Parr Instrument Co. acid digestion vessel) and heated at 250 °C for 96 h. The blue product (0.140 g) was isolated by decanting the gelatinous supernatant and washing the crystals with water. Additional experiments to examine varying reaction conditions were carried out in the same manner with $CaCl_2 \cdot 2H_2O$ (0.196 g, 1.33 mmol), $CuCl_2 \cdot 2H_2O$ (0.227 g, 1.33 mmol), and 5M NaOH at 250 °C.

Characterization: Product composition was confirmed using a Bruker D8-Advance powder X-ray diffractometer (CoKa radiation source) operated at 40 mA and 40 kV. PXRD patterns were recorded in the 2θ range of 10–70° with a scanning rate of 0.5 s per step. The morphology of products was examined by FEI Inspect F field emission gun scanning electron microscope (SEM) operated at 20 keV. The samples were prepared for SEM by sprinkling the powders on carbon sticky tape and then coating with gold. EDS data were collected with an EDAX Inc. instrument. Solid-state ^{29}Si magic angle spinning (MAS) nuclear magnetic resonance (NMR) spectra were collected using a Bruker AV3–400 solid-state NMR spectrometer with a 4 mm MAS BB HX probe. The sample was packed in a 4 mm ZrO_2 rotor with a spinning speed of 10 kHz. The experiment used direct polarization with 1H decoupling with a repetition delay of 10 s,

a pulse length of 2 ms (ca. 35 degree pulse length) and 6136 scans collected. For electron probe micro-analysis (EPMA), the micro-dumbbells were imbedded in resin, polished, and then carbon-coated. EPMA data were collected using a JEOL JXA 8600 Superprobe operated at 10 KeV.

Acknowledgements Work by T.T.S. and D.J.M. was supported by a U.S. Department of Energy (DOE), Office of Science, Basic Energy Sciences (BES) Early Career Research Program Award (#DE-SC0008065). J.W.K. and S.C. are indebted to the National Science Foundation #DMR-1410727. Many thanks to Dr. Chris Fleisher (UGA Geology) for his help with collecting the EPMA data, and to Dr. Johannes Leisen (Georgia Institute of Technology) for assistance with the NMR experiments.

Results and Discussion

We now report the conditions required for $CaCuSi_4O_{10}$ formation in a hydrothermal environment. The key to success is threefold: the copper source must be specifically copper(II) nitrate, the mineralizer is optimally ammonium hydroxide, and the reaction temperature/pressure should be about 350 °C/ 3000 psi. In the optimized procedure, an aqueous mixture of $CaCl_2 \cdot 2H_2O$, $Cu(NO_3)_2 \cdot 2.5H_2O$, and $[Na_2O(SiO_2)x(H_2O)x]$ in a 1:2:4 molar ratio is adjusted to pH 12 with NH_4OH. The resulting gelatinous material is heated at 350 °C for 3 days. These conditions result in complete conversion to highly crystalline $CaCuSi_4O_{10}$. The blue product (Figure 1b) consists of 40–60 μm crystal clusters with a uniform flowerlike morphology (see Figure S1 in the Supporting Information for additional images and a distribution analysis).

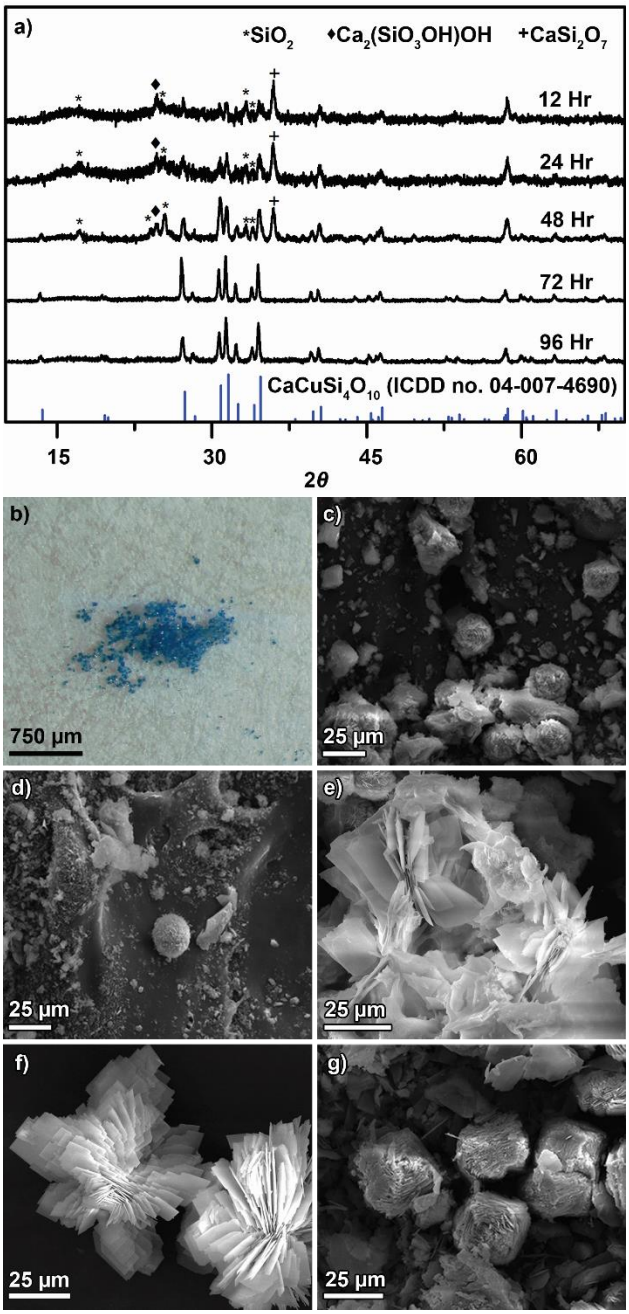

Figure 3.1 Hydrothermal formation of $CaCuSi_4O_{10}$ at 350 °C: a) PXRD patterns of products from 12-96 h reactions, b) optical microscopy image of phase pure $CaCuSi_4O_{10}$ produced with 72 h reaction time, and SEM images of products corresponding to c) 12, d) 24, e) 48, f) 72, and g) 96 h reaction times.

Monitoring this reaction from 12 to 96 h by powder X-ray diffraction (PXRD) (Figure 1a) shows that some $CaCuSi_4O_{10}$ forms early in the reaction, but SiO_2 and calcium silicates like

$Ca_2(SiO_3OH)OH$ and $CaSi_2O_7$ also are present. Scanning electron microscopy (SEM) illustrates a progression from heterogeneous morphologies at 12 and 24 h (Figures 1c and 1d, respectively) to distinct 25 μm $CaCuSi_4O_{10}$ platelets after 48 h (Figure 1e). At 72 h, the product is pure $CaCuSi_4O_{10}$ in the form of well-developed clusters of square-shaped crystals (Figure 1f). At 96 h and beyond, however, crystal delamination and fragmentation become noticeable: the clusters are smaller, exhibit frayed edges, and are covered in debris (Figure 1g). The previously reported exfoliation of layered $CaCuSi_4O_{10}$ in 80 °C water is the likely fragmentation mechanism here.[16] For this reason, 72 h is the ideal length of reaction time for hydrothermal $CaCuSi_4O_{10}$ crystal growth. Varying the calcium and copper sources, as well as the mineralizer, has significant effects on the products of the reaction. Table 1 summarizes the results of using $CaCl_2 \cdot 2H_2O$ versus $Ca(NO_3)_2 \cdot 4H_2O$ and $CuCl_2 \cdot 4H_2O$ versus $Cu(NO_3)_2 \cdot 2.5H_2O$ with either NH_4OH or NaOH.

Table 3.1. Hydrothermal experiments at 350 °C and 3000 psi

Reactants		**Mineralizer**	**Results (PXRD Analysis)**
Calcium source	**Copper Source**		
$CaCl_2 \cdot 2H_2O$	$Cu(NO_3)_2 \cdot 2.5H_2O$	NH_4OH	Bright blue crystals ($CaCuSi_4O_{10}$)
$Ca(NO_3)_2 \cdot 4H_2O$	$Cu(NO_3)_2 \cdot 2.5H_2O$	NH_4OH	Major: bright blue crystals ($CaCuSi_4O_{10}$); minor: larger clear crystals (SiO_2)
$CaCl_2 \cdot 2H_2O$	$CuCl_2 \cdot 4H_2O$	NH_4OH	Pale blue fibrous network [$Na_2CuSi_4O_{10}$, SiO_2, and $Na(Si_2O_4(OH))H_2O$]
$Ca(NO_3)_2 \cdot 4H_2O$	$CuCl_2 \cdot 4H_2O$	NH_4OH	Pale blue fibrous network ($Na_2CuSi_4O_{10}$ and SiO_2)
$CaCl_2 \cdot 2H_2O$	$Cu(NO_3)_2 \cdot 2.5H_2O$	NaOH	Pale blue fibrous network ($Na_2CuSi_4O_{10}$)
$Ca(NO_3)_2 \cdot 4H_2O$	$Cu(NO_3)_2 \cdot 2.5H_2O$	NaOH	Major: pale blue fibrous network ($Na_2CuSi_4O_{10}$); minor: bright blue crystals ($CaCuSi_4O_{10}$)
$CaCl_2 \cdot 2H_2O$	$CuCl_2 \cdot 4H_2O$	NaOH	Pale blue fibrous network ($Na_2CuSi_4O_{10}$, quartz, and SiO_2)
$Ca(NO_3)_2 \cdot 4H_2O$	$CuCl_2 \cdot 4H_2O$	NaOH	Pale blue fibrous network ($Na_2CuSi_4O_{10}$ and quartz)

First, these experiments show that NaOH is a problematic mineralizer in this system because the high concentration of Na^+ leads to preferential formation of $Na_2CuSi_4O_{10}$, a known tubular silicate.[17] The use of NH_4OH instead of NaOH mitigates this reaction pathway to a large extent, though $[Na_2O(SiO_2)_x(H_2O)_x]$ is another Na^+ source present in the system. We do not detect other previously reported sodium copper silicates, such as $Na_4Cu_2Si_{12}O_{27}(OH)_2{\cdot}2H_2O$ or $Na_2Cu_2Si_4O_{11}{\cdot}2H_2O$.[18]

Second, the reaction is relatively insensitive to the calcium source but sensitive to the copper source: the use of $CuCl_2\ {\cdot}4H_2O$ is consistently ineffective in producing $CaCuSi_4O_{10}$ compared to $Cu(NO_3)_2{\cdot}2.5H_2O$. This observation is surprising because both $CuCl_2{\cdot}4H_2O$ and $Cu(NO_3)_2{\cdot}2.5H_2O$ should convert to $Cu(OH)_2$, $[Cu(NH_3)_4]^{2+}$, and mixed ligand species in the presence of excess NH_4OH. In fact, prior studies have shown that both $CuCl_2$ and $Cu(NO_3)_2$ produce nanostructured CuO via putative $Cu(OH)_2$ when treated with NH_4OH under hydrothermal conditions.[19] Based on established hydrothermal chemistry, we speculate that strong Cu–Cl bonding persists at 350 °C, which influences the formation of reactive intermediates.[20] Although we observe the most phase pure $CaCuSi_4O_{10}$ product from $CaCl_2{\cdot}2H_2O$ and $Cu(NO_3)_2{\cdot}2.5H_2O$ starting materials, $CaCuSi_4O_{10}$ also forms from $Ca(NO_3)_2{\cdot}4H_2O$+$Cu(NO_3)_2{\cdot}2.5H_2O$. One expects little difference in chemistry between $CaCl_2$ and $Ca(NO_3)_2$ here, with both converting to $Ca(OH)_2$ under these conditions.[21] Curiously, a small amount of $CaCuSi_4O_{10}$ also is generated from $Ca(NO_3)_2{\cdot}4H_2O$ + $Cu(NO_3)_2\ {\cdot}2.5H_2O$ in the presence of NaOH, despite $Na_2CuSi_4O_{10}$ formation, which may reflect subtle effects related to the solubility and reactivity of calcium and copper hydroxides when approaching the supercritical point of water.[22]

Reaction temperature/pressure is another key parameter in this system. In general, a higher reaction temperature of 450 ˚C and corresponding pressure of 15000 psi disfavors $CaCuSi_4O_{10}$ formation (Table S1 in the Supporting Information). When using NH_4OH as the mineralizer, the dominant product at 450 ˚C is $CaSiO_3$ with minor amounts of $CuSiO_3$. In close similarity to 350 ˚C reactions, $Ca(NO_3)_2{\cdot}2H_2O$ + $CuCl_2{\cdot}2.5H_2O$ + NH_4OH yields $Na_2CuSi_4O_{10}$, as do all reactions utilizing NaOH. Again, some $CaCuSi_4O_{10}$ is generated when both nitrate salts are used in the presence of NaOH at 450 ˚C as at 350 ˚C (Figure S7 in the Supporting Information).

Of the eight reactions listed in Table 1, only one provides an isolable product at 250 ˚C with an autogenous pressure of about 1800 psi: $Ca(NO_3)_2{\cdot}4H_2O$ + $Cu(NO_3)_2{\cdot}2.5H_2O$ + $[Na_2O(SiO_2)_x(H_2O)_x]$ + NH_4OH. As illustrated in Figure 2, the interesting product consists of 0.1–0.2 mm bright blue crystals with a dumbbell morphology.

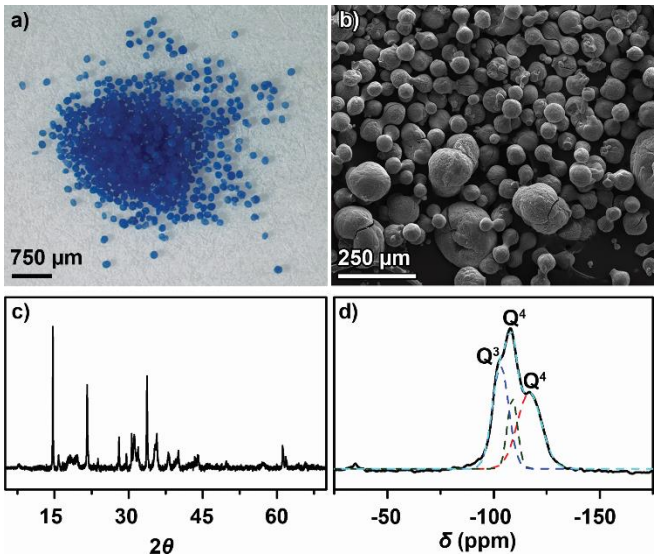

Figure 3.2. Micro-dumbbells formed at 250 °C: a) Optical microscopy image, b) SEM image, c) PXRD pattern, and d) experimental ^{29}Si NMR spectrum (black curve) with peak fitting (dashed curves)

Their color is, in fact, a more pure blue than $CaCuSi_4O_{10}$ (Figure S8 in the Supporting Information), but this material does not luminesce in the infrared range of 700–1400 nm (Figure

S9 in the Supporting Information). Elemental analysis (Table S2 in the Supporting Information) provides an approximate stoichiometry of $Ca_2CuSi_8O_{16}$. Although several crystalline calcium copper silicate compositions are known, including kinoite ($Ca_2Cu_2Si_3O_{10}\cdot 2H_2O$),[23] stringhamite ($CaCuSiO_4\cdot H_2O$),[24] and recently discovered diegogattaite ($Na_2CaCu_2Si_8O_{20}\cdot H_2O$),[25] the PXRD pattern of the micro-dumbbells (Figure 2c) does not match anything previously reported. However, the low-angle data show features similar to data from calcium silicates like gyrolite ($Ca_{16}Si_{24}O_{60}(OH)_8\cdot(14+x)H_2O$ and hillebrandite $Ca_2(SiO_3)(OH)_2$.[26] Gyrolite in particular is known to readily incorporate Cu^{2+} into its layered structure.[27] We further investigated the structure of the dumbbell material using solid-state ^{29}Si magic angle spinning (MAS) nuclear magnetic resonance (NMR) spectroscopy. The spectrum exhibits three overlapping peaks (Figure 2d) at -103, -109, and -117 ppm, which we assign to one Q^3 species [$Si(OSi)_3OH$] and two distinct Q^4 species [$Si(OSi)_4$]. Such a low silanol content is consistent with a porous framework silicate and is similar to data reported for Cu^{2+}-doped zeolites and mesoporous silica materials.[28] These results suggest that the dumbbells contain coordinated Cu^{2+} within pores or channels formed by the silicate structure.

The micro-dumbbells convert to $CaCuSi_4O_{10}$ when heated at 350 °C under hydrothermal conditions, with the cleanest reaction obtained by heating isolated dumbbells in deionized water. SEM analysis (Figure S11 in the Supporting Information) shows that the product mixture contains relatively thick $CaCuSi_4O_{10}$ crystals, thin $CaCuSi_4O_{10}$ platelets, and needlelike and globular morphologies that may correspond to unreacted material.

Conclusion

In conclusion, the conditions for the hydrothermal formation of $CaCuSi_4O_{10}$ are surprisingly specific. Although both $SrCuSi_4O_{10}$ and $BaCuSi_4O_{10}$ form in a range of temperatures and from variable precursors, highly crystalline and phase pure $CaCuSi_4O_{10}$ forms readily only at 350 °C using copper nitrate and ammonium hydroxide. This significant difference in chemistry explains in part why cuprorivaite is not found in the same natural mineral deposits as wesselsite ($SrCuSi_4O_{10}$) or effenbergerite ($BaCuSi_4O_{10}$).[29] The final question is, why has it taken until now for the hydrothermal formation of $CaCuSi_4O_{10}$ to be reported? We suggest that the experimental challenge of conducting hydrothermal reactions at temperatures >250 °C (beyond the capability of Teflon-lined pressure vessels) has been the main impediment to developing this chemistry.

References

1. a) H. Berke, *Angew. Chem. Int. Ed.* **2002**, *41*, 2483–2487; *Angew. Chem*. **2002**, *114*, 2595–2600; b) H. Berke, *Chem. Soc. Rev*. **2007**, *36*, 15–30.
2. T. E. Warner, in Synthesis Properties and Mineralogy of Important Inorganic Materials, Wiley, Chichester (UK), **2011**, pp. 26–49.
3. a) G. Pozza, D. Ajý, G. Chiari, F. De Zuane, M. Favaro, *J. Cult. Heritage* **2000**, *1*, 393–398; b) G. Accorsi, G. Verri, M. Bolognesi, N. Armaroli, C. Clementi, C. Miliani, A. Romani, *Chem. Commun*. **2009**, *23*, 3392–3394.
4. a) G. Verri, *Anal. Bioanal. Chem*. **2009**, *394*, 1011–1021; b) M. L. Sargent, in Tracking Color: The polychromy of Greek and Roman sculpture in the Ny Carlsberg Glyptotek (Ed.: J.S. Østergaard), **2012**, Ny Carlsberg Glyptotek, pp. 14–34.
5. Y. Zhuang, S. Tanabe, *Phys. Status Solidi C* **2012**, *9*, 2304–2307.
6. S. M. Borisov, C. Wìrth, U. Resch-Genger, I. Klimant, *Anal. Chem*. **2013**, *85*, 9371–9377.
7. Y. J. Li, S. Ye, C. H. Wang, X. M. Wang, Q. Y. Zhang, *J. Mater. Chem. C* **2014**, *2*, 10395–10402.
8. P. Garcia-Fernandez, M. Moreno, J. A. Aramburu, *Inorg. Chem.* **2015**, *54*, 192–199.
9. W. Chen, Y. Shi, Z. Chen, X. Sang, S. Zheng, X. Liu, J. Qiu, *J. Phys. Chem. C* **2015**, *119*, 20571–20577.
10. A. Pabst, Acta Crystallogr. **1959**, *12*, 733–739.
11. a) M. S. Tite, M. Bimson, M. R. Cowell, *Adv. Chem. Ser.* **1984**, *205*, 215–242; b) G. A. Mazzocchin, D. Rudello, C. Bragato, F. Agnoli, *J. Cult. Herit.* **2004**, *5*, 129–133; c) T. Pradell, N. Salvado, G. D. Hatton, M. S. Tite, *J. Am. Ceram. Soc.* **2006**, *89*, 1426–1431.

12. a) E. M. Hughes, M. J. Pack, S. E. Dann, M. T. Weller, *An. Quim. Int. Ed.* **1997**, *93*, 233–236; b) D. Johnson-McDaniel, T. T. Salguero, *J. Vis. Exp.* **2014**, *86*, e51686.

13. K. Byrappa, *Prog. Cryst. Growth Charact. Mater.* **2007**, *53*, 117–166.

14. a) C. Minguzzi, *Period. Mineral. Mag.* **1938**, *9*, 333–345; b) Hentschel, *Die Mineralien der Eifelvulkane (Lapis Monographie),* Wise, **1983**; c) N. W. Eastaugh, V.; Chaplin, T.; Siddall, R., The Pigment Compendium: A Dictionary of Historical Pigments, Elsevier Science, Burlington MA, **2004**, p. 136.

15. Y. Chen, M. Y. Shang, X. F. Wu, S. H. Feng, *CrystEngComm* **2014**, *16*, 5418–5423.

16. D. Johnson-McDaniel, C. A. Barrett, A. Sharafi, T. T. Salguero, *J. Am. Chem. Soc.* **2013**, *135*, 1677–1679.

17. K. Kawamura, A. Kawahara, *Acta Crystallographica Section B* **1977**, *33*, 1071–1075.

18. a) X. Q. Wang, L. M. Liu, A. J. Jacobson, *Angew. Chem. Int. Ed* **2003**, *42*, 2044–2047; b) X. Q. Wang, L. M. Liu, L. B. Wang, A. J. Jacobson, *Solid State Sci.* **2005**, *7*, 1415–1422.

19. G. Filipiĉ, U. Cvelbar, *Nanotechnology* **2012**, *23*, 16.

20. T. J. Williams, P. A. Candela, P. M. Piccoli, *Contrib. Mineral. Petrol.* **1995**, *121*, 388–399.

21. W. Liu, H. Xu, X. Yang, X. Shi, Y. Chen, *J. Cent. South Univ. Technol. (Engl. Ed.)* **2012**, *19*, 2751–2754.

22. K. Sue, Y. Hakuta, R. L. Smith, T. Adschiri, K. Arai, *J. Chem. Eng. Data* **1999**, *44*, 1422–1426.

23. R. L. Frost, Y. Xi, *Spectrochim. Acta A* **2012**, *89*, 88–92.

24. R. L. Frost, Y. Xi, *Spectrochim. Acta A* **2012**, *91*, 324–328.

25. a) M. S. Rumsey, M. D. Welch, A. R. Kampf, J. Spratt, *Mineralogical Magazine* **2013**, *77*, 3155–3162; b) M. D. Welch, M. S. Rumsey, *J. Solid State Chem.* **2013**, *203*, 260–265.

26. a) Y. S. Dai, J. E. Post, *Am. Mineral.* **1995**, *80*, 841–844; b) I. G. Richardson, *Cem. Concr. Res.* **2008**, *38*, 137–158; c) A. Baltušnikas, R. Šiaučiūnas, I. Lukošiūtė, K. Baltakys, A. Eisinas, R. Kriūkienė, *Mater. Sci. Medzg.* **2015**, *21*, 111–116.

27. A. Bankauskaite, K. Baltakys, *Mater. Sci.* **2009**, *27*, 899–908.

28. S. Inagaki, I. Kawamura, Y. Sasaki, K. Yoshida, Y. Kubota, A. Naito, *Phys. Chem. Chem. Phys.* **2013**, *15*, 13523–13531.

29. a) G. Giester, B. Rieck, *Mineral. Mag.* **1994**, *58*, 663–670; b) G. Giester, B. Rieck, *Mineral. Mag.* **1996**, *60*, 795–798.

CHAPTER 4

SIZE AND MORPHOLOGICAL CONTROL OF STRONTIUM AND BARIUM COPPER TETRASILICATES VIA HYDROTHERMAL SYNTHESIS

Darrah Johnson-McDaniel and Tina T. Salguero. To be submitted to *The Journal of Crystal Growth and Design.*

Abstract

We can control the crystal size and morphology of $SrCuSi_4O_{10}$ and $BaCuSi_4O_{10}$ via hydrothermal synthesis. By varying the precursors, reaction time, and temperature we have grown uniform crystals on the micro scale with morphologies ranging from flower-like clusters of platelets to nanoscrolls. By adjusting the stoichiometry, we have grown platelets of $SrCuSi_4O_{10}$ of varied thickness. Additionally, we have determined that $BaCuSi_4O_{10}$ grows off the surface of CuO and $CuSiO_3$. Due to our hydrothermally synthesized crystals uniform size and morphology, they would be an excellent target for exfoliation into nanosheets. Thus, this previously unexplored method provides the first process to control and tune the size and morphology of the $ACuSi_4O_{10}$ series on both the micro and nano scale.

Introduction

The metal copper tetrasilicate series, $ACuSi_4O_{10}$, comprises three brilliantly blue materials $CaCuSi_4O_{10}$, $SrCuSi_4O_{10}$, and $BaCuSi_4O_{10}$. Pigment analogues of both $CaCuSi_4O_{10}$ and $BaCuSi_4O_{10}$ were first synthesized out of necessity due to a lack of inexpensive, readily available blue materials and they were used extensively as colorants for paintings, sculptures, and pottery throughout ancient world from 4000 BC to 800 AD.[1] Much later, $CaCuSi_4O_{10}$ and $BaCuSi_4O_{10}$ were found as the rare minerals, Cuprorivaite and Effenbergerite, along with the third member of the $ACuSi_4O_{10}$ series, Wesselsite ($SrCuSi_4O_{10}$).[2] The same copper center in square planer coordination that is responsible for the intense blue color so prized by the ancient people, also makes these materials strongly luminescent; thus expanding the $ACuSi_4O_{10}$ series from its traditional role as pigments into new avenues such as telecommunications, security inks, biological imaging, and as phosphors.[3]

For applications such as biological imaging, control over the size and morphology is quite significant. While the $ACuSi_4O_{10}$ series facilely exfoliates into monolayer nanosheets using agitation of the bulk powder in hot water[4], the dimensions of the resulting nanosheets are highly dependent on the size of the bulk material.[4] The traditional methods for synthesizing the $ACuSi_4O_{10}$ series, namely high temperature solid state[5] and melt flux chemistry[6], do not produce crystals of uniform size or offer control over the final size of the product. Hydrothermal synthetic methods, however, can provide a route for tuning crystal size and morphology[7] as well as producing defect free crystals, at much lower temperatures.[8]

The rare mineralogical forms of the $ACuSi_4O_{10}$ were assumed to have formed under hydrothermal conditions.[2b] And indeed, $SrCuSi_4O_{10}$ and $BaCuSi_4O_{10}$ both readily form into microcrystals using a simple hydrothermal method.[9] $CaCuSi_4O_{10}$, other the other hand, only

forms hydrothermally under very specific conditions, and requires a higher temperature for formation than its isostructural brethren.[10]

Altogether there have been relatively few reports on the hydrothermal chemistry of the $ACuSi_4O_{10}$ series, and therefore we were interested in further investigation, not only to see what the effects time, temperature, stoichiometry, and reactants have on the final size and morphology, but also for what information this chemistry can provide us about this ancient and fascinating class of materials.

Experimental

Materials. Copper chloride dihydrate (Baker Analyzed A.C.S. Reagent, 99.4% purity), and nitric acid (Baker Analyzed A.C.S. Reagent, 69.0-70.0%) were purchased from J.T. Baker and used as received. CuO nanoflowers were synthesized using the method described by Yong-kui, et al.[11] Strontium chloride hexahydrate (ACS Reagent, 99% purity), strontium nitrate tetrahydrate (ACS Reagent, 99.0+% purity), barium chloride (99.9% trace metals basis purity), barium chloride dihydrate (ACS Reagent, ≥ 99% purity), barium nitrate (ACS Reagent, ≥ 99.0% purity), sodium silicate [$Na_2O(SiO_2)_x(H_2O)_x$] (Reagent Grade purity), LUDOX SM colloidal silica (30 wt. % suspended in H_2O), sodium carbonate (BioXtra, ≥ 99% purity), sodium hydroxide (ACS Reagent, ≥ 97.0% purity), potassium hydroxide (ACS Reagent, ≥ 85.0% purity), Hydrochloric acid (ACS Reagent, 37% in H_2O), polydiallyldimethylammonium chloride (20 wt. % in H_2O), polyethylenimine (50 wt. % in H_2O), sodium dodecyl sulfate (SigmaUltra, ≥ 99.0% purity) were purchased from Sigma-Aldrich and used as received. Copper nitrate dihydrate (certified ACS) was purchased from Fischer Scientific and used as received. METSO BEADS® 2048 (sodium metasilicate), RU® Sodium Silicate (47.1% solution in H_2O), and KASIL® 1 (potassium silicate,

29.1% solution in H_2O) were samples obtained from PQ Corporation and were used as received. Strontium chloride was dehydrated from the strontium chloride hexahydrate by heating at 100 °C overnight in a vacuum oven. Deionized water was generated with a Barnstead NANOpure II water purification unit.

Representative (Baseline) Hydrothermal Synthesis of $SrCuSi_4O_{10}$. 1.18 mmol of $CuCl_2 \cdot 2H_2O$ and 1.18 mmol of $SrCl_2 \cdot 6H_2O$ were dissolved in 30 mL of deionized water. While monitoring the pH and stirring, 1.07 mL of sodium silicate solution (4.72 mmol of SiO_2) was added drop-wise to the solution. The final pH of the solution was then adjusted to 12 using 5 M NaOH. The resulting gel-like solution was placed into a 45 mL capacity Teflon-lined autoclave and heated in a box furnace at 250 °C for the desired amount of time. Once the reaction was complete and cooled to room temperature, the supernatant was decanted, the blue crystals were washed with 45 mL of 1 M HNO_3, and then collected by vacuum filtration. For the crystal formation PXRD time study, the products were collected by vacuum filtration without washing.

Variations on the Hydrothermal Synthesis of $SrCuSi_4O_{10}$. For the variations, stoichiometric amounts of CuO, CuO nanoflowers, $Cu(NO_3)_2 \cdot 2.5H_2O$, $SrCl_2$, $Sr(NO_3)_2 \cdot 4H_2O$, or commercial colloidal silicates were substituted into the baseline synthesis. Additionally, 3% of Na_2CO_3, 20% of KOH, and 20% of Tween 20 were added to the baseline reaction. For reactions with $Cu(NO_3)_2 \cdot 2.5H_2O$ and $Sr(NO_3)_2 \cdot 4H_2O$, the pH was adjusted with NH_4OH.

Representative (Baseline) Hydrothermal Synthesis of $BaCuSi_4O_{10}$. 1.06 mmol of $CuCl_2 \cdot 2H_2O$ and 1.06 mmol of $BaCl_2$ were dissolved in 30 mL of deionized water. While monitoring the pH and stirring, 0.96 mL of sodium silicate solution (4.22 mmol of SiO_2) was added drop-wise to the solution. The final pH of the solution was then adjusted to 12 using 5 M NaOH. The resulting gel-like solution was placed into a 45 mL capacity Teflon-lined autoclave

and heated in a box furnace at 250 °C for the desired amount of time. Once the reaction was complete and cooled to room temperature, the supernatant was decanted, the blue crystals were washed with 45 mL of 1 M HNO_3, and then collected by vacuum filtration. For the crystal formation PXRD time study, the products were collected by vacuum filtration without washing.

Variations on Hydrothermal Synthesis of $BaCuSi_4O_{10}$. For the variations, stoichiometric amounts of CuO, CuO nanoflowers, $Cu(NO_3)_2 \cdot 2.5H_2O$, $BaCl_2 \cdot 2H_2O$, $Ba(NO_3)_2$, or commercial colloidal silicates were used. Additionally, 3% of Na_2CO_3, 20% of KOH, and 20% of Tween 20 were added to the baseline reaction. For the 20% KOH reaction, the pH was adjusted down to 12 using 1 M HCl. For reactions with $Cu(NO_3)_2 \cdot 2.5H_2O$ and $Ba(NO_3)_2$, the pH was adjusted with NH_4OH.

High Temperature Hydrothermal Reactions. 0.8 mL of the gelatinous reaction mixture was placed into a silver ampule, welded shut, placed in a high temperature autoclave (filled with deionized water to counter-pressure the ampules), and heated to 350 °C for 12-96 hours. Once the reaction time was complete, the vessel was cooled to room temperature, the solid product was washed with water and collected by vacuum filtration.

Exfoliation of $ACuSi_4O_{10}$. To exfoliate the $ACuSi_4O_{10}$ crystals, we followed the method described in our previous work.[4, 12]

Characterization. The identity of the synthesized pigments was confirmed using a Bruker D8-Advance powder X-ray diffractometer (Co-Kα radiation source) operated at 40 mA and 40 kV. The PXRD patterns were recorded in the 2θ range of 10−70° with a scanning rate of 0.1 sec $step^{-1}$. The morphology of the pigments was examined by FEI Inspect F field emission gun scanning electron microscope (SEM) operated at 20 kV. The samples were prepared for SEM by sprinkling the powders on carbon sticky tape and then coating with a thin layer of gold to

enhance conductivity. The exfoliated nanosheets were characterized using a FEI Tecnai 20 (200 kV) transmission electron microscope (TEM) with selected area electron diffraction (SAED) capability.

Results and Discussion

We have developed a method of controlling both the crystal growth and morphology of $SrCuSi_4O_{10}$ and $BaCuSi_4O_{10}$ by varying time, temperature, stoichiometry, and reactants. For the purposes of simplicity, we will refer to reactions with chloride salts, a sodium silicate solution, and NaOH as a mineralizer run at 250 °C as our baseline synthesis.

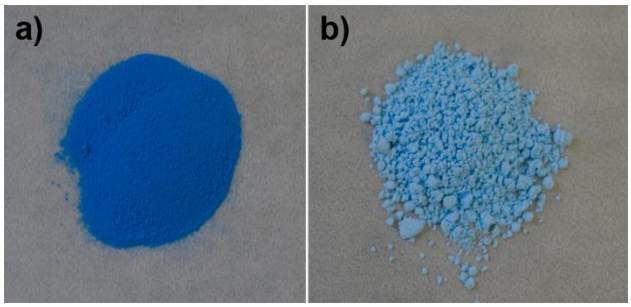

Figure 4.1. Photographs of the baseline synthesis run for 48 h of a) $SrCuSi_4O_{10}$ and b) $BaCuSi_4O_{10}$ show the stark difference in color between the two materials.

Our baseline hydrothermal method run for 48 h produced vividly blue flower-like aggregates of $SrCuSi_4O_{10}$ platelets that were ~35-45 μm in size and clusters of light blue $BaCuSi_4O_{10}$ platelets that were ~2-10 μm (Figures 4.1). $CaCuSi_4O_{10}$ did not form at 250 °C, and therefore cannot be compared to the rest of the series.

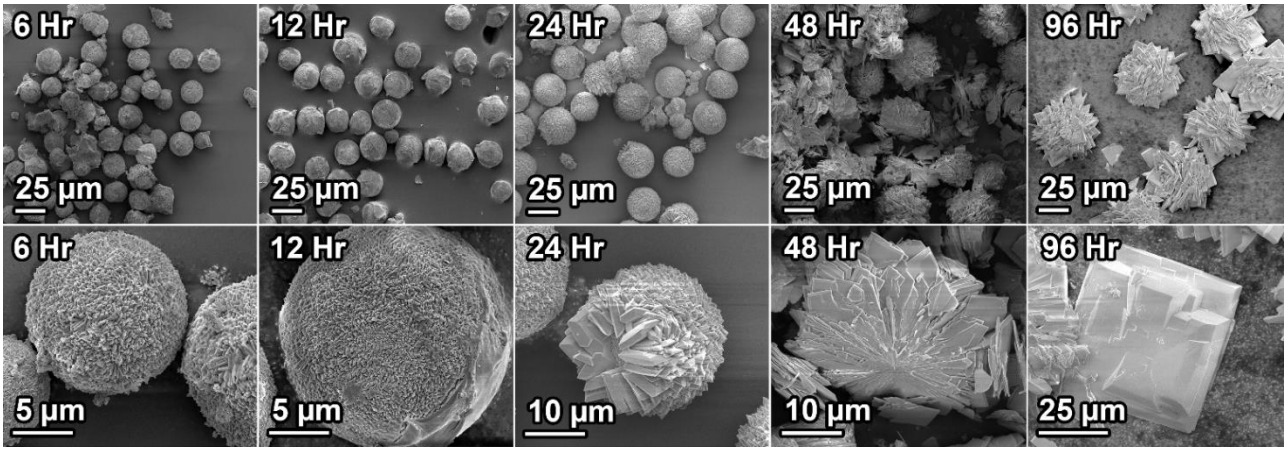

Figure 4.2. Time study of the morphology of $SrCuSi_4O_{10}$ crystals formed during the baseline hydrothermal synthesis method.

We performed a time study from 6-96 hours. For $SrCuSi_4O_{10}$, longer reaction times produced larger crystals; we hypothesize that the reaction proceeded via a two-step process: 1) a rapid nucleation growth mechanism that formed spherical clusters of crystals and then 2) further crystal growth. The results of the time study confirmed our hypothesis. Examining the crystals using scanning electron microcopy (SEM) (Figure 4.2), we observed the following: at 6 h of growth there were spherical crystals ~10 µm in size comprised of small platelets; these crystals increased in size to ~15 µm after 12 h of growth, but otherwise the morphology was not altered. After 24 h of growth, more well-defined platelets started to emerge. After 48 h of growth, flowerlike structures were visible which continued growing in size up to 96 h where the flower-like clusters of platelets were now joined by a few free standing platelets that had the ideal crystal shape for the $ACuSi_4O_{10}$ series.[13] We did not observe any further crystal growth, even after two weeks of reaction.

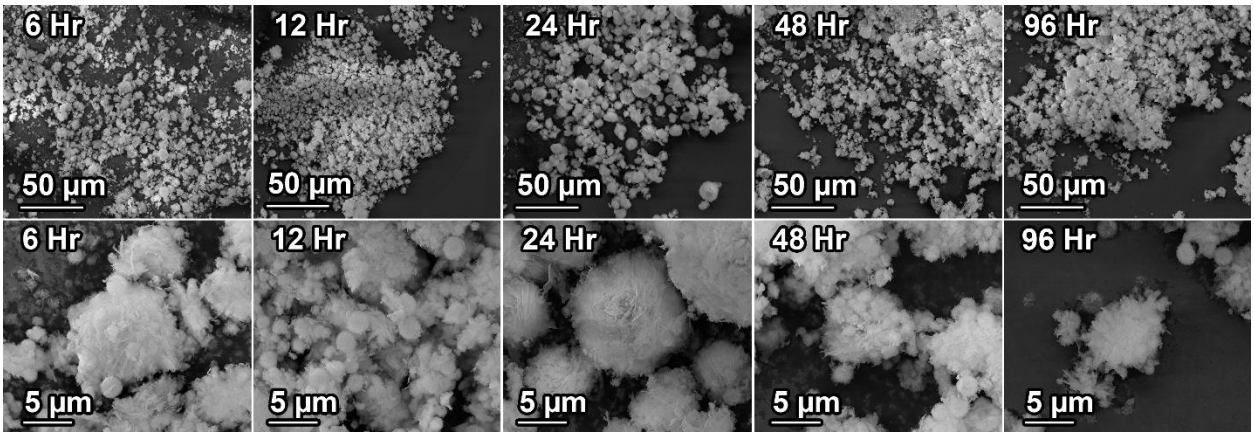

Figure 4.3. Time study of the morphology of $BaCuSi_4O_{10}$ crystals formed during the baseline hydrothermal synthesis method.

The hydrothermal growth of $BaCuSi_4O_{10}$ proceeded in a different manner than $SrCuSi_4O_{10}$. The color of the isolated hydrothermal $BaCuSi_4O_{10}$ product was a much lighter blue then $SrCuSi_4O_{10}$ was (Figure 4.1). The initial nucleation remained the same, but there was no second growth step. By SEM analysis, the baseline synthesis produced crystals that were aggregated together in clusters of varying sizes, and the crystal growth was largely complete after 6 h (Figure 4.3). We hypothesize that the overall crystal formation of $BaCuSi_4O_{10}$ proceeded through a different pathway than the $SrCuSi_4O_{10}$ reaction. Examining the early stages of crystal growth for both $SrCuSi_4O_{10}$ and $BaCuSi_4O_{10}$ by powder X-ray diffraction (PXRD) confirmed the difference. In the case of $SruCiSi_4O_{10}$, there was no crystal formation until 4 h, and there was no formation of intermediates (Figure 4.4a). $BaCuSi_4O_{10}$, on the other hand, first formed crystalline products such as $BaCuSi_2O_6$, which is known to form in $BaCuSi_4O_{10}$ reactions[1b], before forming $BaCuSi_4O_{10}$ after 3 h (figure 4.4b).

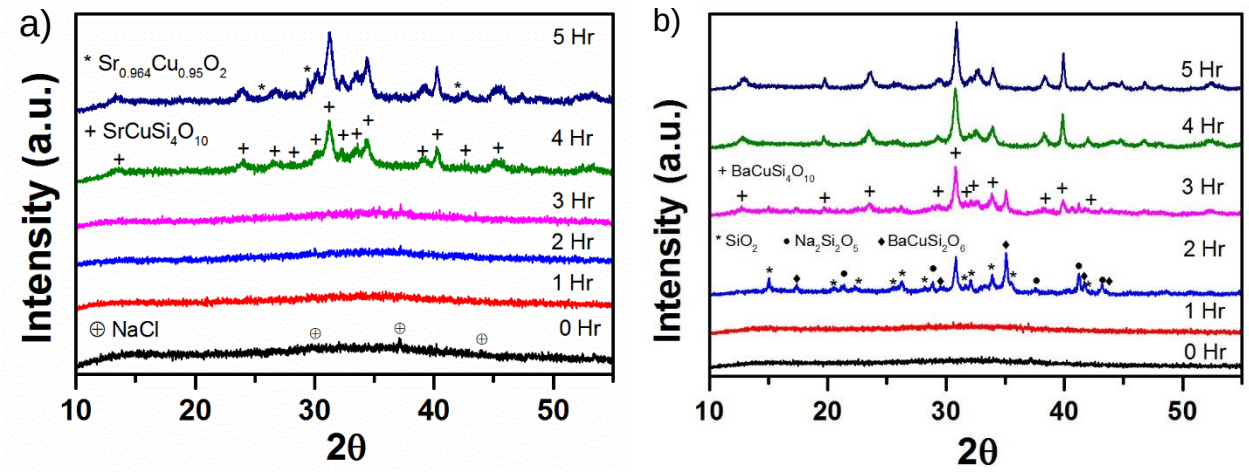

Figure 4.4. a) PXRD patterns collected at early points in the crystal formation of $SrCuSi_4O_{10}$ using the baseline hydrothermal synthesis method. Symbols for identified species include: + for $SrCuSi_4O_{10}$ (ICCD 012-0511) and * for $Sr_{0.964}Cu_{0.95}O_2$ (ICCD 083-0266). b) PXRD patterns collected at early points in the crystal formation of $BaCuSi_4O_{10}$ using the baseline hydrothermal synthesis method. Symbols for identified species include: * for SiO_2 (ICCD 043-0745), ♦ for $BaCuSi_2O_6$ (043-0300), • for $Na_2Si_2O_5$ (ICCD 023-0529), and + for $BaCuSi_4O_{10}$ (AMSCD 0013766).

Looking at the isolated products of the PXRD time study, it was again clear that $BaCuSi_4O_{10}$ had a much shorter crystal growth period than $SrCuSi_4O_{10}$. The relative intensity of the patterns for $BaCuSi_4O_{10}$ did not increase appreciably over the course of the 96 h time study, whereas the intensity of the $SrCuSi_4O_{10}$ increased dramatically, indicating the formation of larger and more crystalline materials.

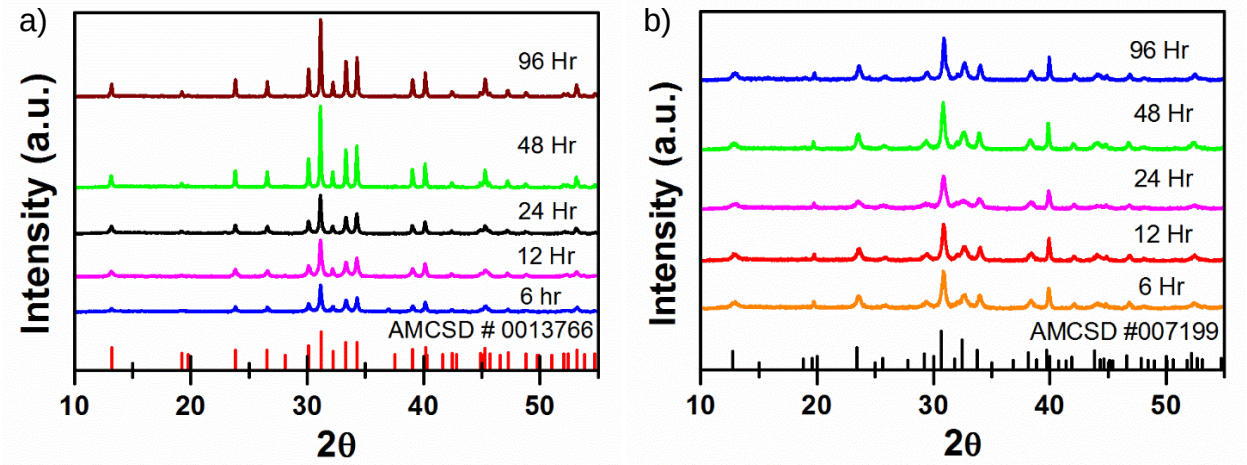

Figure 4.5. PXRD patterns of a) isolated $SrCuSi_4O_{10}$ products formed using the baseline hydrothermal synthesis method with varying reaction times and b) isolated $BaCuSi_4O_{10}$ products formed using the baseline hydrothermal synthesis method with varying reaction times.

Morphology Study

We found that the morphology of the products changed with different starting materials. Overall, the morphology that both $SrCuSi_4O_{10}$ and $BaCuSi_4O_{10}$ preferred was a spherical shape comprised of small platelets. However, we had noticed that using different precursors affected the morphology of the final product. To that end, starting with $SrCuSi_4O_{10}$, we examined the effect of changing the initial precursors.

Varying the copper reactant: changing the copper precursor from $CuCl_2 \cdot 2H_2O$ resulted in different morphologies (Figure 4.6). Using CuO, the spheres of $SrCuSi_4O_{10}$ were no longer well formed; changing the precursor to more reactive CuO nanoflowers, formed clusters of smaller nanoflowers (Figure 4.6). Using $Cu(OH)_2$, led to a directed growth of $SrCuSi_4O_{10}$ into layered platelets. The latter morphology change is potentially due to the existence of ionic $Cu(OH)_2$ in solution; thus being used as a nucleation point and directing the growth anisotropically.

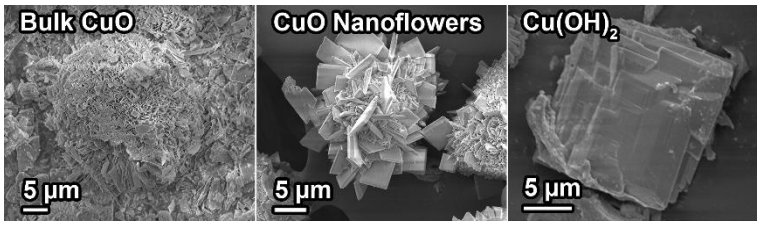

Figure 4.6. Morphology change of $SrCuSi_4O_{10}$ crystals when varying copper starting material run at 250 °C for 48 h.

Varying the silica reactant: changing the silica precursor from sodium silicate resulted in different morphologies as well (Figure 4.7). Using colloidal silica resulted in square shapes with more well defined platelets. KASIL silicate, a commercial potassium silicate, provided well defined spheres. That morphology was maintained when using RU silicate, a sodium silicate with a higher silica percentage, and METSO silica beads.

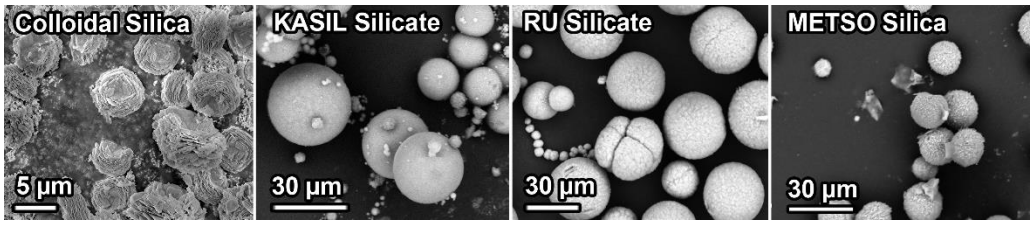

Figure 4.7. Morphology change of $SrCuSi_4O_{10}$ crystals when varying silica starting material run at 250 °C for 48 h.

Growth directing agents: hydrothermal reactions are well suited for introducing growth directing agents.[14] On the addition of 3% of sodium carbonate, and after 12 h of reaction the platelets were no longer tightly grown together, but did not have a well-defined crystal morphology. The excess sodium prevented the formation of spheres. This could potentially be due to the increased amount of sodium ions changing the dissolution and nucleation kinetics of the reaction.[15] After 48 h of growth, the crystals were more defined, and were again clustered together. Addition of Tween 20 as a templating agent did not influence the morphology, but did keep the platelets from growing further.

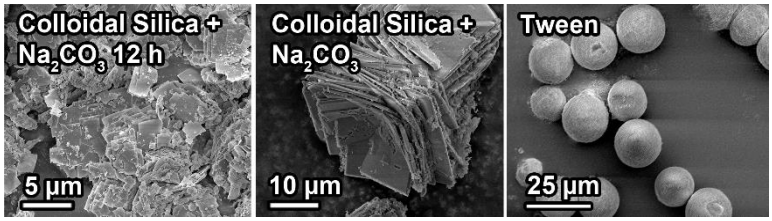

Figure 4.8. Morphology change of the $SrCuSi_4O_{10}$ crystals when the baseline synthesis was run at 250 °C for 48 h with various additives.

Varying the mineralizer: using KOH in place of NaOH produced the usual spheres comprised of platelets (Figure 4.9).

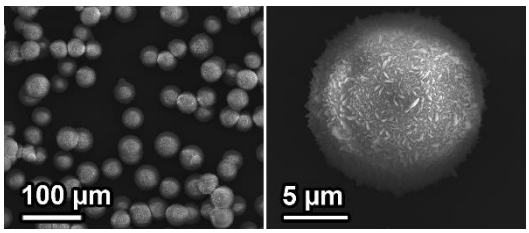

Figure 4.9. Morphology of the $SrCuSi_4O_{10}$ crystals when the baseline synthesis was run at 250 °C for 48 h with KOH.

CsOH produced similar appearing spheres to those formed using KOH (Figure 4.10). However, from the SEM images, it appeared that the platelets were forming as a crust on the outside of the sphere. The inside appeared to be comprised of much smaller crystals.

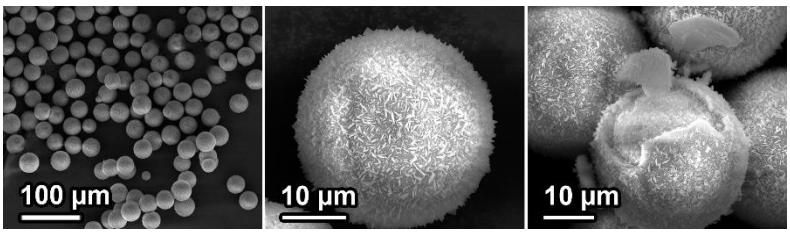

Figure 4.10. Morphology of the $SrCuSi_4O_{10}$ crystals when the baseline synthesis was run at 250 °C for 48 h with CsOH

Using the reagents that were ideal for crystal growth for $CaCuSi_4O_{10}$ produced the usual spheres, however there were more square shaped clusters of platelets, and also smaller clusters of platelets ~2 µm (Figure).

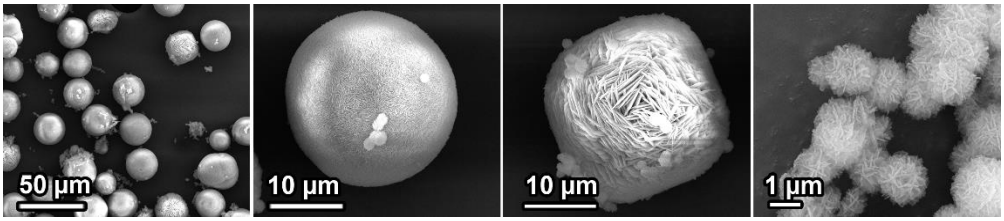

Figure 4.11. Morphology of $SrCuSi_4O_{10}$ from reaction of nitrate salts with NH_4OH run at 250 °C for 48 h.

Overall, $SrCuSi_4O_{10}$ favored a spherical morphology. However, by increasing the reaction time or by changing the reactants, we could vary the crystal morphology to form either flowerlike structures or free standing platelets. Additionally, we could change the crystal size by either changing the time or the reactants.

The morphology of $BaCuSi_4O_{10}$ was also dependent on starting material, but again, it reacted differently than $SrCuSi_4O_{10}$.

Varying the copper reactant: the morphology did not change that dramatically when the copper precursor was changed (Figure 4.10). Using bulk CuO oxide produced spherical clusters of platelets, as well as loose platelets. Changing to CuO nanoflowers produced larger, well-formed flowerlike structures; possibly due to the increased reactivity of the nanosized product. Using $Cu(OH)_2$ again produced spherical clusters of platelets, and did not seem to have the growth directing effect that it had for $SrCuSi_4O_{10}$.

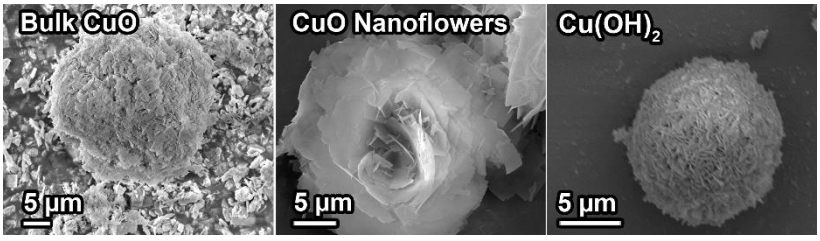

Figure 4.10. Morphology change of $BaCuSi_4O_{10}$ when varying copper starting material run at 250 °C for 48 h.

Varying the silica reactant: changing the silica precursor from sodium silicate resulted in different morphologies (Figure 4.11). Using the RU silicate produced loose clusters of thin

platelets. When potassium silicate (KASIL) was used, $BaCuSi_4O_{10}$ formed into a cluster of thin platelets. When the silica beads were used, $BaCuSi_4O_{10}$ formed into thin, but well-defined platelets clustered in a flower-like formation.

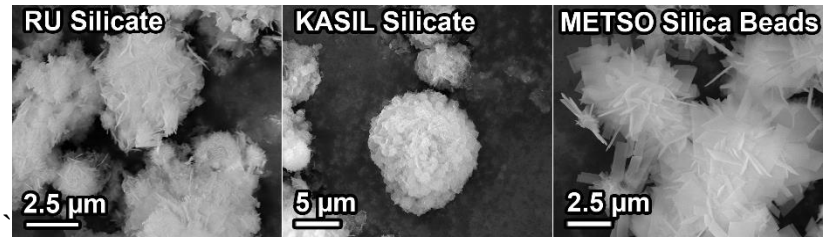

Figure 4.11. Morphology change of $BaCuSi_4O_{10}$ when varying silica starting material run at 250 °C for 48 h.

However, when we combined the potassium silicate with KOH as the mineralizer, the result was a mixed product of well-defined thin platelets and nanoscrolls. The nanoscrolls could potentially be caused by potassium ions inserting into the thin $BaCuSi_4O_{10}$ sheets and consequently rolling up to remove strain.

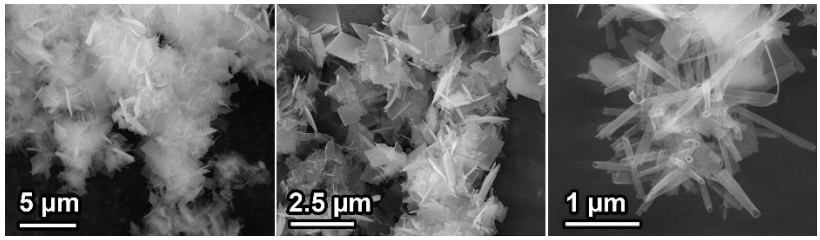

Figure 4.12. SEM images showing the platelet and nanoscroll morphology of $BaCuSi_4O_{10}$ using KASIL silicate and KOH as the mineralizer run at 250 °C for 48 h.

Growth directing agents: again, we added Na_2CO_3 and Tween 20 to try to direct the growth of the product (Figure 4.). However, neither one seemed to have much of an effect on the final morphology, although the size of the crystal aggregates when Tween was used as an additive was smaller than the baseline reaction.

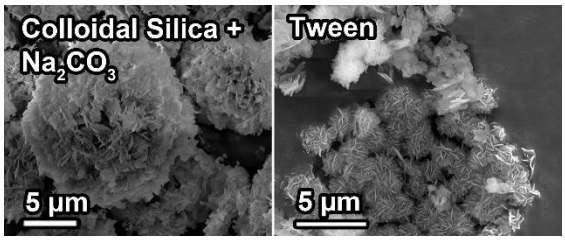

Figure 4.13. Morphology change of the $BaCuSi_4O_{10}$ crystals when the baseline synthesis was run at 250 °C for 48 h with various additives.

Varying the mineralizer: changing the mineralizer did not have a drastic effect on the morphology or size of the final product. Using KOH in place of NaOH, produced thin platelets aggregated together in spherical shapes (Figure 4.14).

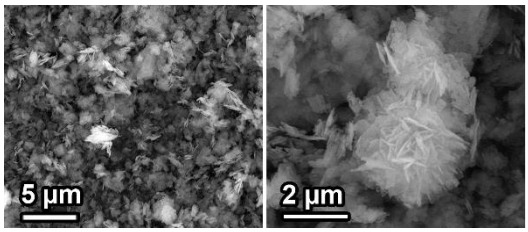

Figure 4.14. Morphology of the $SrCuSi_4O_{10}$ crystals when the baseline synthesis was run at 250 °C for 48 h with KOH.

Using CsOH, produced similar thin platelets aggregated together in spherical shapes to the previous reaction using KOH, although the spherical aggregates were more uniform in the former case (Figure 4.15).

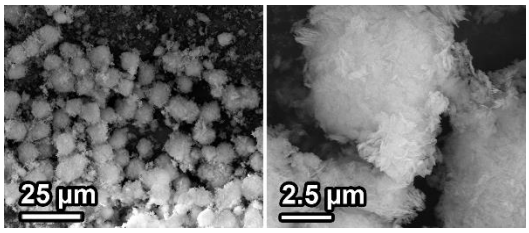

Figure 4.15. Morphology of the $SrCuSi_4O_{10}$ crystals when the baseline synthesis was run at 250 °C for 48 h with CsOH.

Using the reagents that were ideal for crystal growth for $CaCuSi_4O_{10}$ produced the usual spherical aggregates of platelets (Figure 4.16).

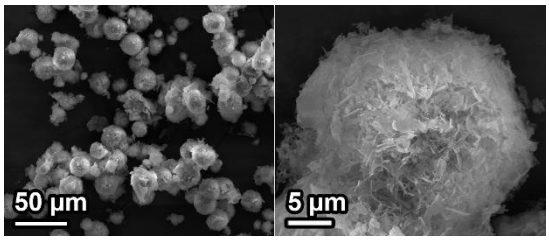

Figure 4.16. Morphology of $BaCuSi_4O_{10}$ from reaction of nitrate salts with NH_4OH run at 250 °C for 48 h.

Overall, while the morphology that $BaCuSi_4O_{10}$ favored was platelets aggregated into spheres, we were again able to change it by varying the precursor. Although the size of the platelets formed remained relatively consistent, we were able to synthesize flowerlike structures using CuO nanoflowers, and form nanoscrolls using potassium silicate and KOH. For $BaCuSi_4O_{10}$, the choice of silica reactant seemed to be the largest influencing factor on the final morphology.

Temperature Study

Reaction temperature was an important factor for the initial formation of crystals, and also played a role in determining the morphology and size of the final product. As previously mentioned, $CaCuSi_4O_{10}$ only formed at the specific temperature of 350 °C. It did not react at lower temperatures and higher temperatures lead to the formation of $Na_2CuSi_4O_{10}$. While, $Na_2CuSi_4O_{10}$ did not form in reactions with $SrCuSi_4O_{10}$ and $BaCuSi_4O_{10}$ and they both reacted at lower temperatures, there was still a temperature dependence. For $SrCuSi_4O_{10}$, the reaction does not proceed at temperatures lower than 250 °C. $BaCuSi_4O_{10}$ was more reactive and could form as low as 200 °C. At higher temperatures, the morphology of the products was slightly different from those formed in lower temperature reactions. $SrCuSi_4O_{10}$ still formed into flower-like clusters of platelets at 350 and 450 °C, however the crystal size was much smaller, and the

crystals were shaped more like swords instead of rectangles (Figure 4.17). Additionally, there were a few larger single crystals in the higher temperature reactions (Figure 4.17).

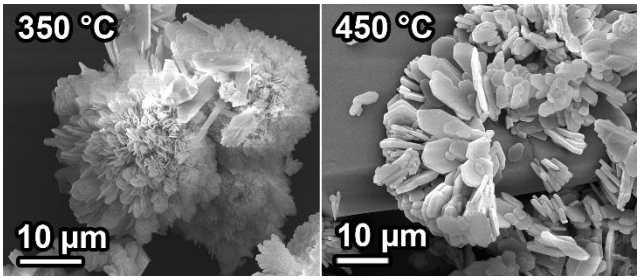

Figure 4.17. Morphology of baseline $SrCuSi_4O_{10}$ reaction run for 4 days at a) 350 °C and b) 450 °C.

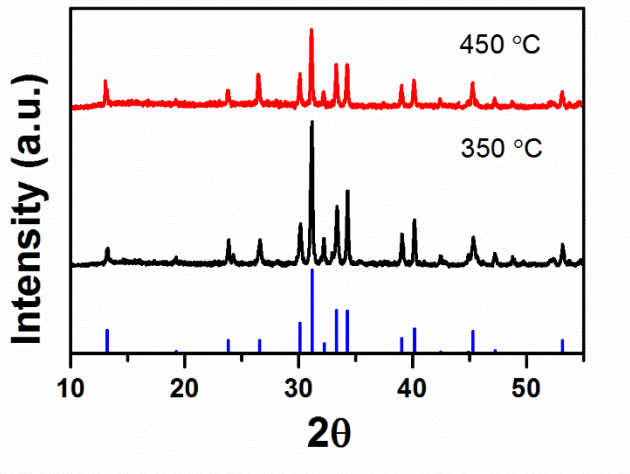

Figure 4.18. Powder diffraction of baseline $SrCuSi_4O_{10}$ reaction run at 350 °C and 450 °C for 4 days.

$BaCuSi_4O_{10}$ synthesized at higher temperatures produced different size crystals (Figure 4.19). At 350 °C, the crystals appeared to be thicker and did not aggregate as much, but the morphology was similar to that of the lower temperature reactions. At 450 °C, the crystals were larger still, several microns in length. Higher temperatures seemed to grow (comparatively) larger and thicker crystals.

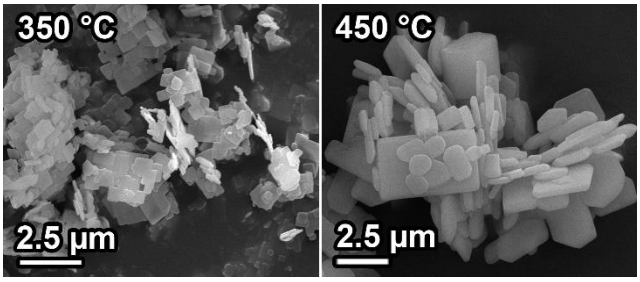

Figure 4.19. Morphology of baseline $BaCuSi_4O_{10}$ reaction run for 4 days at 350 °C and 450 °C.

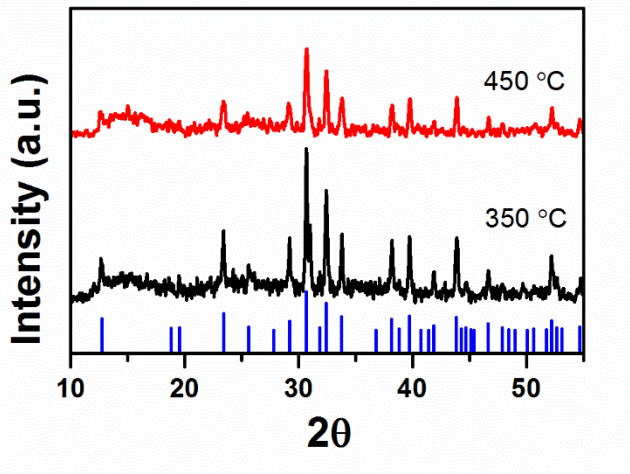

Figure 4.20. PXRD of the baseline $BaCuSi_4O_{10}$ reaction run for 4 days at 350 °C and 450 °C.

Synthesizing $SrCuSi_4O_{10}$ and $BaCuSi_4O_{10}$ using similar precursors and setting the reaction parameters to the same conditions that were previously determined for the optimum hydrothermal synthesis of $CaCuSi_4O_{10}$ produced mixed results. Instead of forming aggregates of thin platelets like the baseline synthesis at 350 ˚C did, $SrCuSi_4O_{10}$ formed into the flower-like clusters that were similar to those found in the baseline synthesis run at 250 ˚C (Figure 4.21). At 450 ˚C, the platelets were larger and more well-defined (Figure 4.21).

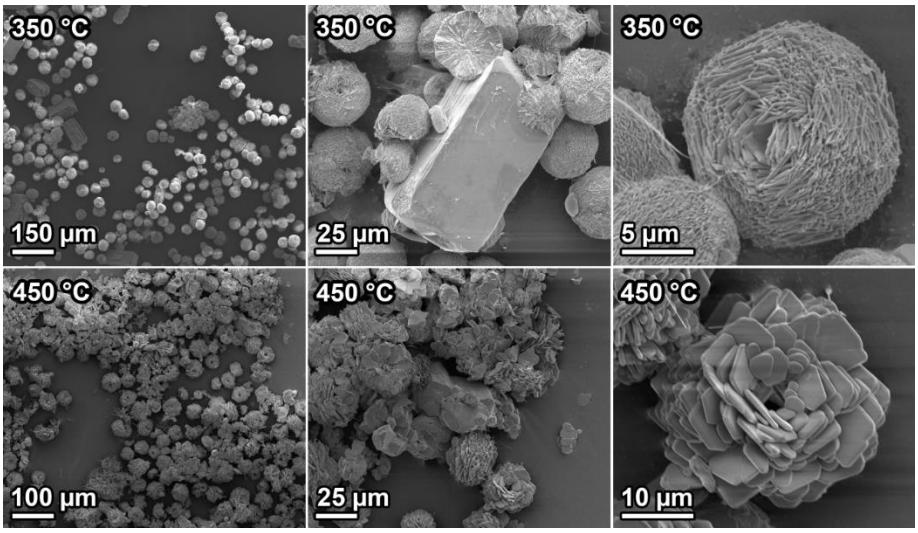

Figure 4.21. $SrCuSi_4O_{10}$ using nitrate salts and NH_4OH reacted at 350 °C and 450 °C for 4 days.

$BaCuSi_4O_{10}$ formed at the higher temperatures with the nitrate salts as a mixture with SiO_2, but observing the product by SEM, it did not have a well-defined morphology at 350 ˚C (Figure 4.22). However, the reaction at 450 ˚C did show much larger and well defined crystals.

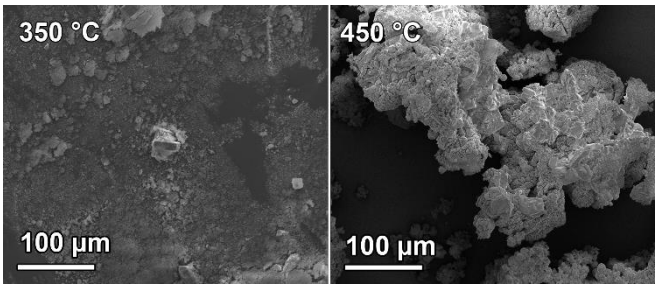

Figure 4.22. $BaCuSi_4O_{10}$ using nitrate salts and NH_4OH reacted at 350 °C and 450 °C for 4 days.

Overall, the growth of $SrCuSi_4O_{10}$ and $BaCuSi_4O_{10}$ was possible at temperatures > 350 ˚C and provided a route to larger platelets for $BaCuSi_4O_{10}$.

Concentration Study

We found that the concentration of the reagents also played a role in the final morphology. For $SrCuSi_4O_{10}$, increasing the strontium concentration produced thin platelets (Figure 4.23a) ~ 500 nm in thickness, while increasing the copper three-fold produced thick platelets ~5 µm, as well as unreacted copper oxide (Figure 4.23b). Increasing the silica concentration did not change the morphology from spheres (Figure 4.23c).

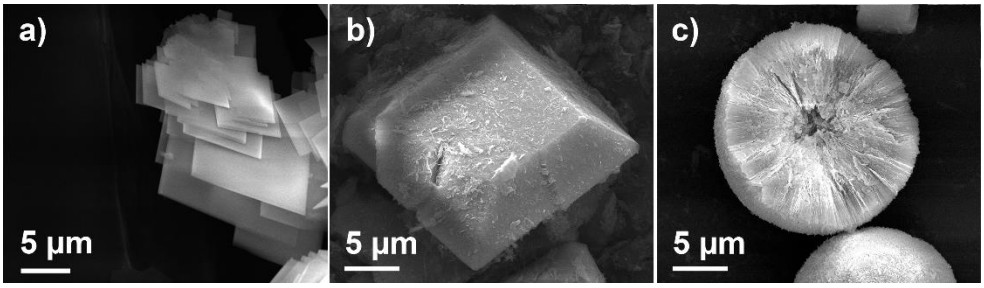

Figure 4.23. Baseline $SrCuSi_4O_{10}$ reaction with a) 3x molar increase in strontium, b) 3x molar increase in copper, and c) 3x molar increase in SiO_2

These results indicate the role that each reagent is playing in the morphology of the final product. Increasing the strontium and the copper shifted the morphology to platelets and away from clusters, however there was a difference in the growth direction. Increasing the strontium concentration increased growth in the [0k0] plane, where increasing the copper concentration increased the growth in [00l] plane. The silica did not have as much effect on which plane was expressed more.

For $BaCuSi_4O_{10}$, we see the opposite trend. Increasing the barium and copper concentration produced the usual collections of small nanocrystals (Figure 4.24a-b). However, increasing the silica concentration produced $CuSiO_3$, where the $BaCuSi_4O_{10}$ can be seen growing off of the surface in platelets (Figure 19c inset).

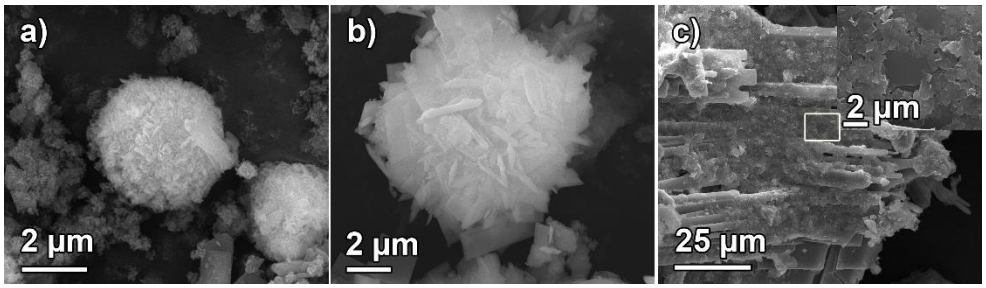

Figure 4.24. Baseline $BaCuSi_4O_{10}$ reaction with a) 3x molar increase in strontium, b) 3x molar increase in copper, and c) 3x molar increase in SiO_2

Reaction order

There has been evidence that the order in which the reagents are added is significant to the final morphology of the product.[16] To test this theory in our system, we changed the reaction order so that instead of adding the mineralizer last, we added the NH_4OH before adding the silica. This would lead to formation of a copper ammonium complex which should be more reactive. However, there was no drastic change in the overall morphology of the product: $SrCuSi_4O_{10}$ formed into spheres with globular shapes on them (Figure 4.25) and $BaCuSi_4O_{10}$ formed into the usual collection of platelets, however the edges were slightly frayed (Figure 4.26).

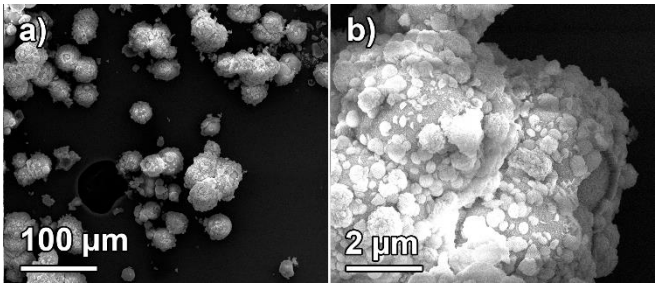

Figure 4.25. SEM images showing the morphology of $SrCuSi_4O_{10}$ after changing the reagent order.

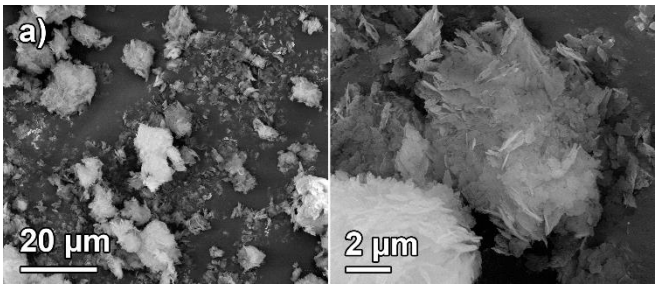

Figure 4.26. SEM images showing the morphology of $BaCuSi_4O_{10}$ after changing the reagent order.

Growth off of Substrates

$CuSiO_3$ was not the only surface that $BaCuSi_4O_{10}$ grew on. We found that $BaCuSi_4O_{10}$ grew off of CuO and Cu_2O substrates. In Figure 4.27, shows the relatively complete coverage of the blue clusters of particles on the surface of the Cu_2O. From the SEM analysis, it appeared that there were two types of growth: the platelets that grew on the smooth top of the Cu_2O surface, and the clusters that formed in volcanos on the rougher sides.

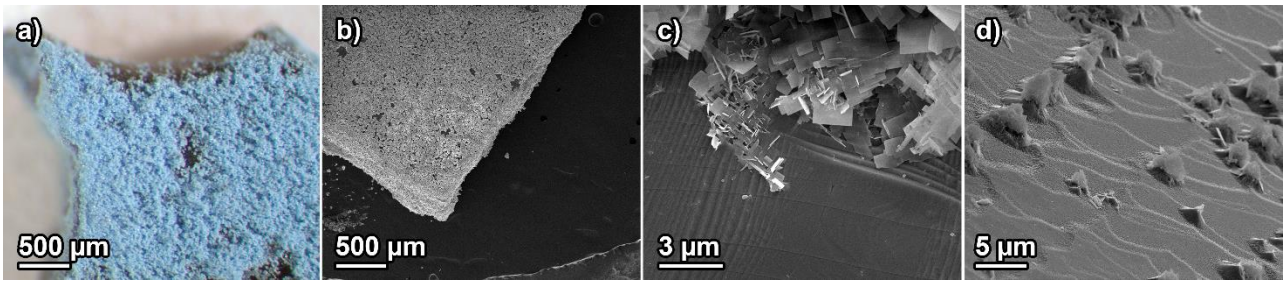

Figure 4.27. Images of $BaCuSi_4O_{10}$ grown on Cu_2O where a-b) are optical and SEM images showing the relatively complete coverage of $BaCuSi_4O_{10}$ on the Cu_2O surface, c-d) are SEM images showing the growth on the top and the side of the Cu_2O surface.

Conclusion

Through hydrothermal synthesis, we have shown that we can control the crystal size and morphology of the $ACuSi_4O_{10}$ series. By varying the precursors, reaction time, and temperature we have grown uniform crystals of $SrCuSi_4O_{10}$ and $BaCuSi_4O_{10}$ on the micro scale with morphologies ranging from flower-like clusters of platelets to nanoscrolls. By varying the

stoichiometry, we controlled the thickness of $SrCuSi_4O_{10}$ crystals; and we formed nanoscrolls of $BaCuSi_4O_{10}$ using potassium silicate with KOH. Additionally, we have found that $BaCuSi_4O_{10}$ grows on the surface of CuO and $CuSiO_3$ in a novel way.

Our hydrothermally synthesized crystals, due to their uniform size and morphology, would be an excellent target for exfoliation into nanosheets for applications that require small, uniform nanocrystals such as biological imaging. Overall, our hydrothermal method would be the first process to control and tune the size and morphology of the $ACuSi_4O_{10}$ series on both a micro and nano scale.

References

1. (a) Berke, H., *Angew. Chem. Int. Ed.* **2002,** *41* (14), 2483-2487; (b) Berke, H., *Chem. Soc. Rev.* **2007,** *36* (1), 15-30.
2. (a) Hentschel, G., *Die Mineralien der Eifelvulkane (Lapis Monographie)*. Wise: 1983; (b) Giester, G.; Rieck, B., *Mineralogical Magazine* **1994,** *58* (393), 663-670; (c) Giester, G.; Rieck, B., *Mineralogical Magazine* **1996,** *60* (402), 795-798.
3. (a) Pozza, G.; Ajò, D.; Chiari, G.; De Zuane, F.; Favaro, M., *Journal of Cultural Heritage* **2000,** *1* (4), 393-398; (b) Verri, G., *Anal. Bioanal. Chem.* **2009,** *394* (4), 1011-1021; (c) Li, Y.-J.; Ye, S.; Wang, C.-H.; Wang, X.-M.; Zhang, Q.-Y., *J. Mater. Chem. C* **2014,** *2* (48), 10395-10402.
4. Johnson-McDaniel, D.; Barrett, C. A.; Sharafi, A.; Salguero, T. T., *J. Am. Chem. Soc.* **2013,** *135* (5), 1677-1679.
5. Chakoumakos, B. C.; Fernandez-Baca, J. A.; Boatner, L. A., *J. Solid State Chem.* **1993,** *103* (1), 105-113.
6. (a) Tite, M. S.; Bimson, M.; Cowell, M. R., *Adv. Chem. Ser.* **1984,** *205* (Archaeol. Chem. 3), 215-42; (b) Warner, T. E., Artificial Cuprorivaite CaCuSi4O10 (Egyptian Blue) by a Salt-Flux Method. In *Synthesis, Properties and Mineralogy of Important Inorganic Materials*, John Wiley & Sons, Ltd: 2011; pp 26-49.
7. (a) Amin, G.; Asif, M. H.; Zainelabdin, A.; Zaman, S.; Nur, O.; Willander, M., *Journal of Nanomaterials* **2011,** *2011*, 9; (b) Xu, Y.; Yang, S.; Zhang, G.; Sun, Y.; Gao, D.; Sun, Y., *Mater. Lett.* **2011,** *65* (12), 1911-1914; (c) Kimijima, T.; Kanie, K.; Nakaya, M.; Muramatsu, A., *Crystengcomm* **2014,** *16* (25), 5591-5597.
8. Byrappa, K., *Prog. Cryst. Growth Charact. Mater.* **2007,** *53* (2), 117-166.

9. Chen, Y.; Shang, M. Y.; Wu, X. F.; Feng, S. H., *Crystengcomm* **2014,** *16* (24), 5418-5423.

10. Johnson-McDaniel, D.; Comer, S.; Kolis, J. W.; Salguero, T. T., *Chemistry – A European Journal* **2015,** *21* (49), 17560-17564.

11. YIN Yong-kui, X. Y.-L., LI Ying, REN Feng-yun, LI Shuang-jing, JIN Ge, LI Miao-jing, CUI Xin-yu, *CHEMICAL RESEARCH IN CHINESE UNIVERSITIES* **2013,** *29* (2), 379-383.

12. Johnson-McDaniel, D. S., T.T., *Journal of Visual Experiments* **2013**.

13. Harker, J. D. H. D. a. D., *Am. Mineral.* **1937,** *22*, 446-467.

14. (a) Zhang, L.; Yu, J. C.; Xu, A.-W.; Li, Q.; Kwong, K. W.; Wu, L., *Chem. Commun.* **2003,** (23), 2910-2911; (b) Wang, Y.; Zhang, S.; Wei, K.; Zhao, N.; Chen, J.; Wang, X., *Mater. Lett.* **2006,** *60* (12), 1484-1487; (c) Shi, S.; Cao, M.; He, X.; Xie, H., *Crystal Growth & Design* **2007,** *7* (9), 1893-1897.

15. (a) Dove, P. M.; Han, N.; De Yoreo, J. J., *Proceedings of the National Academy of Sciences* **2005,** *102* (43), 15357-15362; (b) Kowacz, M.; Prieto, M.; Putnis, A., *Geochim. Cosmochim. Acta* **2010,** *74* (2), 469-481.

16. Jiang, Q.; Shi, Q.; Xu, H.; Li, J.; Dong, J., *Eur. J. Inorg. Chem.* **2011,** (13), 2112-2117.

CHAPTER 5

EXFOLIATION OF THE METAL COPPER TETRASILICATE SERIES

Darrah Johnson-McDaniel and Tina T. Salguero. To be submitted to *Chemical Reviews*.

Abstract

The metal copper tetrasilicate series ($ACuSi_4O_{10}$), which serves as the inorganic basis for several historically relevant blue pigments, can be chemically exfoliated into nanosheets using the novel, yet simple, process of hot water plus agitation over a period of two weeks. The nanosheets are freestanding and comprised of mono-to-few layers with lateral dimensions ranging from a hundred nanometers up to a few microns. Although the exfoliation process *can* take place at room temperature, the time scale required is far longer, on the order of months. Additionally, and fortuitously for our purposes, the exfoliated $ACuSi_4O_{10}$ series retains the strong emission in the near infrared of the bulk material. Capitalizing on this phenomenon, we have solution processed the nanosheets into inks for inkjet printing and spray coating. The nanosheets have been used to form a macroscopic paper. Additionally, we have demonstrated that one can use the nanosheets as a biological imaging agent that shows similar luminescence to quantum dots.

Introduction

The 2010 Nobel Prize in Physics was awarded to Andre Geim and Konstantin Novoselov for the discovery of graphene which sparked increased interest in two-dimensional materials.[1] Nanosheets, which belong to this class, are essentially two-dimensional crystals; and thus can have excellent thermal stability and tribological properties.[2] Additionally, the decrease in thickness of the crystals can lead to enhanced properties such as capacitance[3] or luminescence[4]. While the literature does not provide a precise definition of the dimensions a material should have in order to be considered a nanosheet, for our purposes here, a nanosheet is defined as a material that has one dimension which is <10 nm, with the other two ranging from anywhere from hundreds of nanometers up to microns. Nanosheets can either be freestanding or attached to a surface. One of the major advantages of freestanding nanosheets, is that unlike attached two-dimensional materials created by methods such as chemical vapor deposition or the scotch tape method, freestanding nanosheets can be suspended colloidally and can then be easily processed for spin coating, dip coating, printing, and stamping.[5]

As previously stated, the metal copper tetrasilicate series, $ACuSi_4O_{10}$, has a layered structure where the cation can either be calcium, strontium, or barium.[6] The copper is in square planer coordination which causes strong emission in the near infrared region (NIR) of the electromagnetic spectrum.[7] The strong NIR emission makes this series a promising candidate for applications such as biological imaging or sensing. Producing nanostructured $ACuSi_4O_{10}$ samples greatly enhances the potential for such applications. To that end, we are interested in creating isolable nanosheets of the metal copper tetrasilicate series in order to harness the NIR emission of the materials for luminescent inks, as well as for use as a potential biological imaging agent.

Generally, methods for creating nanoscale materials can be classified as either top-down or bottom up approaches. Top-down approaches usually consist of delaminating or exfoliating a bulk material into nanosheets.[2a, 5b] Bottom up approaches include, but are not limited to, self-assembly[8] and templating.[9] For this paper, however, we are only interested in exfoliation methods. Common exfoliation methods for layered materials can be physical, such as the scotch tape method, or chemical, such as ion intercalation methods. The scotch tape method, first pioneered by Andre Geim and Konstantin Novoselov in 2004 for the exfoliation of graphite, is a physical delamination method that is incredibly useful for van der Waals' materials.[2a] However, the scotch tape method is only applicable for materials that have layers that are loosely bound together which, unfortunately, rules out this method for a wide variety of materials. Other methods primarily established for van der Waals' materials are chemical exfoliation using intercalation with solvated electron liquid ammonia[10] and using ultrasonication with coordinating solvents[11]. Materials that have more complicated bonding, i.e. perovskite materials or layered minerals, usually require different methods for exfoliation, such as ion intercalation, where typically a bulky organic molecule is intercalated into the structure and used to force the layers apart.[12]

The organic ion intercalation method was not successful for exfoliating the $ACuSi_4O_{10}$ series, potentially due to a lack of driving force for the intercalation of bulky organic molecules. Because, unlike metal dichalcogenides or layered minerals such as kaolinite, the $ACuSi_4O_{10}$ series is not held together by van der Waals' forces or hydrogen bonding. The exfoliation method developed by Coleman and coworkers, which uses ultrasonication in coordinating organic solvents, on the other hand, was somewhat effective for delaminating the $ACuSi_4O_{10}$ series. As demonstrated in this work, however, this method has the disadvantages of using high power

ultrasonication, which can lead to fragmentation of the nanosheets, as well toxic organic solvents. To address these issues, we have developed a simple and non-toxic method for exfoliating the metal copper tetrasilicate series using hot aqueous conditions with agitation.[13] Our method produces freestanding nanosheets of mono-to-few layers with lateral dimensions on the micron scale.

Experimental

Exfoliation of the $ACuSi_4O_{10}$ series with organic solvents: 75 mg of the $ACuSi_4O_{10}$ crystals were dispersed in 10 mL of *N*-methyl-2-pyrrolidone (NMP) and then ultrasonicated at 50 power for 1 hour. The resulting suspension was allowed to settle overnight, and the nanosheets were isolated from the supernatant by centrifugation.

Exfoliation of the $ACuSi_4O_{10}$ series with hot water and agitation: 0.5 g (1.33 mmol) of $CaCuSi_4O_{10}$ crystals were dispersed in 30 mL of deionized water and stirred at 80 °C for a period of two weeks. This process produced a light blue dispersion with pearlescent distortions. The nanosheets were then isolated from the supernatant by centrifugation and either re-suspended in water with bath sonication or dried into a light blue powder using vacuum filtration with a 0.4 μm pore size Millipore microcellulose membrane filter. The other members of the $ACuSi_4O_{10}$ series were exfoliated using the same method.

Annealing Experiment: The $CaCuSi_4O_{10}$ nanosheets were annealed at 900 °C for 12 hours in a platinum crucible in the atmosphere and returned to the bright blue color of the bulk material.

Solution processing: For the inkjet printing, a ~3 mg/mL dispersion of $CaCuSi_4O_{10}$ dispersed in N-methyl-pyrrolidone was used as the ‘ink’, and then 5 layers of the nanosheets were printed onto ITO coated glass in a pattern of squares using a Dimatix Materials Printer. For the spray

coating, 10 mL of a 1.0 mM solution of $ACuSi_4O_{10}$ nanosheets in DI water was sprayed onto watercolor paper in a single coat using an Iwata HP-BC1 Plus air brush. The paper was taped to the table to minimize paper warping and allowed to dry in air overnight.

Biological Imaging Trial: A 1 mg/mL solution of $CaCuSi_4O_{10}$ nanosheets was placed in a glass vial. A solution of CdTe quantum dots of the same concentration was used as a luminescence reference. Thin sliced pork was purchased from Publix. Both samples were placed under pork slices with thicknesses ranging from 0.5-1.3 cm. The two samples were then irradiated using a red LED and imaged using a modified Xnite Nikon D3000 camera with Nikkor 18-200 mm lens and Xnite 830 filter. The brightness of the emission was measured using Photoshop CS5.

Characterization: The identity of the exfoliated nanosheet pigments was confirmed using a Bruker D8-Advance powder X-ray diffractometer (Co-Kα radiation source) operated at 40 mA and 40 kV. The PXRD patterns were recorded in the 2θ range of 10−70° with a scanning rate of 0.1 sec $step^{-1}$. The morphology of the exfoliated nanosheets was examined using a FEI Technai 20 (200 keV) transmission electron microscope (TEM) with selected area electron diffraction (SAED) capability and by a FEI Inspect F field emission gun scanning electron microscope (SEM) operated at 20 keV. The samples were prepared for SEM by sprinkling the powders on carbon sticky tape and then coating with gold. The height of the samples was determined using a Bruker Innova atomic force microscope (AFM) in tapping mode. The samples were prepared for AFM by dipping a clean silicon wafer into a dilute solution of the exfoliated nanosheets for ~30 seconds. Photoluminescence spectroscopy was carried out on powder samples using a Horiba FluoroLog-3 equipped with an additional DSS-IGA020L detector for NIR light measurements. For the IR imaging, the samples were first irradiated with a red LED and imaged using a modified Xnite Nikon D3000 camera with Nikkor 18-200 mm lens and Xnite 830 filter.

Results and Discussion

Exfoliation of the $ACuSi_4O_{10}$ Series

The $ACuSi_4O_{10}$ series was first exfoliated using a modified version of the Coleman method. This method produced nanosheets that had large lateral dimensions, but appeared to be slightly fragmented, as shown by transmission electron microscopy (TEM) analysis (Figure 5.1).

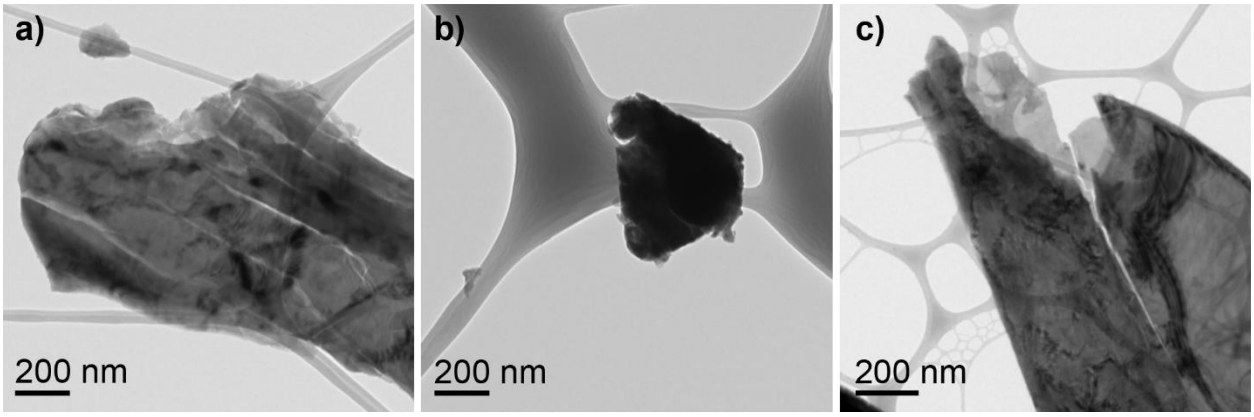

Figure 5.1. TEM images showing the morphology of the $ACuSi_4O_{10}$ series exfoliated using NMP and ultrasonication a) $CaCuSi_4O_{10}$, b) $SrCuSiO_{10}$, and c) $BaCuSi_4O_{10}$

Again, the Coleman method is ideal for materials that exfoliate quite easily due to their van der Waals bonding, but the $ACuSi_4O_{10}$ series does not have van der Waals bonding, and appeared to be more delaminated than exfoliated using this method. The force of the ultrasonication appeared to be the source of the damage, producing fragmentary nanoplatelets rather than nanosheets. The damage was especially noticeable in the case of $SrCuSi_4O_{10}$, where the exfoliated product was small and fragmented (Figure 5.1b).

Therefore, we developed a simpler and gentler method for exfoliating the $ACuSi_4O_{10}$ series. We heated $ACuSi_4O_{10}$ crystals dispersed in deionized water at 80 °C with constant stirring (Figure 5.2). An exfoliation period of two weeks produces a light blue dispersion with pearlescent distortions.

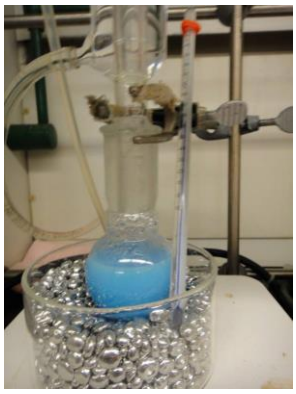

Figure 5.2. Photograph of the $ACuSi_4O_{10}$ exfoliation set-up.

Afterward, the nanosheets were isolated from the bulk material by centrifugation and were then either re-suspended in water or dried into a compact powder by vacuum filtration. The resulting dried nanosheets had a light blue color and a fluffy texture (Figure 5.3).

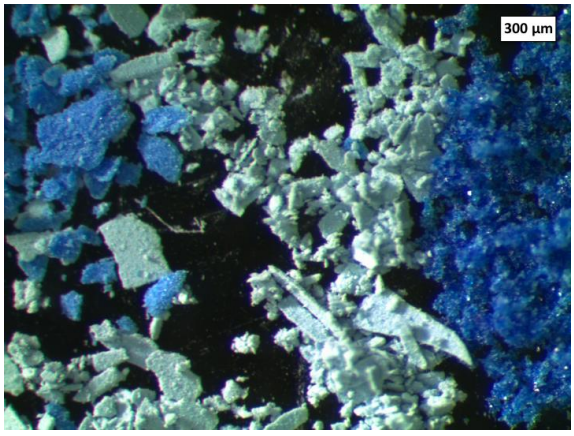

Figure 5.3. Optical image illustrating the dichromaticism of $CaCuSi_4O_{10}$. From left to right: bright blue annealed $CaCuSi_4O_{10}$ nanosheets, light blue exfoliated $CaCuSi_4O_{10}$, and bright blue bulk $CaCuSi_4O_{10}$. Reprinted with permission from *J. Am. Chem. Soc.* **2013,** *135* (5), 1677-1679 (SI). Copyright 2013 American Chemical Society.

The $CaCuSi_4O_{10}$ nanosheets were then annealed at 900 °C for 12 hours in atmosphere which returned them to the bright blue color of the bulk material (Figure 5.3). The color change was consistent with the dichromatic nature of $CaCuSi_4O_{10}$, where the hue of the material changes with both concentration and crystal thickness; that is, larger crystals produce deeper, more vivid

blues.[14] The other members of the $ACuSi_4O_{10}$ series were exfoliated and characterized in the same manner and all produced similar light blue colloidal dispersions, which could be either kept suspended or isolated as powders by vacuum filtration. We confirmed the identity of the exfoliated and annealed products using powder X-ray diffraction (PXRD) (Figure 5.4.)

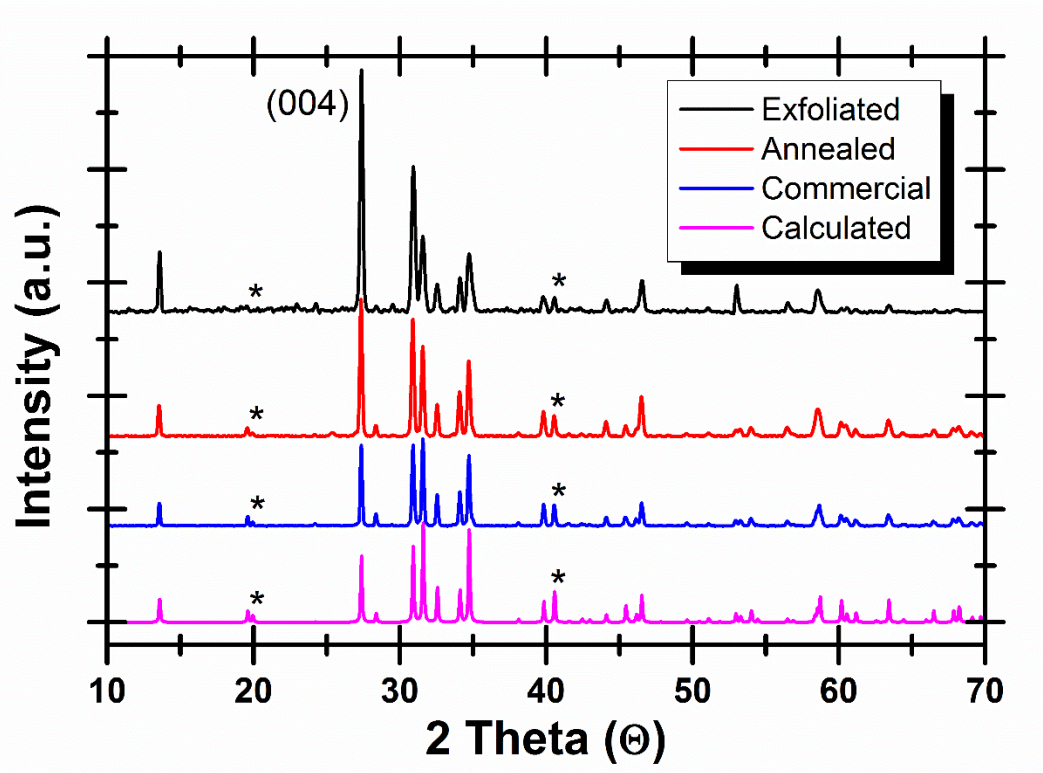

Figure 5.4. PXRD data for exfoliated $CaCuSi_4O_{10}$ nanosheets, recrystallized nanosheets, and commercial Egyptian blue, and the calculated pattern. The asterisks (*) denote the decreased intensity of the {*hk*0} series in the exfoliated products as compared to the rest of the patterns. Reprinted with permission from *J. Am. Chem. Soc.* **2013,** *135* (5), 1677-1679. Copyright 2013 American Chemical Society.

The powder diffraction pattern for the $CaCuSi_4O_{10}$ nanosheets matched the reference pattern for $CaCuSi_4O_{10}$. The exfoliated $CaCuSi_4O_{10}$ showed an orientation effect where the intensity of the {00*l*} series was increased when compared to the rest of the {*hk*0} reflections. Here, the orientation effect is indicative of the material being two-dimensional because the {00*l*} series is the layer plane in the crystal structure. After the nanosheets were annealed, they

regained their three-dimensional structure, which was confirmed both by the resurgence of the bright blue color as well as the increase in intensity of the {*hk*0} reflections. The nanosheets produced from the other members of the $ACuSi_4O_{10}$ also matched their corresponding reference patterns, and they all showed the same orientation effect where the intensity of the {00*l*} series was increased when compared to the rest of the {*hk*0} reflections (Figure 5.5).

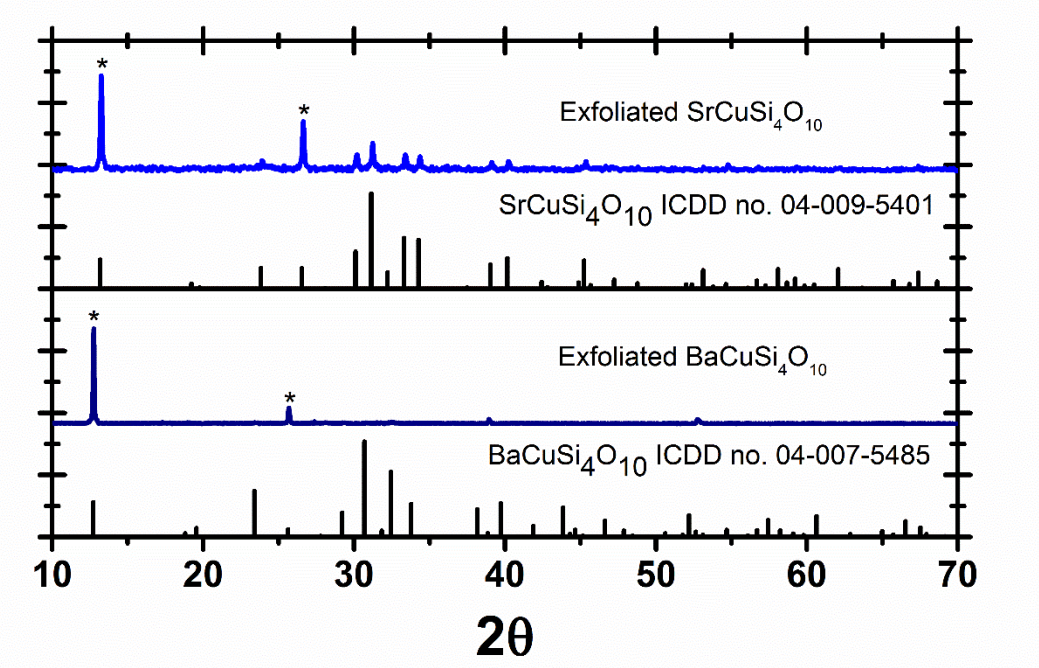

Figure 5.5. PXRD patterns for $SrCuSi_4O_{10}$ and $BaCuSi_4O_{10}$ nanosheets with matching reference patterns from the International Center for Diffraction Data (ICDD). The asterisks denote the increased intensity of the {00*l*} reflections.

We examined the morphology of the $CaCuSi_4O_{10}$ nanosheets using TEM and atomic force microscopy (AFM). The nanosheets were highly crystalline with crisp, clean edges and with lateral dimensions ranging from hundreds of nanometers up to microns (Figure 5.6a). The selected area electron diffraction pattern (Figure 5.6a inset) matched the tetragonal crystal structure of $CaCuSi_4O_{10}$ and was indexed to the (200) and (020) reflections. We also determined

that the zone axis was [002], confirming that the nanosheets were exfoliated along the {00*l*} plane. The height of the nanosheets was determined to be ~1.2 nm using AFM (Figure 5.6b). The theoretical thickness of a monolayer of $CaCuSi_4O_{10}$ is 0.87 nm. However, we propose that there are hydration layers present on the surface of the nanosheet, which accounts for this increase in height.

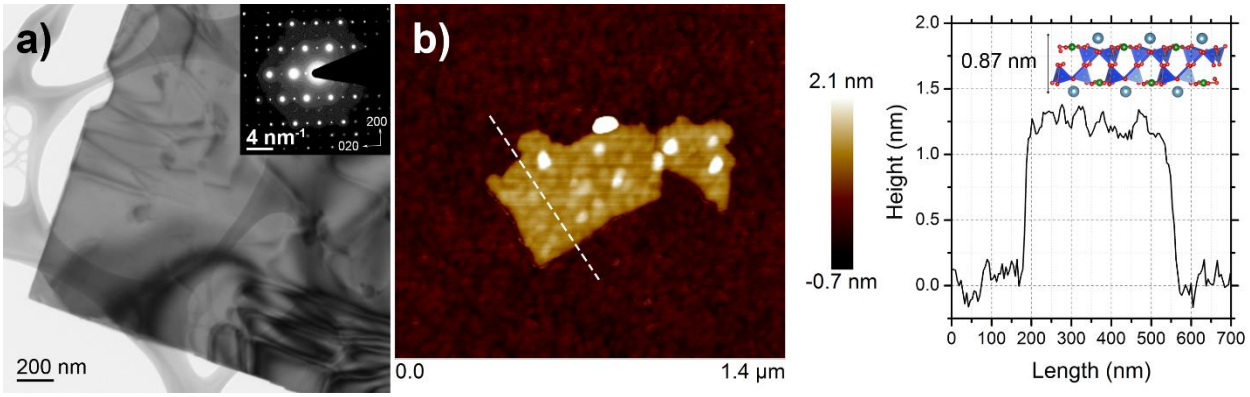

Figure 5.6. Morphology of exfoliated $CaCuSi_4O_{10}$. a) TEM which shows that the lateral dimensions of the nanosheets are on the micron scale. The inset shows the SAED image. b) Topographic AFM image (left) and height profile of the nanosheet (right). Inset shows the side view of the structure of a monolayer of $CaCuSi_4O_{10}$. Adapted with permission from *J. Am. Chem. Soc.* **2013,** *135* (5), 1677-1679. Copyright 2013 American Chemical Society.

All the nanosheets of the $ACuSi_4O_{10}$ series were similar in morphology: they had lateral dimensions ranging from hundreds of nanometers up to microns and long, straight edges (Figure 5.7).

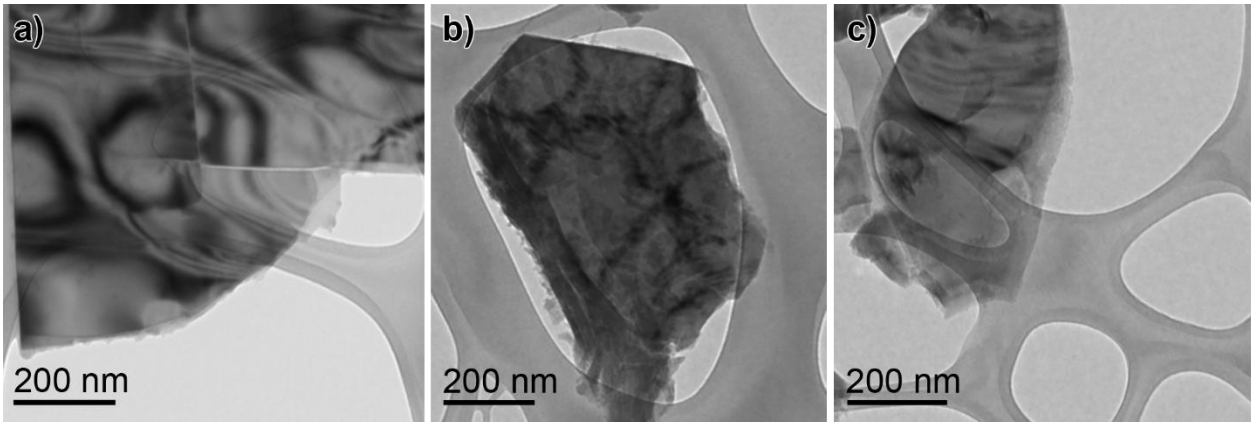

Figure 5.7. TEM images showing the similar morphology of the $ACuSi_4O_{10}$ series exfoliated using hot water and agitation a) $CaCuSi_4O_{10}$, b) $SrCuSiO_{10}$, and c) $BaCuSi_4O_{10}$. Adapted with permission from *MRS Proceedings*, **2014**, *1618*, 161-166. Copyright 2014 Materials Research Society.

The size of the $ACuSi_4O_{10}$ nanosheets directly corresponded to the initial morphology and size of the starting material. Larger crystals produced larger nanosheets: as seen in Figure 5.8 where the nanosheets exfoliated from crystals formed from a melt flux route were noticeably larger than those exfoliated from crystals formed using a solid state route. This size dependence has been previously observed for the exfoliation of layered perovskite crystals into nanosheets.[5b, 12b]

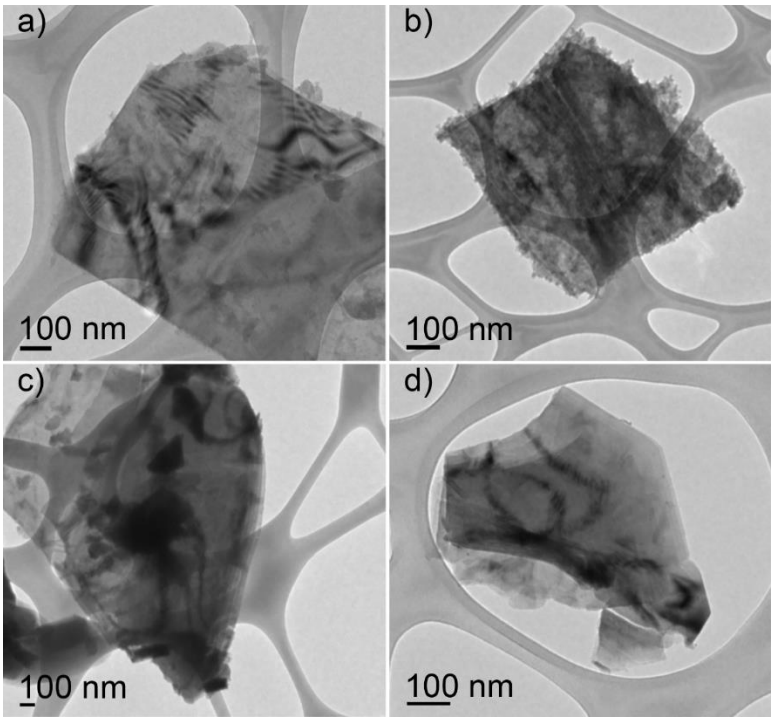

Figure 5.8. TEM images showing the size dependence of the exfoliation process. a) $CaCuSi_4O_{10}$ exfoliated from crystals formed using a melt flux route, b) a) $CaCuSi_4O_{10}$ exfoliated from crystals formed using a solid state route, c) $BaCuSi_4O_{10}$ exfoliated from crystals formed using a melt flux route, and d) $BaCuSi_4O_{10}$ exfoliated from crystals formed using a solid state route. Reprinted with permission from *J. Vis. Exp.* **2014, *86*, e51686**. Copyright 2014 Journal of Visual Experiments.

Indeed, this size dependence was the most notable and useful when hydrothermally synthesized $BaCuSi_4O_{10}$ (detailed in Chapter IV) was used as an exfoliation precursor. The resulting exfoliated product was on a much smaller scale than the other nanosheets obtained using melt flux or even solid state precursors, producing uniform rectangular nanocrystals that had lateral dimensions of 50-200 nm and monolayer thickness (Figure 5.9).

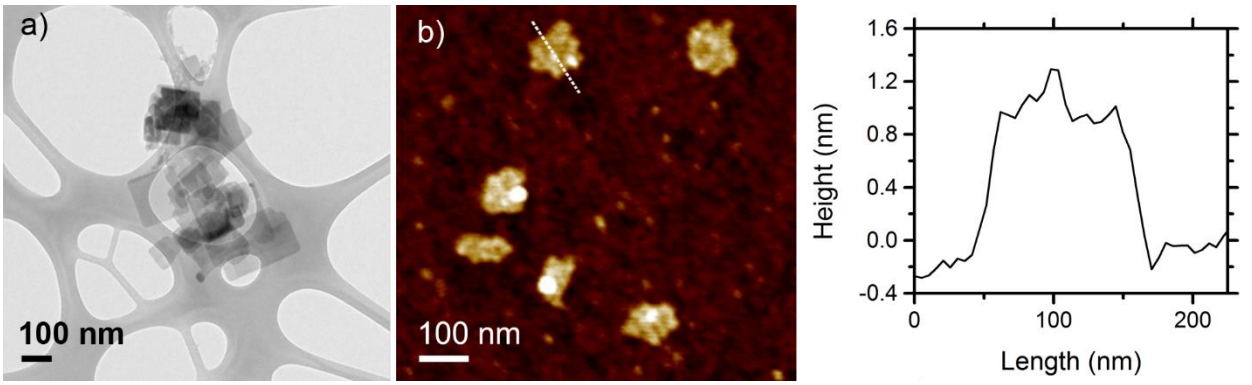

Figure 5.9. Morphology of the exfoliated hydrothermally synthesized $BaCuSi_4O_{10}$ by a) TEM and b) topographic AFM image (left) and height profile of the nanocrystal (right).

The rectangular morphology was unique to the hydrothermally synthesized $BaCuSi_4O_{10}$ crystals and none of the other synthetic methods produced as uniform crystals. The ability to control the size of the nanosheet product is useful for applications, such as biological imaging, that require small, uniform nanocrystals.

Temperature Study of the Exfoliation Process

In order to further understand how the exfoliation process takes place, we carried out a temperature study of the exfoliation of $CaCuSiO_{10}$. Using the standard procedure for exfoliating $CaCuSi_4O_{10}$, we sealed the reaction in a Schlenk vessel, and then stirred at room temperature for an extended period of time. The exfoliation of $CaCuSi_4O_{10}$ did occur in aqueous conditions at room temperature. However, instead of the usual two weeks, the exfoliation process was much slower—six months. And even on that timescale, the nanosheets produced are not as thin as the ones exfoliated using 80 °C water, as seen in Figure 5.10 where the nanosheets are ~5 nm in thickness, indicating that agitation alone does not create enough energy to completely separate the layers.

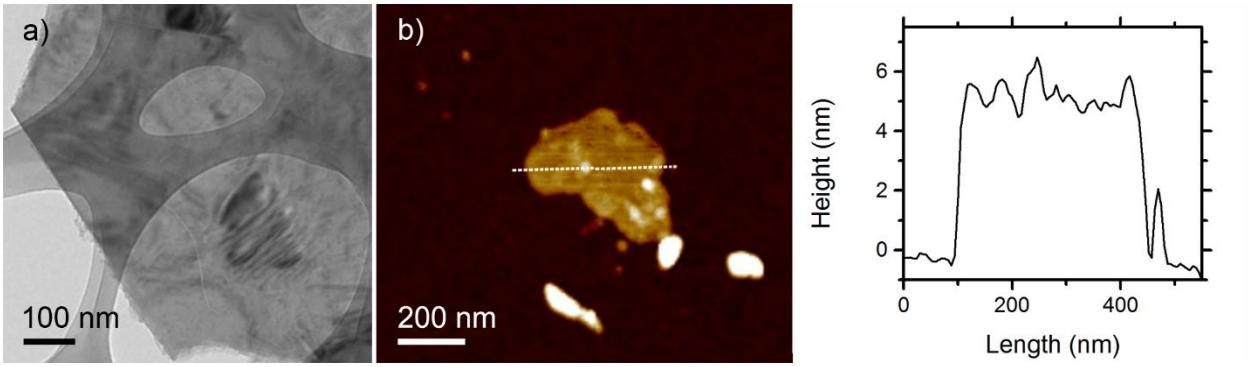

Figure 5.10. Morphology of the room temperature exfoliated $CaCuSi_4O_{10}$ by a) TEM and b) topographic AFM image (left) and height profile of the nanosheet (right).

Historical Exfoliation

Based on the results of the above temperature study, we hypothesized that historical samples of Egyptian blue might have undergone a similar delamination effect if the exposed surface had come into any contact with water over the years; because, as previously demonstrated, $CaCuSi_4O_{10}$ did delaminate without added heat over long time scales. To test our hypothesis, we obtained two archeological specimens of Egyptian blue which had been in drastically different environments. The first was a sediment sample from a post-Roman stratigraphy layer in Leicester, UK that contained a few grains of Egyptian blue. The sample had been in moist, acidic soil for at least 500 years.[15] The second was a sample loaned from the Carlos museum at Emory University taken from an Egyptian coffin which had been in hot, dry conditions for the bulk of its history. For the Leicester sample, we first had to physically separate an Egyptian blue crystal from the rest of the sample, as shown in Figure 5.11a where a bright blue crystal is visible in the optical image intermingled with other sediment crystals.

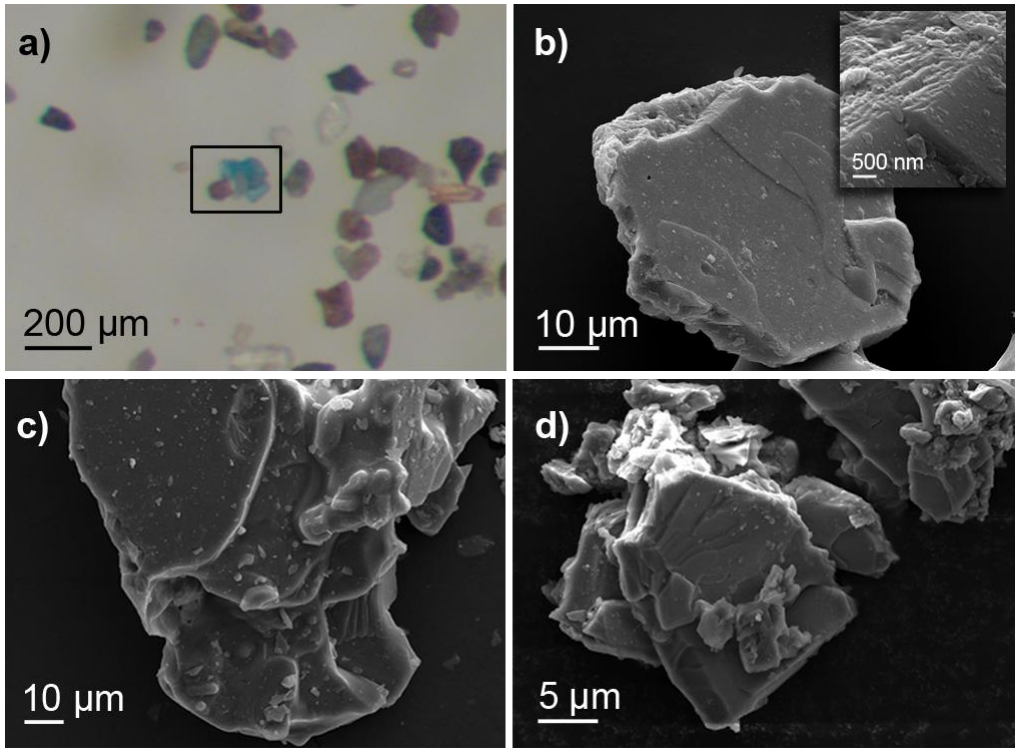

Figure 5.11. (a) Optical image of the Leicester sample, with a Egyptian blue crystal in the central box, (b) SEM image of the crystal identified in the optical image, with the insert showing a magnified view of the top left crystal edge, (c) SEM image of commercial Egyptian blue, and (d) SEM image of the sample of Egyptian blue taken from the Egyptian coffin. Reprinted with permission from *MRS Proceedings*, **2014**, *1618*, 161-166. Copyright 2014 Materials Research Society.

We then examined both of the archeological samples by SEM, along with a commercial sample of $CaCuSi_4O_{10}$ for comparison. As shown in Figure 5.11, there were platelets present in all of the samples which clearly showed the steps, ridges, and terraces that are common features of layered materials that can physically cleave along the layer planes. However, we did not see any signs of chemical exfoliation, such as detached sheets, on either of the archeological samples. Even the Leicester sample, which we had hypothesized would have been the likeliest candidate for exfoliation because it had been exposed to damp conditions for years, did not show any of the expected signs of chemical delamination. Indeed, all the samples were very similar in comparison. Therefore, we cannot definitively say if any chemical exfoliation occurred over the

millennia. On the other hand, since we were working from an extremely limited number of samples, and only one of them had been exposed to damp conditions over a long period of time, neither can we categorically rule out the possibility of such naturally occurring historical exfoliation.

Photoluminescence Spectroscopy and Near Infrared Imaging

As previously stated, the $ACuSi_4O_{10}$ series strongly luminesces in the NIR when excited with light in the visible range. In order to see if our nanosheet product maintained the luminescence of the bulk pigment, we performed photoluminescence spectroscopy and near IR imaging on our exfoliated $CaCuSi_4O_{10}$. The $CaCuSi_4O_{10}$ nanosheets produced a slightly asymmetrical curve centered at ~910 nm that corresponds to the B_{2g}-B_{1g} transition, which was a very similar emission profile compared to that of the bulk material (Figure 5.12). The annealed nanosheets also had a similar emission peak. The observed emission wavelength for both the exfoliated and bulk $CaCuSi_4O_{10}$ was lower than the 950 nm which had been previously reported by Pozza and coworkers.[7b] However, the reported emission values for the $ACuSi_4O_{10}$ series are not exact over the series and can vary by tens of nanometers.[16]

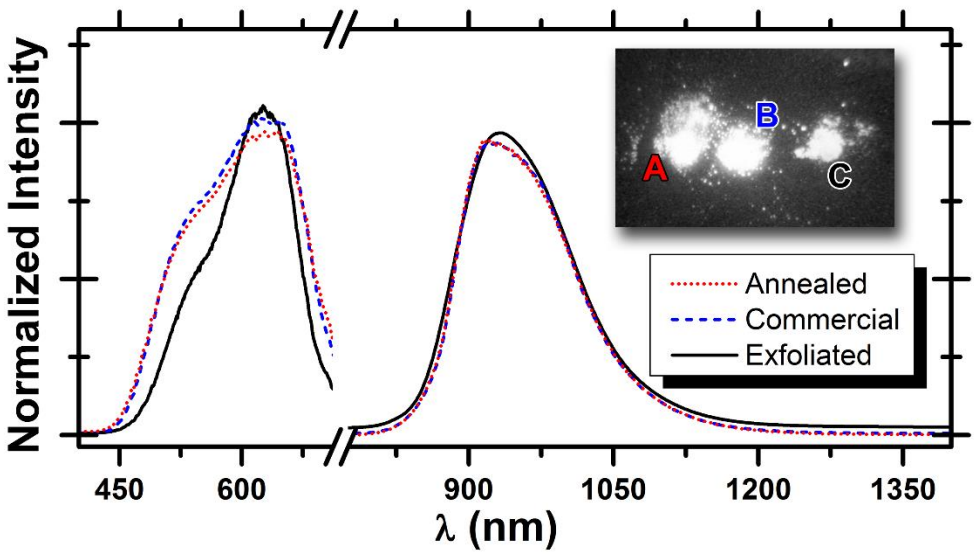

Figure 5.12. Excitation and emission spectra of powder samples of commercial Egyptian blue (Kremer Pigment), exfoliated $CaCuSi_4O_{10}$ nanosheets, and recrystallized (annealed) nanosheets. The inset shows a near IR image of the three powder samples. Reprinted with permission from *J. Am. Chem. Soc.* **2013,** *135* (5), 1677-1679. Copyright 2013 American Chemical Society.

For the excitation profile, there was a difference in the spectrum for the exfoliated sample compared to the commercial sample. The feature on the excitation curve at 540 nm that corresponds to the B_{1g}-A_{1g} transition was slightly reduced for the exfoliated sample. This is not surprising because, in D_{4h} symmetry, the B_{1g}-A_{1g} transition is caused by vibronic coupling between the layers, and therefore we would expect the intensity for this transition to be less as the material essentially goes from three to two dimensions. After annealing, the nanosheets revert to a three-dimensional structure and therefore the excitation profile was nearly the same as that of the bulk. Using NIR imaging, we observed bright luminescence from all the samples (Figure 5.12 inset).

Examining the photoluminescence of the other members of the $ACuSi_4O_{10}$ series, we again see the preservation of luminescence for the exfoliated product (Figure 5.13).

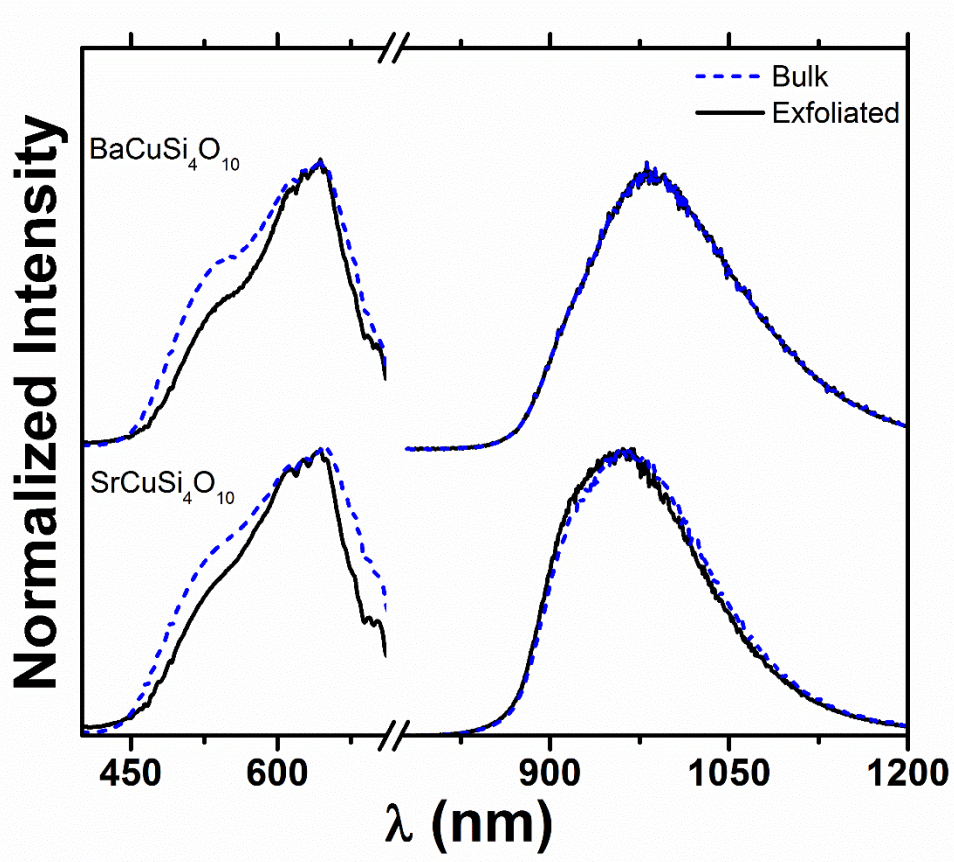

Figure 5.13. Excitation and emission spectra of powder samples of bulk and exfoliated $SrCuSi_4O_{10}$ and $BaCuSi_4O_{10}$.

The wavelength of emission was red-shifted with increasing cation size for the other members of the $ACuSi_4O_{10}$ series, $SrCuSi_4O_{10}$ had an emission peak at 960 nm and $BaCuSi_4O_{10}$ emitted at 980 nm, but the basic shape of the emission profile remained the same. Again, we observed the reduction in the intensity of the B_{1g}-A_{1g} transition in the excitation profile for the exfoliated samples as compared to the bulk. The overall retention of luminescence makes the $ACuSi_4O_{10}$ nanosheets excellent candidates for sensors or biological imaging beacons.

Solution Processing

By making the $ACuSi_4O_{10}$ series nanostructured, we have opened up new avenues for applications, some of which can be realized through solution processing, such as security inks. We can process the colloidal dispersions of the $ACuSi_4O_{10}$ in various ways, including inkjet printing and spray coating. (Figure 5.14). Using a dilute solution of the nanosheets, we printed a pattern of squares on an ITO coated glass slide using a materials printer. The printed nanosheets still luminesced in the NIR, proving they could be used as a luminescent ink (Figure 5.14a). Additionally, we can use our nanosheet ink with a spray coater and templates to make various luminescent images on paper, as demonstrated in Figure 5.14b with the photoluminescent Georgia Bulldog.

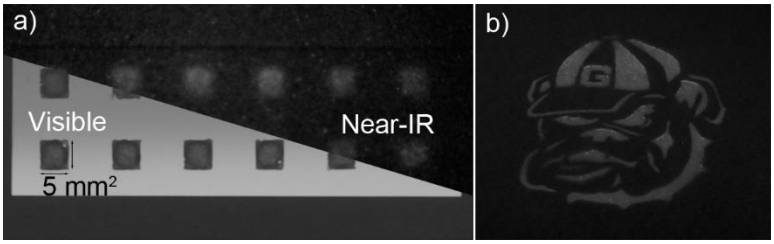

Figure 5.14. Solution processing images a) visible and IR photographs of the inkjet printed squares and b) IR photograph of the spray coated bulldog. Adapted with permission from *J. Am. Chem. Soc.* **2013,** *135* (5), 1677-1679. Copyright 2013 American Chemical Society.

Work carried out by R. Weimar turned our $CaCuSi_4O_{10}$ nanosheets into a millimeter size macrostructure by creating a paper from them (Figure 5.15).[17] A colloidal suspension of the nanosheets was filtered onto a membrane filter. The resulting macrostructure was a light blue color and was fragile and easily fractured (Figure 5.15a). SEM showed that the nanosheets were stacking to form a lamellar structure (Figure 5.15b). After annealing, as seen in Figure 5.15c, the nanosheet paper turned from a light blue to a darker blue crystal, again indicating that a bulk structure was formed.

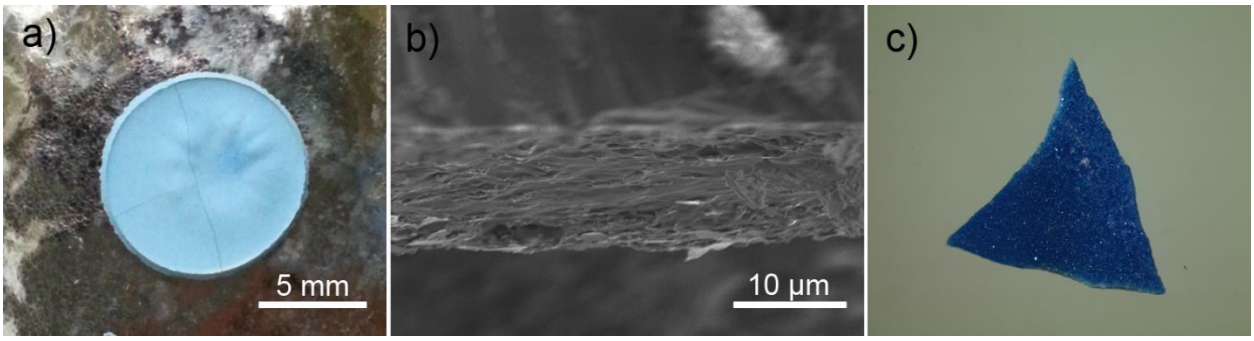

Figure 5.15. a) Photograph of a freestanding paper of $CaCuSi_4O_{10}$ nanosheets, (b) a side-on view of the paper by SEM revealing the lamellar structure, and (c) an annealed piece of $CaCuSi_4O_{10}$ nanosheet paper showing the change to darker blue. Reprinted with permission from *MRS Proceedings*, **2014**, *1618*, 161-166. Copyright 2014 Materials Research Society.

Biological Imaging

Tissue penetration is the best between 650-1450 nm, therefore materials that emit at long wavelengths and in the NIR are attractive candidates for biological imaging agents.[18] As the $ACuSi_4O_{10}$ series emits firmly in that window, that makes them interesting candidates for biological imaging. As a proof of concept test, we measured the emission of a 1 mg/mL solution of $CaCuSi_4O_{10}$ nanosheets through pork slices of varying thickness. The emission was visible up through 1.1 cm of pork, which is the approximate thickness of skin (Figure 5.16a). We also compared the emission of the $CaCuSi_4O_{10}$ nanosheets through the pork to CdSe quantum dots, and the emission levels were similar.

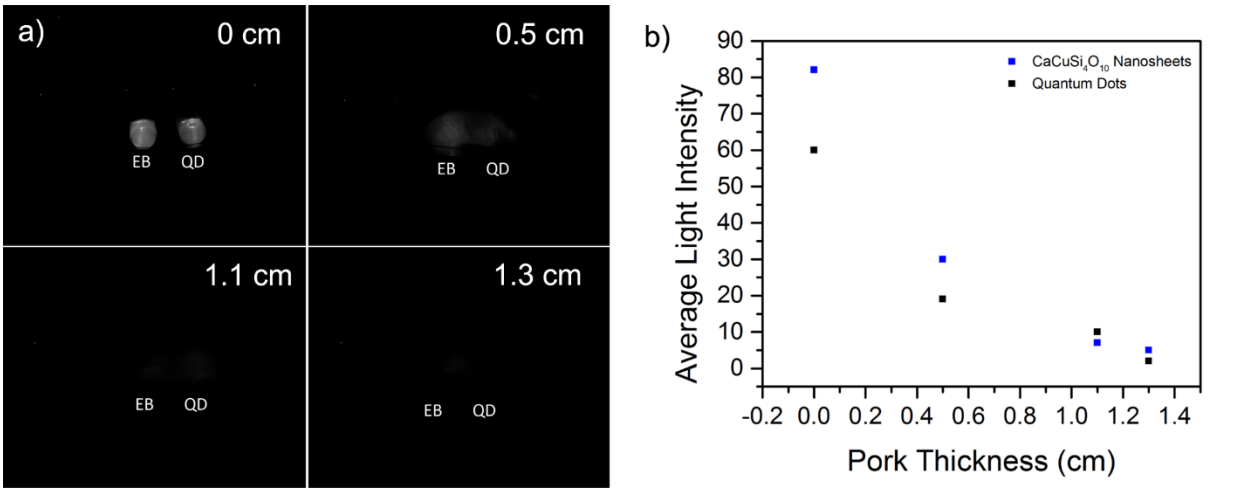

Figure 5.16. Biological imaging proof of concept test with $CaCuSi_4O_{10}$ nanosheets a) IR image of the emission from both the $CaCuSi_4O_{10}$ nanosheets (labeled EB) as well as the CdSe quantum dots (labeled QD) and b) plot of the average light intensity calculated from the images.

While the ideal size for a biological imaging agent is largely dependent both on what part of the body is being imaged and the method for introducing it, nanomaterials in the range of 30-400 nm are useful for multiple imaging routes.[18] The current drawback to using our exfoliated $CaCuSi_4O_{10}$ nanosheets as a biological imaging agent is that not all of the nanosheets lie in the target range of 30-400 nm. Indeed, some of the sheets were over a micron in size which could lead to blockage at an injection site.[18] However, future research could overcome this drawback by processing the nanosheets to a smaller, more uniform size or turning to $BaCuSi_4O_{10}$, which is amenable to hydrothermal processing as discussed in Chapter IV.

Conclusion

The metal copper tetrasilicate series can be delaminated using the method developed by Coleman and coworkers of ultrasonication in organic solvents, however this method does not produce pristine nanosheets, but rather fragmentary nanoplatelets. We then developed a safe, gentle, and non-toxic method for exfoliating all the members of the $ACuSi_4O_{10}$ series into

nanosheets using hot water and agitation for a period of two weeks. This facile method produces colloidal suspensions of the nanosheets that can either be kept suspended or dried into powders. We have shown that the resulting freestanding nanosheets are highly crystalline and are, by TEM and AFM analysis, mono-to-few layers with lateral dimensions ranging from a hundred nanometers up to a few microns. The dimensions and morphology are highly dependent on the morphology and dimensions of the starting material.

As we have demonstrated, the $ACuSi_4O_{10}$ series can also be exfoliated at room temperature; however, the time scale is much longer and the nanosheets are not as thin. Despite our hypothesis of archeological samples having undergone a similar delamination process over the years, we found no concrete evidence that occurred. Because our exfoliated nanosheets retain the near infrared emission of the bulk material, they can be solution processed to form luminescent images and be formed into a 'paper'. Additionally, in a preliminary proof of concept test, our $CaCuSi_4O_{10}$ nanosheets showed similar effectiveness as a biological imaging agent to quantum dots. By exfoliating the $ACuSi_4O_{10}$ series, we have brought these fascinating ancient materials into the 21st century, where they have found new life.

References

1. (a) Eda, G.; Yamaguchi, H.; Voiry, D.; Fujita, T.; Chen, M.; Chhowalla, M., *Nano Lett.* **2011,** *11*, 5111-5116; (b) Wang, Q.; O'Hare, D., *Chem. Rev.* **2012,** *112*, 4124-4155; (c) Zhang, G.; Lou, X. W., *Adv. Mater.* **2013,** *25*, 976-979; (d) Yu, J.; Low, J.; Xiao, W.; Zhou, P.; Jaroniec, M., *J. Am. Chem. Soc.* **2014,** *136*, 8839-8842; (e) Rodenas, T.; Luz, I.; Prieto, G.; Seoane, B.; Miro, H.; Corma, A.; Kapteijn, F.; Llabres i Xamena, F. X.; Gascon, J., *Nat. Mater.* **2015,** *14*, 48-55.
2. (a) Novoselov, K. S.; Geim, A. K.; Morozov, S. V.; Jiang, D.; Zhang, Y.; Dubonos, S. V.; Grigorieva, I. V.; Firsov, A. A., *Science* **2004,** *306*, 666-669; (b) Cammarata, A.; Polcar, T., *Inorg. Chem.* **2015,** *54* (12), 5739-5744; (c) Huang, H. D.; Tu, J. P.; Gan, L. P.; Li, C. Z., *Wear* **2006,** *261* (2), 140-144.
3. Zhu, Y.; Cao, C.; Tao, S.; Chu, W.; Wu, Z.; Li, Y., *Sci. Rep.* **2014,** *4*, 5787.
4. Splendiani, A.; Sun, L.; Zhang, Y.; Li, T.; Kim, J.; Chim, C.-Y.; Galli, G.; Wang, F., *Nano Lett.* **2010,** *10*, 1271-1275.
5. (a) Schwartz, R. W. N., Manoj, Chemical Solution Deposition—Basic Principles In *Solution Processing of Inorganic Materials*, Mitzi, D., **2009**, Wiely. (b) Shibata, T.; Takano, H.; Ebina, Y.; Kim, D. S.; Ozawa, T. C.; Akatsuka, K.; Ohnishi, T.; Takada, K.; Kogure, T.; Sasaki, T., *J. Mater. Chem. C* **2014,** *2*, 441-449.
6. Pabst, A., *Acta Crystallogr.* **1959,** *12*, 733-739.
7. (a) Accorsi, G.; Verri, G.; Bolognesi, M.; Armaroli, N.; Clementi, C.; Miliani, C.; Romani, A., *Chem. Commun.* **2009,** *23*, 3392-3394; (b) Pozza, G.; Ajò, D.; Chiari, G.; De Zuane, F.; Favaro, M., *Journal of Cultural Heritage* **2000,** *1*, 393-398.

8. Wang, Z. C.; Li, Z. Y.; Medforth, C. J.; Shelnutt, J. A., *J. Am. Chem. Soc.* **2007,** *129*, 2440-2441.

9. Pope, T. R.; Lassig, M. N.; Neher, G.; Weimar, R. D., III; Salguero, T. T., *J. Mater. Chem. C* **2014,** *2*, 3223-3230.

10. Ding, Z. F.; Bux, S. K.; King, D. J.; Chang, F. L.; Chen, T. H.; Huang, S. C.; Kaner, R. B., *J. Mater. Chem.* **2009,** *19*, 2588-2592.

11. Coleman, J. N.; Lotya, M.; O'Neill, A.; Bergin, S. D.; King, P. J.; Khan, U.; Young, K.; Gaucher, A.; De, S.; Smith, R. J.; Shvets, I. V.; Arora, S. K.; Stanton, G.; Kim, H.-Y.; Lee, K.; Duesberg, G. S.; Hallam, T.; Boland, J. J.; Wang, J. J.; Donegan, J. F.; Grunlan, J. C.; Moriarty, G.; Shmeliov, A.; Nicholls, R. J.; Perkins, J. M.; Grieveson, E. M.; Theuwissen, K.; McComb, D. W.; Nellist, P. D.; Nicolosi, V., *Science* **2011,** *331*, 568-571.

12. (a) Sasaki, T.; Watanabe, M., *J. Am. Chem. Soc.* **1998,** *120*, 4682-4689; (b) Tanaka, T.; Ebina, Y.; Takada, K.; Kurashima, K.; Sasaki, T., *Chem. Mater.* **2003,** *15*, 3564-3568; (c) Xu, F. F.; Ebina, Y.; Bando, Y.; Sasaki, T., *J. Phys. Chem. B* **2003,** *107*, 9638-9645; (d) Chalasani, R.; Gupta, A.; Vasudevan, S., *Sci. Rep.* **2013,** *3*, 3498.

13. (a) Johnson-McDaniel, D.; Barrett, C. A.; Sharafi, A.; Salguero, T. T., *J. Am. Chem. Soc.* **2013,** *135*, 1677-1679; (b) Johnson-McDaniel, D.; Salguero, T. T., *J. Vis. Exp.* **2014,** *86*, e51686.

14. (a) Riederer, J., Egyptian Blue. In *Artists' Pigments: A Handbook of Their History and Characteristics*, FitzHugh, E. W., Ed. **1997**; (b) Eastaugh, N. W., V.; Chaplin, T.; Siddall, R., *The Pigment Compendium: A Dictionary of Historical Pigments*. **2005**, Butterworth-Heinemann: Oxford, U.K.

15. Canti, M. G.; Heathcote, J. L., *J. Archaeol. Sci.* **2002,** *29*, 831-836.

16. (a) Chen, W.; Shi, Y.; Chen, Z.; Sang, X.; Zheng, S.; Liu, X.; Qiu, J., *J. Phys. Chem. C* **2015**, *119*, 20571-20577; (b) Li, Y.-J.; Ye, S.; Wang, C.-H.; Wang, X.-M.; Zhang, Q.-Y., *J. Mater. Chem. C* **2014,** *2*, 10395-10402; (c) Verri, G., *Anal. Bioanal. Chem.* **2009,** *394*, 1011-1021.

17. Salguero, T. T.; Johnson-McDaniel, D.; Barrett, C. A.; Sharafi, A.; Weimar, R.; Blevins, T., *MRS Online Proceedings Libaray*, **2014**, *1618*, 161-166.

18. Pansare, V. J.; Hejazi, S.; Faenza, W. J.; Prud'homme, R. K., *Chem. Mater.* **2012,** *24*, 812-827.

CHAPTER 6

CONCLUSIONS

Conclusions

A ‘good blue’ might have been hard for the ancient people to find, but their efforts in inventing synthetic methods for making $CaCuSi_4O_{10}$ and $BaCuSi_4O_{10}$ have had a major and lasting impact. Not only were these pigments used to color paintings, sculptures, and pottery a brilliant blue for thousands of years[1], and even used as a form of currency in parts of ancient China, but they are also strongly photoluminescent[2] and, therefore, can dazzle the modern world as much as they did the ancient one. The ancient people were remarkable chemists and were able to accurately manufacture $CaCuSi_4O_{10}$ and $BaCuSi_4O_{10}$ using melt-flux synthesis, despite the limitations of rather primitive technology.[1c, 3]

However, the ancient people could not have possibly predicted that we would eventually live in a nano world, or that we would ever want to produce the $ACuSi_4O_{10}$ series on anything but a macro scale. To address that understandable knowledge gap we developed three novel methods for creating the metal copper tetrasilicate series on the micro and nano scale.

Our first method for synthesizing the $ACuSi_4O_{10}$ series on this sub-macro scale was to employ a solid state synthetic method, with the addition of nanoscale precursors. This process created micron-to-sub-micron scale $ACuSi_4O_{10}$ crystals that are more uniform in size and morphology than those created through bulk solid state synthesis. We also successfully lowered the initial reaction temperatures for the $ACuSi_4O_{10}$ series by over 200 °C and were able to create

brighter blues compared to solid state products synthesized with bulk precursors. Additionally, the overall morphology was more uniform compared to synthesis using bulk precursors. $CaCuSi_4O_{10}$ and $SrCuSi_4O_{10}$ formed crystals that had a sub-micron grain size and $BaCuSi_4O_{10}$ formed into sub-micron sized single crystals in the ideal crystal shape for the $ACuSi_4O_{10}$ series.

Hydrothermal synthesis provided the second route to size control, with the added bonus of being able to tune the morphology. While it has long been theorized that the mineralogical forms of the $ACuSi_4O_{10}$ series formed hydrothermally[4], this method has been relatively unexplored synthetically. The hydrothermal synthesis of $CaCuSi_4O_{10}$ was considerably more difficult than that of the heavier members of the series. We found that the temperature of the reaction played an important role: too hot and it formed calcium silicate; too cold and it formed a hydrated calcium copper silicate. The choice of precursor was crucial as well. Indeed, $CaCuSi_4O_{10}$ was only able to be synthesized under very specific conditions. By using nitrate salts, sodium silicate, and ammonium hydroxide and reacting at 350 °C for three days, we were finally able to hydrothermally synthesize uniform micron-sized clusters of $CaCuSi_4O_{10}$ platelets. $SrCuSi_4O_{10}$ and $BaCuSi_4O_{10}$, on the other hand, were much simpler to form via hydrothermal synthesis. We were even able to tune the morphologies of the products from flower-like clusters of platelets to nanoscrolls by varying the precursors, reaction time, and temperature. And through our hydrothermal method, we were able to grow $BaCuSi_4O_{10}$ crystals off the surface of CuO and $CuSiO_3$. Additionally, due to our hydrothermally synthesized crystals' uniform size and morphology, they are an excellent target for exfoliation into nanosheets. Thus, hydrothermal synthesis provides the first process to control and tune the size and morphology of the $ACuSi_4O_{10}$ series on both the micron and nano scale.

Finally, we developed a method for facilely exfoliating the $ACuSi_4O_{10}$ series into nanosheets. Using hot water and agitation, we were able to exfoliate the $ACuSi_4O_{10}$ series into mono-to-few layers over the course of two weeks. Our resulting nanosheets were freestanding with lateral dimensions ranging from a hundred nanometers up to a few microns. The dimensions of the nanosheets were dependent on the dimensions of the bulk material. One example of this phenomenon was when our hydrothermally synthesized $BaCuSi_4O_{10}$ crystals exfoliated into uniform nanocrystals. We also showed that the exfoliation process could take place at room temperature, although the time scale required was far longer. Additionally, since our $ACuSi_4O_{10}$ nanosheets retained the strong emission in the near-infrared of the bulk material, we were able to solution process the nanosheets into inks for inkjet printing and spray coating. They were also used to form a macroscopic paper. Furthermore, we demonstrated that our nanosheets can be used as biological imaging agent that shows similar luminescence to quantum dots.

The metal copper tetrasilicate series has been many things to many people over the centuries. First it was a source of brilliant blue color for the ancient world. Then a puzzle for 19^{th} century chemists and archaeometrists. Next, geologists discovered that it existed in nature as rare minerals. The strong photoluminescence was an incredibly useful tool for art historians and provided new applications for the series. While through the ages, countless artists and art lovers have found inspiration and delight in its vibrant hues. Now the metal copper tetrasilicate series has firmly established itself in modern nanoscience. Given such a rich and varied history, it would not be surprising if this series holds additional secrets for future researchers to unveil.

References

1. (a) Berke, H., *Angew. Chem. Int. Ed.* **2002,** *41*, 2483-2487; (b) Eastaugh, N. W., V.; Chaplin, T.; Siddall, R., *The Pigment Compendium: A Dictionary of Historical Pigments*. **2005**, Butterworth-Heinemann: Oxford, U.K.; (c) Berke, H., *Chem. Soc. Rev.* **2007,** *36*, 15-30.

2. (a) Pozza, G.; Ajò, D.; Chiari, G.; De Zuane, F.; Favaro, M., *J. Cult. Heri.* **2000,** *1*, 393-398; (b) Verri, G., *Anal. Bioanal. Chem.* **2009,** *394*, 1011-1021.

3. (a) Mirti, P.; Appolonia, L.; Casoli, A.; Ferrari, R. P.; Laurenti, E.; Amisano Canesi, A.; Chiari, G., *Spectrochim. Acta, Part A* **1995,** *51A*, 437-46; (b) Russell, W. J., *P. Roy. Soc. Lond. A. Mat.* **1893,** (XIV), 67-71.

4. (a) Minguzzi, C., *Period. Mineral. Mag.* **1938,** *9*, 333-345; (b) Giester, G.; Rieck, B., *Mineral. Mag.* **1994,** *58*, 663-670; (c) Giester, G.; Rieck, B., *Mineral. Mag.* **1996,** *60*, 795-798.